Effective Strategies to Enhance Electrochemical Performance of Carbon Materials for Non-Aqueous Potassium- and Sodium-Ion Capacitors

TECHNISCHE UNIVERSITÄT
ILMENAU

Dissertation

Zur Erlangung des Doktorgrades

Dr. rer. nat.

Vorgelegt dem Institut für Physik der Fakultät für Mathematik und Naturwissenschaften der Technische Universität Ilmenau

Von

Chenglin Zhang

Ilmenau

1. Gutachter: Prof. Dr. Yong Lei
2. Gutachter: Prof. Dr. Heiko O. Jacobs
3. Gutachter: Prof. Dr. Zhijie Wang

Tag der Einreichung: 19.10.2021

Tag der wissenschaftlichen Aussprache: 24.02.2022

URN: urn:nbn:de:gbv:ilm1-2022000060

DOI: 10.22032/dbt.51557

Abstract

Hybrid ion capacitors have attracted much attention for decades as an emerging class of energy storage system that may bridge the performance of commercial electric double-layer capacitors with high-power output and conventional secondary ion batteries with high-energy output. Recently, potassium- and sodium-ion capacitors have been considered as promising energy storage devices to realize commercial applications owing to the abundant and low-cost sodium and potassium resources. However, there are still three key challenges to promote their development. First, electrode capacity suffers from the complexity of hybrid ion storage. Second, ionic diffusion kinetics suffers from the large radius of Na and K ions. Third, there is a lack of electrolyte research.

In order to tackle these challenges, three novel and effective strategies are developed to optimize three important components of hybrid ion capacitors: cathode, electrolyte, and anode. First, an oxygen-functionalized carbon electrode is fabricated as the high-capacity cathode for potassium-ion capacitors. The rationality of the carbon precursor selection and oxygen functionalization engineering are discussed. Second, a systematic investigation between the electrolytes and dual-ion storage is carried out. This work first reveals that the interaction of the cations and anions plays a key role in the dual-ion storage of the carbon cathode. It further demonstrates that the ether electrolyte outperforms the ester electrolytes in high-rate cation and anion storage. Third, a combination of adsorption mechanism and co-intercalation mechanism is proposed to realize fast sodium-ion storage on the carbon anode. All three works are demonstrated in both half cells and full cells, they achieve improved electrochemical performance in terms of large capacity, long cycle life, and high rate capability. These effective strategies can provide valuable guidance regarding materials synthesis design, electrolyte optimization, and mechanism modification for approaching high-performance hybrid ion capacitors.

Zusammenfassung

Hybrid-Ionen-Kondensatoren werden seit Jahrzehnten als eine aufstrebende Klasse von Energiespeichersystemen betrachtet, die die Leistung kommerzieller elektrischer Doppelschichtkondensatoren mit hoher Leistung und konventioneller Sekundär-Ionen-Batterien mit ausgezeichnet energischem Output überbrücken können. In der letzten Zeit wurden Kalium- und Natrium-Ionen-Kondensatoren aufgrund der Abundanz und der Kosten-Günstigkeit des Kalium- und -Natriumressourcen als aussichtsreiche Energiespeicher für kommerzielle Anwendungen angesehen. Aber drei wesentliche Herausforderungen sollen zuerst diskutiert werden. Die limitierte Elektrodenkapazität aufgrund der Komplexität der hybriden Ionenspeicherung, die Diffusionskinematik der Ionen beschränkt durch den großen Radius der K- und Na-Ionen und die fehlende Elektrolytforschung.

Um die obengenannten Herausforderungen zu bewältigen, werden drei neuartige und effektive Strategien entwickelt, sodass die drei wichtigen Komponenten bzw. die Kathode, der Elektrolyt und die Anode der Hybrid-Ionen-Kondensatoren optimiert werden können. Zuerst wird eine mit dem Sauerstoff funktionalisierter Kohlenstoff-Elektrode als höher Kapazität-Kathode der Kalium-Ionen-Kondensatoren hergestellt. Dabei wird die Rationalität der Auswahl der Kohlenstoff-Precursoren und die Sauerstofffunktionalisierungstechnik diskutiert. Demnächst wird eine systematische Korrelationsuntersuchung zwischen den Elektrolyten und der Dual-Ionenspeicherung der Sauerstoffkatode der Kalium-Ionen Kondensatoren durchgeführt. Die Interaktion zwischen Kationen und Anionen spielt eine wichtige Rolle bei der Dual-Ionen-Speicherung der Kohlenstoff-Kathode. Darüber hinaus wird gezeigt, dass der Ether-Elektrolyt bei der Kationen- und Anionen-Speicherung mit hohen Raten besser als der Ester-Elektrolyt wirkt. Drittens wird eine Kombination aus Adsorptions- und Co-Interkalationsmechanismus als neue Ionenspeicherungsmechanismus vorgeschlagen, um eine effiziente schnelle Na-Ionen-Speicherung auf der Kohlenstoff-Anode der Nalium-Ionen Kondensatoren zu realisieren. Alle drei Arbeiten werden sowohl in Halb- als auch in Vollzellen demonstriert, sodass eine verbesserte elektrochemische Leistung in Bezug auf große Kapazität, lange Lebensdauer und das High-Rate Vermögens erreichen werden kann. Die obengenannten effektiven Strategien haben ausführlich gezeigt, wie die Gestaltung der Materialsynthese, die Optimierung des Elektrolyten und die Modifizierung des Mechanismus für die leistungsstarken Hybrid-Ionen-Kondensatoren sind.

Acknowledgement

Throughout the researching and writing for this dissertation, I have received a great deal of support and assistance. Individuals who aided me in this task need to be singled out for special mention.

First and foremost, I would like to express my sincere gratitude to my supervisor, Prof. Yong Lei. I thank him for providing me with the opportunity to conduct my Ph.D. thesis in his research group. I appreciate all his invaluable and continuous support in formulating the research topics and methodology during my Ph.D. study, his patience, motivation, and thoughtfulness. His expertise helped me in all the time of research and writing of this thesis. The insightful feedback pushed me to sharpen my thinking and brought my work to a higher level. Moreover, he encouraged me to be an independent thinker and instructor, and he also encouraged me into other academic activities including teaching activities and conference management. I'm really grateful for the enjoyable and valuable experiences and memories that we shared in the past four years.

My sincere thanks also go to Dr. Yang Xu, who provided me with a lot of training on professional skills in related research fields. I am grateful to him for enlightening me at the first glance of research. Dr. Huaping Zhao who makes me convenient to get access to research facilities also has my sincere gratitude. His contribution to the daily procurement and management of the laboratory ensured that my experiment can be carried out smoothly and effectively. Without their precious support, it would not be possible to conduct the research in this dissertation.

I thank my fellow labmates. The stimulating discussion with Dr. Yuhan Wu always helps me a lot. Dr. Rui Xu, Dr. Long Liu, Mo Sha, Shouzhi Wang, Chengzhan Yan, Pankaj-Chandan Solanki, Dr. Huanming Zhang, Yulian Dong, Jiajia Qiu, your kind suggestions and helps supported me facing the challenges and difficulties of my research. I will always remember the happiness that we were working together and all the fun we have had in the last four years.

Additional thanks must be extended to the foundation of my financial support, China Scholarship Council, which sponsored all my university and living expenses during the last four years.

Last but not the least, I would like to thank my family and friends for supporting me spiritually throughout writing this thesis and my life in general.

Table of Contents

List of Figures and Tables

List of Abbreviations

AC	Activated carbon
APS	Ammonium persulfate
CV	Cyclic voltammetry
CNT	Carbon nanotubes
CE	Coulombic efficiency
CTAB	Ammonium persulfate
CMC	Carboxymethyl cellulose
DEC	Diethyl carbonate
DME	Dimethyl ether
DEGDEM	Diethylene glycol dimethyl ether
ESSs	Energy storage systems
ECs	Electrochemical capacitors
EDLCs	Electrochemical double-layers capacitors
EIS	Electrochemical impedance spectroscopy
EC	Ethylene carbonate
FEC	Fluoroethylene carbonate
FTIR	Fourier transform infrared spectroscopy
GITT	Galvanostatic intermittent titration
GO	Graphite oxide
HC	Hard carbon
HRTEM	High-resolution transmission electron microscopy
LTO	Lithium titanate
LIBs	Lithium-ion batteries
LICs	Lithium-ion capacitors
MOF	Metal organic framework
NC	Nitrogen-doped carbon
NMR	Nuclear Magnetic Resonance
NMP	N-methyl-2-pyrrolidone

ONC	Oxygen-functionalized carbon
OCNT	Oxygen-functionalized carbon nanotubes
OAC	Oxygen-functionalized activated carbon
PIBs	Potassium-ion batteries
PICs	Potassium-ion capacitors
PC	Propylene carbonate
PPy	Polypyrrole
PVdF	Polyvinylidene fluoride
PG	Pristine graphite
PAS	Polyacenic semiconductive
RGO	Reduced Graphite oxide
SIBs	Sodium-ion batteries
SICs	Sodium-ion capacitors
SC	Soft carbon
SEM	Scanning electron microscopy
SEI	Solid electrolyte interphase
TEM	Transmission electron microscopy
TEGDEM	Tetraethylene glycol dimethyl ether
2D	Two-dimensional
3D	Three-dimensional
XRD	X-ray diffraction
XPS	X-ray photoelectron spectroscopy

1 Introduction

Nowadays, we humans face a critical challenge, the contradiction between global warming and energy production. With ever-growing global populations, the energy supply is becoming increasingly severe. We must double the energy production from the present rate of 14 TW to 28 TW by 2050 (Figure 1-1a). However, in response to the climate change crisis, this increase must be achieved without increasing CO_2 emissions.[1-3] The energy demand and fossil-fuel resources reduction require the update of sustainable energy alternatives, including both renewable energy sources and sustainable storage technologies. Wind, solar, geothermal, and tide energies are considered as eco-friendly energy sources. However, the intermittent feature of these energy sources makes them need large-grid energy storage systems (ESSs) to store and deliver them sustainably and efficiently (Figure 1-1b).[4, 5] Furthermore, it is crucial to incorporate raw material abundance, eco-efficient synthetic processes, and long cycle life into the design of new electrochemical storage systems.

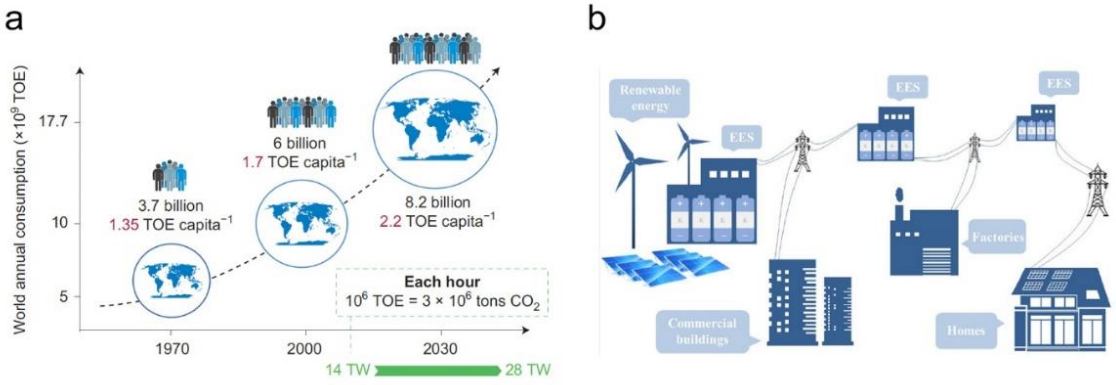

Figure 1-1 (a) Past, present and forecast of the world's energy needs up to 2050.[1] (b) Schematic illustration of the smart gird in which large-scale energy storage systems integrate renewable energy into the grid.[4]

Due to the abundant resources, low cost, and well-distributed reserves of sodium and potassium, sodium- and potassium-ion-based energy storage devices are promising technologies for constructing the large-grid ESSs.[6-8] Currently, sodium- and potassium-ion batteries (SIBs and PIBs) have been widely studied and achieved great progress.[4, 9-18] However, other sodium- and potassium-ion-based energy storage devices, sodium-ion capacitors (SICs) and potassium-ion capacitors (PICs) that can offer both high energy and high

power have not advanced to the same extent.[19] It is therefore essential to develop these two new types of ion-storage technologies. In order to further promote the commercialization of SICs and PICs, it is not enough to reduce the cost just by replacing lithium with sodium and potassium, we must innovate in some low-cost materials. Among all the anode and cathode materials of the hybrid ion capacitors (HICs), the carbon material is a quite unique electrode for the SICs and PICs. It is because on the one hand it can serve as both anode and cathode through storing cations, anions, or dual ions, on the other hand it is cost-effective, easily processed, and renewable.[20, 21] In this dissertation, I mainly focus on the optimization of carbon cathodes and anodes for high-performance SICs and PICs. This research completely complies with the critical requirements on the development of new energy storage technologies.

This dissertation is divided into two major parts. The first part mainly reviews the literature that is related to the background of my research topic. The second part mainly presents the results and discussions of my research. The majority of novel research in this dissertation is summarized into three parts. To be specific, in chapter 2, there will be a comprehensive introduction including the motivation of developing HICs, the history and progress of electrode materials exploration. In chapter 3, the origin and concept of my research will be introduced. The issues presented in this section will be addressed accordantly by carrying out three new strategies. In chapter 4, I propose an oxygen functionalization engineering towards well-exploiting carbon nanomaterial as a cathode to achieve enhanced potassium-ion storage performance. Selecting a precursor with abundant graphene edges for oxygen functionalization engineering is discussed and suggested. In chapter 5, I systematically investigate the relationship between the dual-ion storage and electrolytes in graphite oxide cathodes of PICs. It is verified that the ether electrolyte can isolate the cations and anions more efficiently, which gives more freedom of the ion diffusion at or near the electrode interface thus ensuring fast K-ion storage. In chapter 6, I propose a combination of adsorption mechanism and co-intercalation mechanism instead of a conventional combination of adsorption mechanism and single-ion intercalation mechanism towards ultrafast sodium-ion storage on the anode of SICs. Benefiting from an introduction of co-intercalation, the highly graphitic carbon layers can efficiently store sodium ions during high-rate charge and discharge processes. In chapter 7, there will be a conclusion regarding the issues that I have addressed in this dissertation. In addition, an exciting perspective will be conceived.

2 Background: hybrid ion capacitors for energy storage

2.1 Motivation for hybrid ion capacitors

The ubiquity of portable electronics including mobile phones, laptops, electric vehicles would not be possible without ESSs. There are primarily two power sources for the reversible electrochemical energy supply: secondary-ion batteries and electrochemical capacitors (ECs). The electrochemical capacitors include electronic double-layer capacitors (EDLCs) and supercapacitors. Generally, secondary-ion batteries output high energy density, while the electrochemical capacitors possess the characteristic of high-power density output and long cycle life.[22-26] In rechargeable batteries, the chemical energy of the active mass reversibly converts into electrical energy by reversible redox reactions in the bulk phase of cathode and anode. During discharge, the electrolyte transports the ionic component from the anode to the cathode and forces the electron to traverse an external circuit, then back again when it charges (Figure 2-1a).[27, 28] A change in the valence of all active materials produces a large amount of electron transfer, which is the reason for the capability of the large energy density of the battery technology. As we know, the dominant energy storage technology is lithium-ion batteries (LIBs). We even can't imagine what the modern world would be if LIBs were not be founded and developed. The first commercial LIB based on $LiCoO_2$ cathode//graphite anode was introduced in 1991 by Sony Corporation.[29] After the development for three decades, the state of art LIBs is reaching an energy density of 200 Wh kg^{-1}, while the power density is still limited. For instance, commercial Panasonic LIBs exhibit an energy density of 200 Wh kg^{-1} but a power density of only 350 W kg^{-1} (Figure 2-1b).[26, 30, 31] In rechargeable ECs, there are two forms of energy storage (Figure 2-1a). One is the regular adsorbing electrolyte ions onto the surface of anode and cathode, which creates double-layer capacitance driven by the potential dependence of electrostatic adherence. Another is adsorbing the diffusion ions generated from the reversible redox reaction at the interface of the anode and cathode. The most notable feature of these charge-storage behaviors is that they both take place on the surface or interface of the electrode, which is the reason for the capability of the high power density of the ECs technology. The commercial ECs were first produced as memory backup power sources of commercial computers in 1978 by NEC (Japan) under the energy company SOHIO's license. Until now, most commercial ECs possess a great power density as high as 10 kW kg^{-1} but a limited energy density of 5 Wh kg^{-1} (Figure 2-1b).[32, 33]

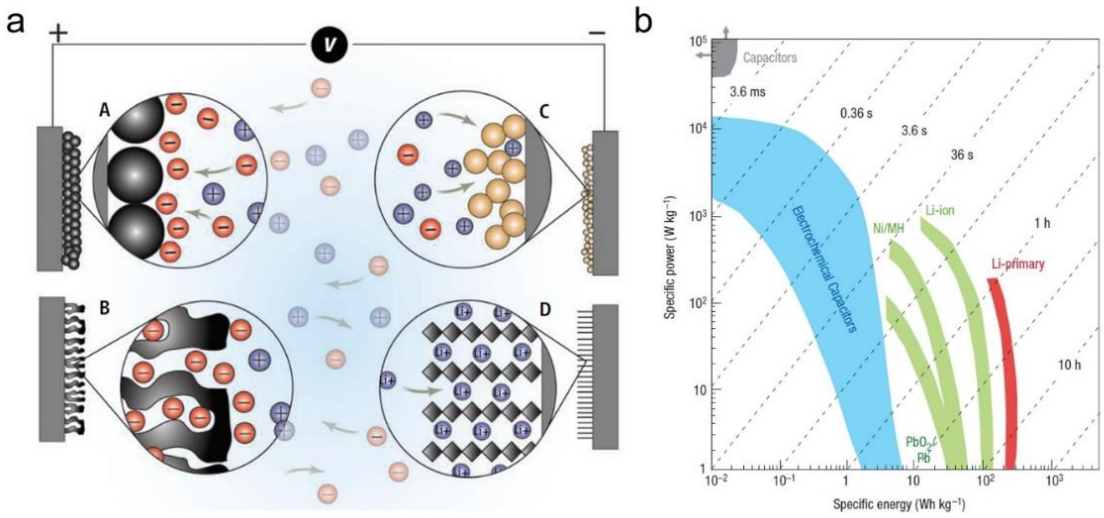

Figure 2-1 (a) Comparison of electrochemical energy storage mechanisms between batteries and electrochemical capacitors, upper: electrochemical capacitors, bottom: batteries.[27] (b) Specific power against specific energy for various electrical energy storage devices.[26]

Despite their different electrochemical behaviors and characteristics, secondary-ion batteries and ECs are constructed from similar components, both are configurated by cathode, anode, electrolyte, separator, and current collector. As far as we are concerned, the ultimate target of the development of new energy storage technologies for EESs is to approach both high energy density and high power density within long cycle life in a single device, the hybridization of secondary-ion batteries and electrochemical capacitors is one of the best choices. A new energy storage technology, HICs are proposed, which consists of a capacitor-type electrode and a battery-type electrode.[31, 33-35] Figure 2-2a shows that HICs exhibit comparable energy density to the secondary-ion batteries (up to 100 Wh kg^{-1}), while in principle delivering capacitor-like power density (up to 10 kW kg^{-1}).[36-38] In the case of HICs, during discharging or charging, the bulk redox reactions occur at battery-type electrodes, delivering cations. In the meantime, the surface EDLC-type or pseudocapacitive redox reactions occur at capacitor-type electrodes, storing anions or cations (Figure 2-2b).[39] Moreover, the capacitor-type electrodes can either be EDLC-type or supercapacitor-type electrodes, and either be cathodes or anodes.

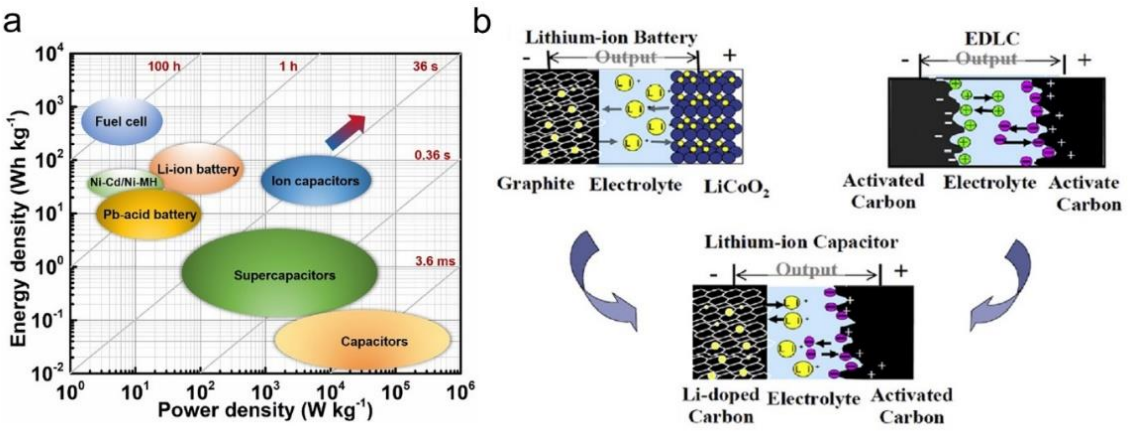

Figure 2-2 (a) Ragone plots of various energy storage systems, Li-ion capacitors belong to the class of HICs.[36] (b) Update of the chemical reaction in case of three different types of energy storage.[39]

Since HICs were proposed as promising devices to bridge the performance of commercial ECs and metal-ion batteries, they have been evaluated in many industrial applications in the literature, including renewable energy storage systems, power electronics, flywheels, braking systems of different transportations, pulsed power, hybrid electric vehicles, spacecraft, and satellites.[40, 41] For instance, Nakayama et al. proposed a high-efficient converter system by using temporary storage of LICs under low solar irradiance. The updated power conditioning units achieve an increase of 12% of the annual gross power generation.[42] Additionally, the application of LICs in photovoltaic generation and wind power mitigation connected to the grid was also studied.[43] For the power electronics, Lambert et al. demonstrated that LICs are more suitable due to the better toleration at high frequency as compared with supercapacitors.[44] LICs were also identified as a replacement for some energy-storage media utilizing flywheel technology.[45] There is also a huge potential market that applies HICs to braking systems of transportations, including railways, elevators, vehicles. Interesting research by Ciccarelli et al. suggested an energy management control system based on LICs.[46] The proposed strategy is capable of promoting remarkable energy saving (up to 30%). Moreover, Uno et al. applied LICs to the spacecraft and Soltani et al. studied the application of LICs in a pure electrical bus.[47-49] The wide range of applications of HICs further tells its necessity to develop.

2.2 Evolution of hybrid ion capacitors: from lithium to sodium and potassium

The development of hybrid ion capacitors started from the LICs. The initial study dates back to 1981 when an amorphous carbonaceous material, known as PAS (polyacenic semiconductive) was invented. PAS was demonstrated as an electrode in rechargeable devices, which exhibited high specific energy, and later was commercialized as the PAS capacitors. PAS capacitors began to be used in 1986, and later a LIC was invented by using a similar material in 1991.[50] Another impressive early research on LICs was reported by Amatucci et al (Figure 2-3).[51] They first constructed a hybrid LIC using nanostructured insertion-type $Li_4Ti_5O_{12}$ as the anode and activated carbon (AC) as the cathode. The energy density was promoted to 20 Wh kg^{-1} for the first time, which is about three times higher than conventional capacitors. This work encouraged many researchers to develop new types of electrode materials for LICs. Since then, a series of LICs based on lithium titanate (LTO), graphite, V_2O_5, MnO, Fe_2O_3, Nb_2O_5, etc. are discovered. So far, lots of combinations of electrode materials for LICs have been practical.[39, 52-54] LICs are configurated by a capacitor-type electrode against a lithium-ion-battery-type electrode in lithium-ion based electrolyte. These two types of electrodes reversibly store cations and anions in low and high potential ranges, respectively, providing a high open voltage window and achieving high energy density. From the configuration of LICs, lithium-ion-based electrolytes and the electrodes of lithium-ion batteries are important components. Therefore, it is unsurprising that the earliest hybridization devices of ECs and batteries are LICs in consideration of widely commercial LIBs applications. It is well known that LICs and LIBs are mature energy storage technology and have currently dominated the market for portable energy storage devices. Many modern devices including mobile phones, laptops, cameras, and electric vehicles are mainly powered by LIBs and LICs. Especially for electric vehicles, many countries have announced their policies about the replacement of petrol energy vehicles with electric vehicles in the next decade. Unfortunately, it reminds a debate about whether the lithium resource can be enough to meet such a booming demand. As known, lithium reserve is only about 0.0017% so far and has limited geographical distribution (Table 2-1).[5, 11, 12] Moreover, it has been predicted that the recyclization of lithium reserves may not be overcome in the next decade.[55] Therefore, it is urgent to develop other new battery technologies as a supplement to lithium-based energy storage technology.

Table 2-1 Physical and economic characteristics of lithium, sodium, and potassium.[5]

Alkalis	**Lithium**	**Sodium**	**Potassium**
Atomic Number	3	11	19
Atomic Weight	6.941	22.989	39.0983
Density (g/cm^3)	0.535	0.968	0.856
Melting Point (°C)	180.54	97.72	63.38
Atomic Radius (pm)	167	190	243
Ionic Radius (pm)	76	102	138
Voltage vs. SHE (V)	-3.04	-2.71	-2.93
Abundance in Earth's Crust (%)	0.0017	2.3	1.5
Distribution	70% in South America	Everywhere	Everywhere
Cost of industrial grade metal (US $/ton)	~100000	~3000	~13000

In the last decade, sodium- and potassium-ion-based energy storage technologies have been identified as potential candidates for next-generation storage devices. Naturally, SICs and PICs are considered as promising alternatives to LICs.[56-58] As lithium's counterparts, they have many fundamental differences and similarities between each other. As shown in Table 2-1, they both are alkali metals and belongs to the same group in the periodic table, and the standard potentials of Na/Na^+ (-2.71 V *vs.* standard hydrogen electrode) and K/K^+ (-2.93 V *vs.* standard hydrogen electrode) are very close to that of Li/Li^+ (-3.14 V vs. standard hydrogen electrode), suggesting that sodium and potassium have similar electrochemical properties to lithium. In particular, the abundance of sodium and potassium reserves in the earth are respectively 2.3 % and 1.542%, nearly 1000 times higher than that of lithium. The cost of industrial-grade sodium (~3000 US $/ton) and potassium metal (~13,000 US $/ton) are also much lower than that of lithium metal (~130000 US $/ton), which suggests that SICs and PICs will be more cost-

effective and essential for large-scale applications. Additionally, the melting points of sodium (97.72 ℃) and potassium metal (63.38 ℃) are much lower than that of lithium metal (180.54 ℃). In this case, the dendrite leads to an internal short circuit during overcharging, dendritic sodium and potassium will melt readily at a safe temperature, which means that the safety issue of SICs and PICs would be less remarkable than that of LICs. Nevertheless, the atomic weight and density of sodium and potassium are higher than those of lithium, thus the gravimetric and volumetric energy densities of SICs and PICs are inevitably lower than those of LICs. Furthermore, the larger Na-ion and K-ion radiuses make them difficult for the diffusion in the bulk of electrode. As compared with Li-ion storage, sodium- and potassium-ion storage will lead to a much larger expansion of the host materials. Therefore, the optimization of SIC and PIC electrodes is required to be more rigorous to allow effective and rapid reversible ionic insertion and extraction. However, given by the weaker Lewis acidity of Na-ions and K-ions versus Li-ions, Na ions and K ions may possess an advantage of fast ionic transportation in electrolytes, which is very critical for fast rate devices of SICs and PICs.

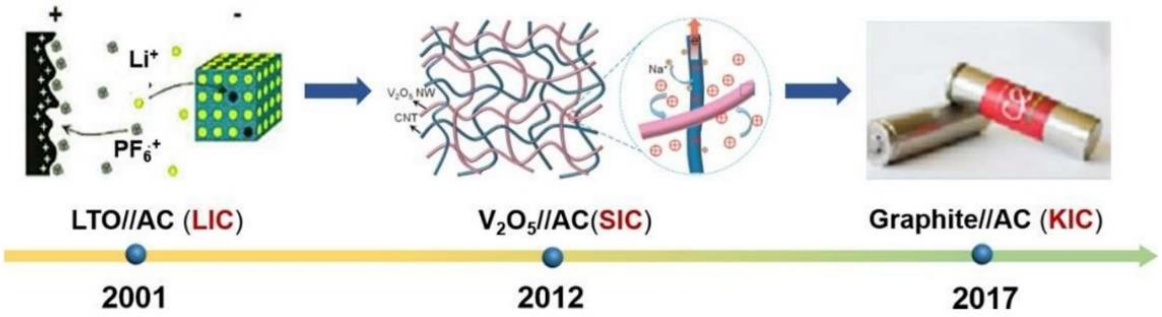

Figure 2-3 The development process of hybrid ion capacitors (LICs, SICs, and PICs).[59]

As same as LICs' history, the history process of SICs and PICs began after the research boost of SIBs and PIBs (Figure 2-3). Since 2010, many publications were reported in relation to the electrode materials for the Na-ion host.[57, 59-62] Thereafter, in 2012, Chen et al. demonstrated a nonaqueous SIC by firstly utilizing $NaCl_4$ in propylene carbonate (PC) electrolyte.[63] The capacitor device was configurated with a composite of layers V_2O_5 nanowires and carbon nanotubes (CNTs) as the anode and AC as the cathode. It delivered a maximum energy density of ~40 Wh kg^{-1} and ~80% of the initial capacity over 900 cycles at a power density of ~1700 W kg^{-1}. Since then, a certain amount of research has been done on SICs. Subsequent research into PICs began in 2017, which follows the rapid development of PIBs after 2015.[64-67] Le Comte et al. introduced the pioneering work of PICs.[68] The capacitor device was configurated

by utilizing graphite as anode and AC as cathode with 0.8 M KPF_6 in acetonitrile electrolyte. An energy density of 12 Wh kg^{-1} was achieved. The cycling stability is outstanding, which can run up to 55000 cycles at a high current density of 100C. So far, PICs have been rarely reported. Overall, the studies of SICs and PICs are very attractive and still at their infancy stage.

2.3 Fundamentals of SICs and PICs

2.3.1 Working principles

According to the ion storage mechanism, SICs or PICs can be classified into three types (Figure 2-4):[59]

a) Electrolyte consuming mechanism: this type of capacitor commonly consists of a battery-type anode electrode (Titanium compounds or metal oxide/sulfides) and a capacitor-type cathode electrode (it is usually AC). During the charging process, the anions and cations are separated from the electrolyte and move to the cathode and anode, respectively. Under a certain voltage, the cathode undergoes an anion adsorption process and the anode undergoes a cation intercalation process. During discharging process, the anions and cations reversibly go back to the electrolyte.

b) Ionic exchange mechanism: this type of capacitor commonly consists of a battery-type cathode, which provides cations (ceramic materials), and a capacitor-type anode electrode (porous carbon materials, MXene). The electrolyte only acts as a transportation medium of cations. During charging and discharging processes, the reversible ion-storage process is analogous to “Rocking-Chair” SIBs or PIBs.

c) Hybrid mechanism: the feature of this type of capacitors is that the anode and the cathode, one or both are composed of battery-type and capacitor-type electrode materials (graphite oxide as, carbon-based composites). During the charging process, the cathode absorbs free anions from the electrolyte and extracts cations into the electrolyte in the meantime. The anode reversible store cations, which are provided from the electrolyte or additionally from the cathode. During discharging process, the pathways are reversed.

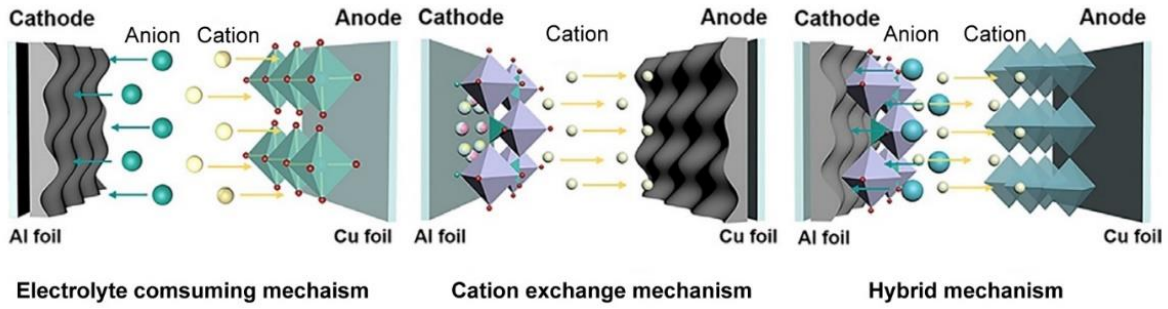

Figure 2-4 Configurations of three types of SICs.[59]

2.3.2 Calculation

The energy density (Wh kg^{-1}) of HICs is normally estimated by directly integrating the area below the profiles of operation voltage-capacity (Figure 2-5).

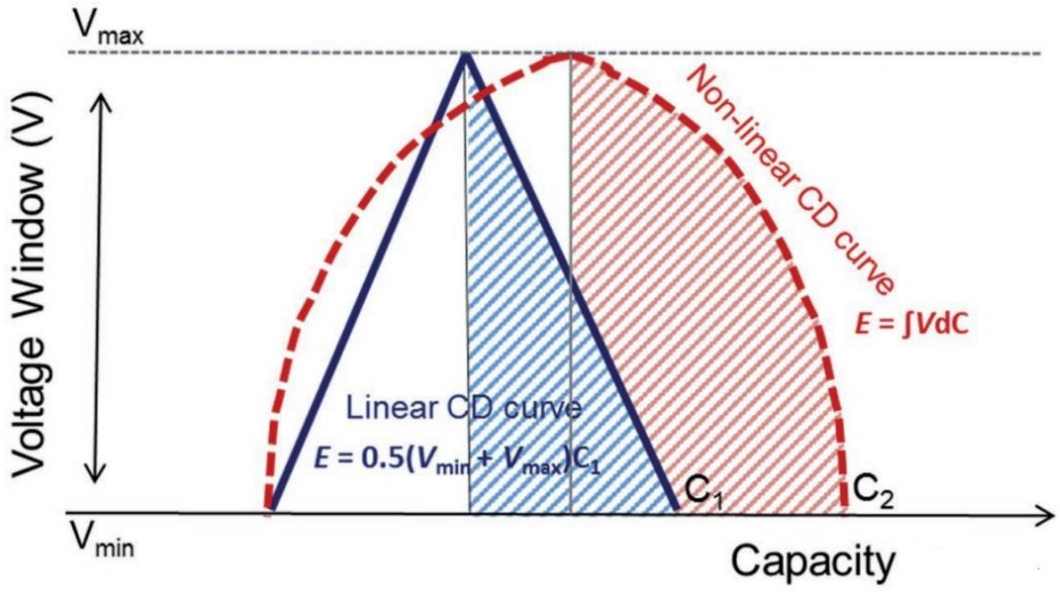

Figure 2-5 Schematic of electrochemical profiles of the typical HICs with linear and non-linear relationships between operation voltage and capacity.[57]

For the linear relationship:

$$E = \frac{1}{2}(V_{min} + V_{max}) \times C_1 \qquad Eq.1$$

for the non-linear relationship:

$$E = \int_{V_{min}}^{V_{max}} C_2 \, dV \qquad Eq.2$$

and the power density (W kg^{-1}) is estimated by the equation:

$$P = \frac{E}{t} \qquad Eq.3$$

where V_{max} and V_{min} are the upper and lower limits of the voltage window at different current densities, respectively. C_1 and C_2 are the discharge capacity. t is the discharge time.[57, 59, 69] Furthermore, the charge balance between cathode and anode is necessary for a HIC configuration:

$$Q_{cathode} = Q_{anode} \qquad Eq.4$$

$Q_{cathode}$ and Q_{anode} are determined by the specific capacity ($C_{electrode}$), the active mass of the electrode (m), and the working voltage window (ΔV) according to the equation:[70]

$$Q_{electrode} = C_{electrode} \times m \times \Delta V \qquad Eq.5$$

2.4 Anode materials

Since the exploration of SICs and PICs emerged in the last decade, many anode materials have been developed. They are classified into carbonaceous materials, titanium-based materials, metal chalcogenides, niobium-based and vanadium-based pentoxides, and other types of materials. They are typical battery-type anode materials.[71]

2.4.1 Carbonaceous materials

Owing to the advantages of low cost, good chemical stability, and renewable resources, carbonaceous materials have been extensively utilized as the anodes of HICs. In fact, the carbonaceous anode of HICs and the carbonaceous of batteries store ions in the same principle. As shown in Figure 2-6, there are two types of carbonaceous materials for electrochemical ion storage. One is the graphitic carbons with ordered layer structures, and another is the amorphous carbons with ordered and disordered layer structures. The graphitic carbons store ions by intercalation mechanism, and the amorphous carbons store ions by both intercalations between the ordered carbon layers and adsorption mechanisms at the electrode interface (including filling and pseudocapacitance or redox capacitance).[72] Various carbonaceous

materials have been demonstrated for SICs and PICs, including graphite, soft carbon, hard carbon, heteroatom-doped carbon, and biomass-derived porous carbon.[73-75]

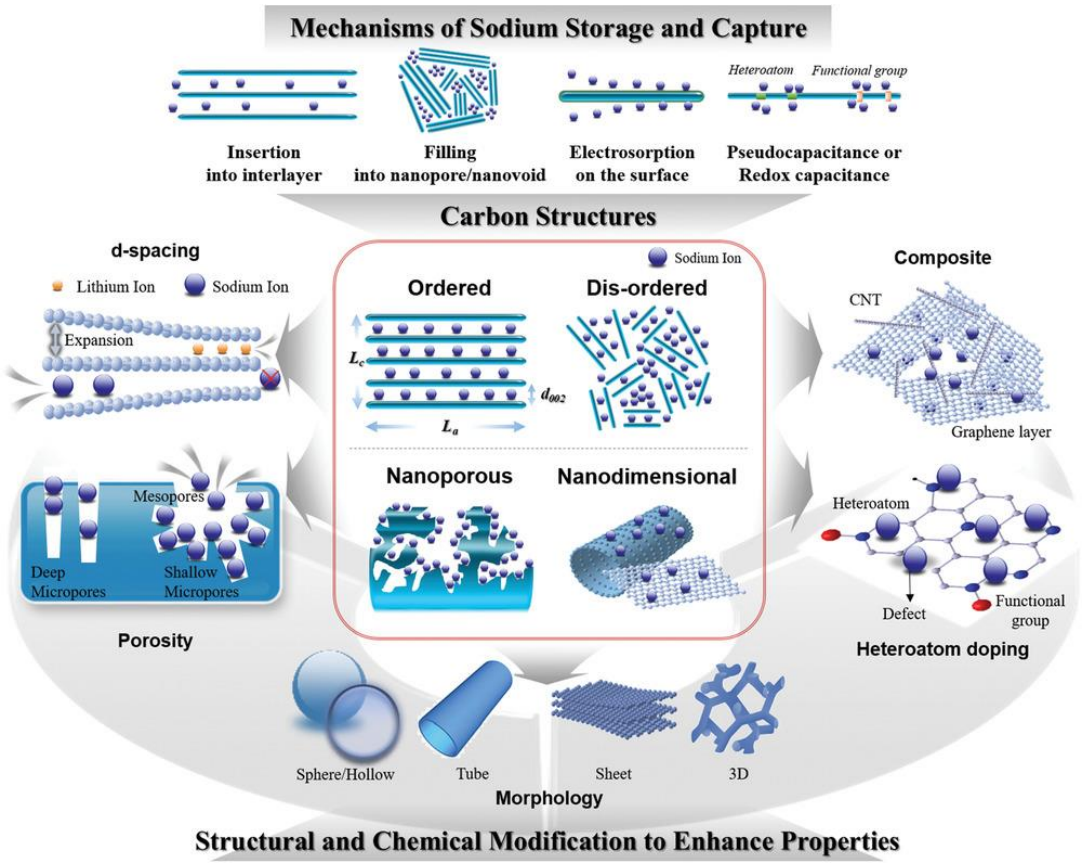

Figure 2-6 Schematic illustration about the mechanisms of sodium-ion storage and capture in carbon materials, and their structural and chemical modifications to improve the electrochemical performance.[72]

Graphite stores potassium ions through single intercalation or co-intercalation mechanism while it stores sodium ions only through co-intercalation.[64-66, 76-85] Soft carbon, hard carbon, and biomass-derived porous carbon with many defects and porous structures can store potassium ions or sodium ions through the adsorption at carbon defects and intercalation in expanded carbon layers.[86-98] Heteroatom-doped carbon with many heteroatom-containing functional groups, carbon defects store potassium ions or sodium ions through the ion adsorption or reaction related to functional groups, intercalation in expanded carbon layers.[99-108]

Owing to the large radius of Na^+ and K^+, the diffusion rate of sodium ions or potassium ions in the bulk of an electrode is sluggish, leading to a severe polarization effect, poor rate

capability, and poor cyclability. To break through this limitation, many rational designs have been demonstrated to promote the ion storage kinetics, which can be refined as following three major parts (Figure 2-6):

a) Expending interlayer spacing between the order carbon layers to allow the insertion of large sodium-ion or potassium-ion insertion. For instance, a 3D framework carbon with large graphitic interlayer spacing was synthesized as the anode for SICs, the full SICs exhibits a high energy density of 67 Wh kg^{-1} at a power 20000 W kg^{-1}, and ultra-long cycling stability (80% capacity retention after 10000 cycles at 2.0 A g^{-1}).[109]

b) Optimizing porous structures to facilitate sodium-ion or potassium ion transportation and expose more active sites. For instance, a 3D architecture graphdiyne nanosheets with interconnective porous structure was investigated as a high-performance anode for SICs. It delivers a specific energy density of 166 Wh kg^{-1} at a power density of 15000 W kg^{-1}.[110]

c) Introducing heteroatoms into carbon lattice structures for increasing capacitive adsorption or reaction active sites (e.g. S, P, N, F-doped, or dual-doped carbons). For instance, a 3D nitrogen-doped framework carbon was demonstrated as anode for high-performance PICs, which delivers a high energy density of 163.5 Wh kg^{-1} at a power density of 210 W kg^{-1}.[111]

d) Constructing different morphologies to facilitate ion transportation and electron transfer, including nanosphere/hollow spheres,[112, 113] nanotubes,[114] nanowires,[115] nanosheets,[116] nanobelts,[117] 3D framework.[118] For instance, Wen and co-workers demonstrated phosphorous and nitrogen co-doped hierarchical porous carbon nanofibers, which integrates the advantages of interlayer spacing expansion, electron conductivity enhancement, and active site increase, exhibiting high energy, power density, and long cycle life.[119]

These methods are usually conducted synergistically. Besides, many researchers realize these methods through directly annealing biomass. Generally, biomass-derived carbons are heteroatom-doped disordered carbon because the precursors are mainly composed of elemental C, H, O, and some other light heteroatom. They utilize proper biomass precursors to design the carbon materials with scheduled structure and composition for high-performance sodium- or potassium-ion storage.

2.4.2 Titanium-based compounds

Titanium-based compounds are popular battery-type anode materials for SICs and PICs due to their opened lattice structure which provides fast ion diffusion channels. Besides, the merits

including their low intercalation potential (~0.3 *vs.* Na/Na^+), low cost, and low toxicity further attract researchers' attention. There are many different titanium-based compounds for sodium- and potassium-ion storage, the most common form is titanium dioxide, TiO_2 (Figure 2-7a).[120-128] TiO_2 has seven different crystalline phases, such as anatase, rutile, brookite, and TiO_2(B) In all these polymorphs, the tetravalent titanium cations are sixfold coordinated to divalent oxygen anions to form distorted TiO_6 octahedra.[9] The opening framework structure endows TiO_2 with fast ion diffusion kinetics for sodium-ion and potassium-ion storage. Another common form is sodium/potassium titanates, $K_xTi_yO_z$. As shown in Figure 2-7b–e, this type of titanates also possesses open structural frameworks for fast ion diffusion. So far, various titanates were identified as anodes for SICs and PICs, including $Na_2Ti_3O_7$,[129] $Na_2Ti_9O_{19}$,[130] $Na_2Ti_2O_4(OH)_2$,[131] $K_2Ti_2O_5$,[132] and $K_2Ti_6O_{13}$.[133] Moreover, the NASICON-type titanium-based materials possess interstitials and ionic conduction channels along the c-axis via oxygen atoms sharing of TiO_6 and PO_4 tetrahedra, providing sodium or potassium-ion host (Figure 2-7f).[134-137] However, Ti-based compounds are still hindered by low storage capacity and sluggish reaction kinetics resulting from the poor electronic conductivity.

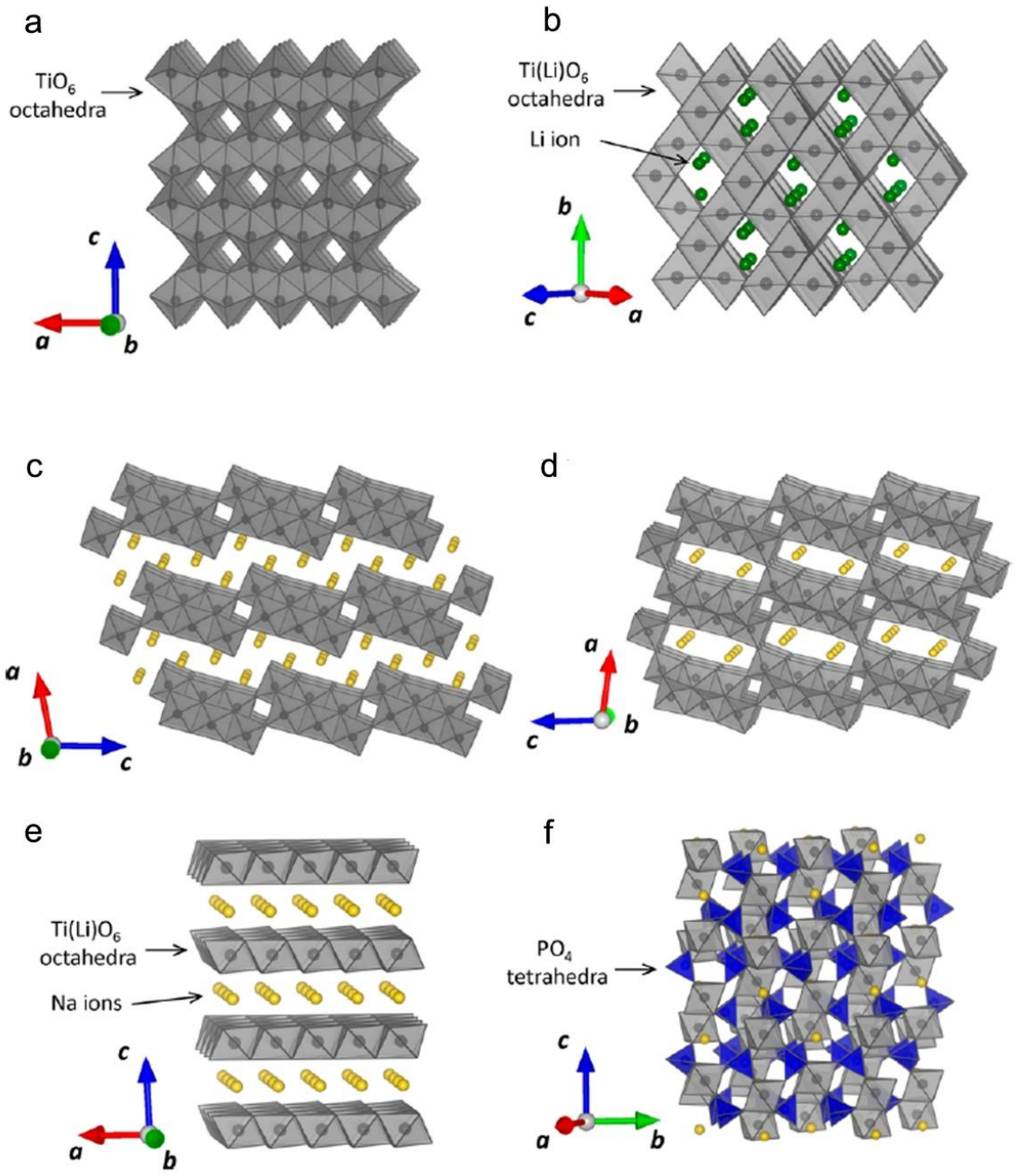

Figure 2-7 Schematic illustrations of (a) anatase-type TiO2, (b) $Li[Li_{1/3}Ti_{5/3}]O_4$, (c) $Na_2Ti_3O_7$, (d) $Na_2Ti_6O_{13}$, (e) P2-$Na_{0.66}[Li_{0.22}Ti_{0.78}]O_2$, and (f) $NaTi_2(PO_4)_3$.[9]

2.4.3 Niobium pentoxide and vanadium pentoxide

Niobium pentoxide (Nb_2O_5) and Vanadium pentoxide (V_2O_5), due to their intrinsic pseudocapacitive behaviors and large interlayer spacings, have been reported for fast ion diffusion and storage in SICs and PICs. However, the metal oxides intrinsically possess poor

electronic conductivity and sluggish reaction kinetics, which seriously restrict their development. Generally, they are synthesized by coupling with carbon materials.[138-143] Wang et al. reported an in-situ encapsulation strategy to grow ultrathin graphene shells over T-Nb_2O_5 nanowires.[141] By configuring the synthesized Gr-Nb_2O_5 with an active carbon cathode, the full SICs deliver a high energy density of 62.2 Wh kg^{-1} with long cyclability. Kiruthiga and coworkers demonstrated V_2O_5 nanorods anchored on reduced graphene as anode for SICs, it outputs a high energy density of 65 Wh kg^{-1}.[144]

2.4.4 Metal chalcogenides

Unlike metal oxides, metal chalcogenides possess better electronic conductivity, mechanical property, and high theoretical capacity, which have been considered as promising anode materials for sodium-ion and potassium-ion storage.[145-152] In principle, this large family of materials commonly store ions by three types of mechanisms: intercalation, conversion reaction, alloying reaction (only for alloying metal-based chalcogenides, such as Bi_2S_3, Sb_2S_3, SnS_2, et. al.).[14, 153-155] These mechanisms usually work in combination. However, the conversion reactions or alloying reactions generally cause large volume variation of the electrode, which leads to poor cycling stability. This issue hinders the development of metal chalcogenides for SICs and PICs.[58] At present, they are just demonstrated and studied in the laboratory and uncommercialized. Designing nanostructured materials and coupling with carbon materials are the major strategies for enhancing the electrochemical performance of this class of materials. For instance, Yi and co-workers synthesized a nitrogen-doped $MoSe_2$/graphene composite using diatomite as the template. The anode exhibits a favorable pseudocapacitive potassium-ion storage. It works as the anode of PICs, delivering a high energy density of 119 Wh kg^{-1} and a high power density of 7212 W kg^{-1}.[152]

2.5 Cathode materials

Most cathode materials in SICs and PICs possess capacitive electrochemical behaviors, which store energy through the adsorption and desorption of anions or cations. They mainly are carbon materials. In addition, those which can store cations with high-rate capability are also used as the cathodes for SICs and PICs, including MXenes, ceramic intercalation materials.

2.5.1 Carbon materials

The carbon materials can be utilized not only as anodes in HICs but also as cathodes. The carbon cathodes possess the same merits as the anodes, including abundant sources, low cost, nontoxic nature, high chemical/thermal stability. Besides, the carbon materials can store anions in high voltage windows, which provide high open voltage in full cells, thus enabling high energy density.[156, 157] Inspired by these advantages, carbon materials show the most promising commercial applications for SICs and PICs.

Activated carbon materials have been commercialized as the cathodes of LICs for years. They are often obtained from various precursors, including biomass,[158, 159] metal-organic frameworks,[160] and polymers.[161, 162] In consideration of easy synthesis, the activated carbons generally are employed as the standard cathode to assembly full cells in the research works of anode materials.[58, 163] However, the low ion storage capacity of activated carbons leads to the low energy density of the full cells. Therefore, researchers currently are developing various other carbon materials with large surface areas, nanostructures, abundant defects, and dopants. Enlarging the surface area and nanostructuring electrode endow more active sites exposures and fast reaction kinetics. The defects and dopants provide additional active sites, further improving the specific capacity.

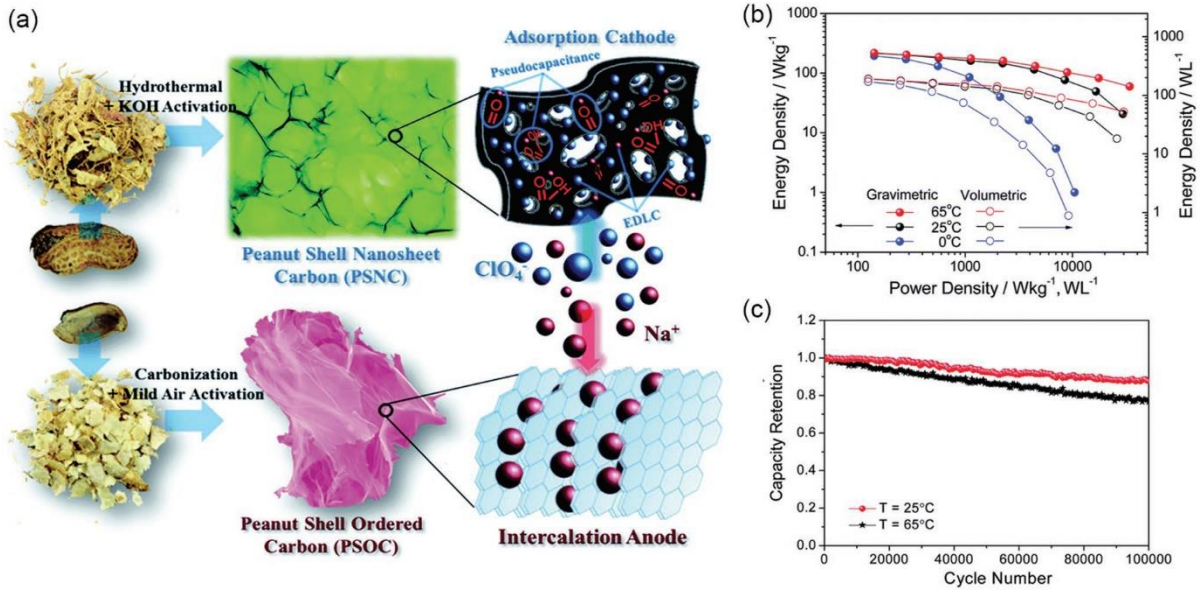

Figure 2-8 (a) Schematic illustration of the synthesis process for peanut shell as cathode (PSNC) and anode (PSOC), and the relevant charge storage mechanisms in SIC. (b) Ragone plots (c) cycling stability of PSOC//PSNC at the different temperatures.[163]

Oxygen-functionalized carbon materials are one of the most promising candidates for the cathodes of SICs and PICs. This type of carbon material possesses the capability of storing both anions and cations within a high voltage window. As shown in Figure 2-8, the oxygen-containing functional groups, *e.g.*, carbonyl, can reversibly react with cations, which is inspired by the studies of organic cathodes in batteries. The reduction reaction occurs that accompanies the cation storage and anion release during the discharging process. During the charging process, the oxidation reaction occurs that accompanies the cations release and anions storage.[163] The energy density and power density can respectively reach 100 Wh kg^{-1} and 10000 W kg^{-1} over 10000 cycles. Graphite oxides and oxygen functionalized multiple-wall carbon nanotubes (MCNTs) are typical representatives. Through the process with the strong oxidants and acids, they possess abundant carbon defects and oxygen-containing functional groups, which are the essential active sites for the storage of anions and cations.[164] Moreover, As compared with the activated carbons, the graphene and CNTs possess higher crystallinity with more sp^2 carbon bonds, which endows them with higher electronic conductivity.[165] Currently, they are wildly utilized in different forms for the cathodes of SICs.[124, 166-170] In addition, other heteroatom-rich carbon materials also have been developed as not only the anode but the cathode of SICs.[171] Regulating the properties of carbon materials is urgently needed in terms of Raman I_G/I_D ratio, heteroatom dopants, surface area, and porosity.

2.5.2 MXenes

2D layered transition metal carbides and carbonitrides are defined as the MXenes. This type of material was first identified as cations host by Gogotsi and his co-workers. The general formula of MXenes is $M_{n+1}XnT_x$, where M is the metal element (such as Ti, V, Cr, Nb, Mo, et al.), X is carbon or carbon and nitrogen elements, T is the light elements (such as H, O, F, et al.).[172, 173] MXenes usually are synthesized by processing the ternary carbides, or nitrides (MAX phase). The MAX phase is composed of layered transition metal carbides or nitrides that are inserted with layered A-element atoms (such as Al, Si, Sn, In, et al.). After selectively etching and removing A layers from the MAX phase, the MXenes with large interlayer spacing can be obtained, which is suitable for hosting large-size sodium or potassium ions. As illustrated in Figure 2-9, a typical MXene, V_2CT_x, is synthesized starting from V_2AlC, then using HF to remove the Al layers. Finally, $V_2C(OH)_x(O)_y(F)_z$ with a series of fluorinated and oxygenated surface functional groups is fabricated. The presences of the -OH, -O, and -F are

noted as T_x.[174] As we know, MXenes can work as both capacitive-type cathode and capacitive-type anode for HICs.[175, 176]

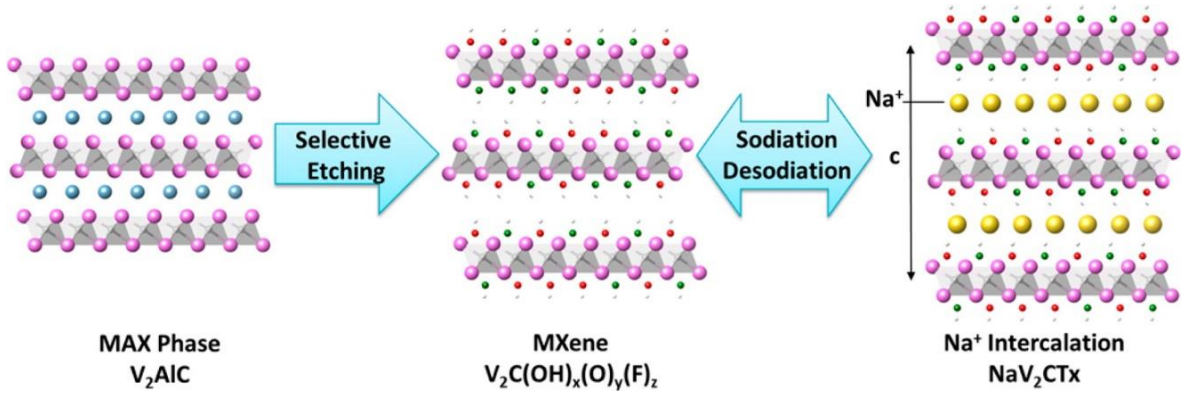

Figure 2-9 Schematic illustration of synthesis of V_2CT_x and its sodium intercalation.[174]

2.5.3 Ceramic intercalation materials

Ceramic intercalation materials as conventional battery-type cathodes also have been studied for the cathodes of SICs and PICs. They are generally coupled with carbon anodes, exhibiting a high energy density with slop voltage profiles. This type of material contains a transition metal element, like manganese, vanadium, iron et al. They commonly possess a diversity of stable oxidation states (eg. Mn^{2+}, Mn^{3+}, Mn^{4+}, V^{2+} $V3^{+}$, V^{4+}, V^{5+}, etc.), multi-channel crystal structure, morphology.[177-180] Those properties are favorable for hosting ions with high voltage output. As shown in Figure 2-10a and 2-10b, the lattice structure of $Na_{0.44}MnO_2$ shows large-size tunnels that can readily accommodate sodium ions.[181, 182] It exhibits a high volumetric discharge capacity of 286 mAh cm^{-3}.[183] Another representative battery-type cathode is $Na_3V_2(PO_4)_3$, which is a compound of Na^+ superionic conductor (NASICON). As shown in Figure 2-10c, its 3D open structure consists of PO_4 tetrahedra and VO_6 octahedra, providing large channels for hosting sodium ions. The multistep redox reaction among V^{2+}/V^{3+} and V^{3+}/V^{4+} endows $Na_3V_2(PO_4)_3$ with slop voltage profiles and high specific capacity (Figure 2-10d and 2-10e).[179, 184]

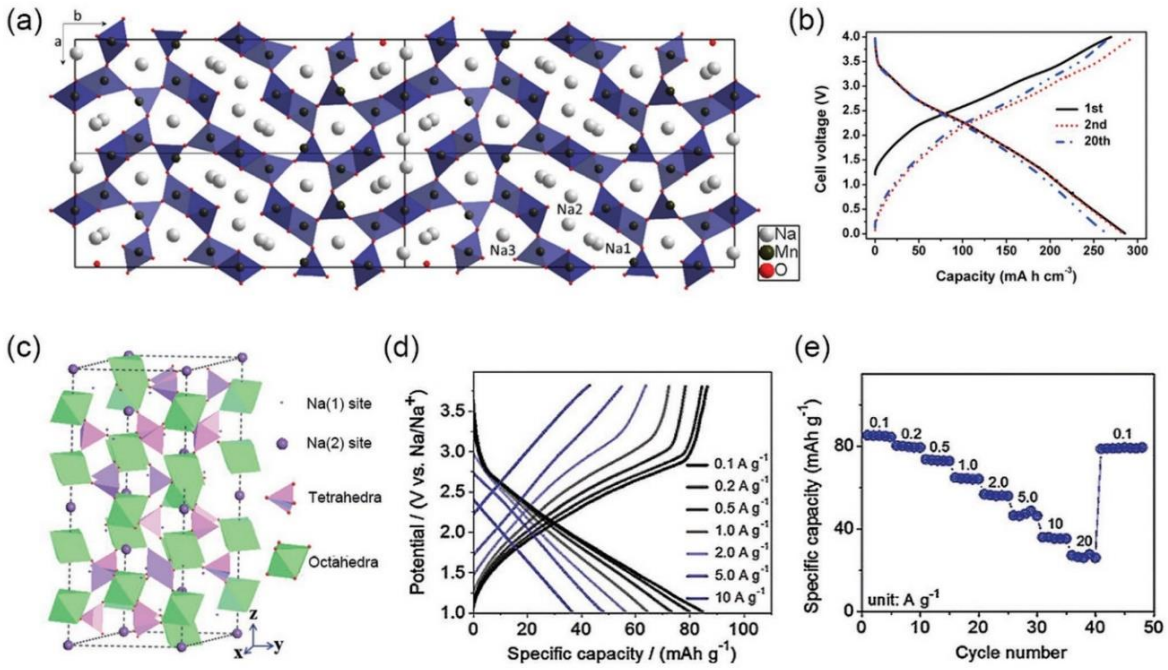

Figure 2-10 (a) Schematic crystal structure of $Na_{0.44}MnO_2$ perpendicular to the *ab* plane.[181] (b) Charge-discharge curves of NIC with $Na_{0.44}MnO_2$ cathode.[183] (c) Schematic illustration of $Na_3V_2(PO_4)_3$ crystal structure.[179] (d) Charge-discharge profiles and (e) rate performance of NIC with $Na_3V_2(PO_4)_3$ cathode.[184]

2.6 Electrolytes

As the ionic bridge to connect cathodes to anodes, electrolytes play a crucial role in electrochemical energy storage devices, including electrochemical capacitors and batteries. They are also critical to determine the electrochemical behaviors in terms of reversible ion storage capacity, cyclability, rate capability, and safety. Designing or utilizing an electrolyte with high ion conductivity, low viscosity, good thermal stability, and a wide voltage window can significantly improve the electrochemical performance of SICs and PICs.[185] So far, various electrolytes have been investigated for NICs, including aqueous, organic, ionic liquid, and solid-state electrolytes. In fact, the electrolytes utilized in SICs and PICs are usually the same as those in SIBs and PIBs. Among the above four electrolytes, aqueous electrolytes have the advantages of high ionic conductivity (~1.0 S cm^{-1}), cost efficiency, and safety.[135, 186] However, due to the low potential of the decomposition reaction of water, the HICs with aqueous electrolytes are limited to the voltage window of 1.23 V.[187] The energy density is suppressed. The ionic liquid electrolytes can provide wide voltage windows and a stable solid electrolyte interface (SEI). They have the advantages of low volatility, nonflammability, and

high ignition temperature.[188, 189] Nevertheless, ionic liquid electrolytes are still subjected to high cost, high viscosity, and unstable physicochemical properties. The solid-state electrolytes are still in their infancy for SICs and PICs. The solid-state electrolytes can't contact electrodes as tight as the liquid electrolyte, which reduces the accessibility of ions to the electrode materials' surface thus suppressing the fast ion-adsorption/desorption kinetics. This drawback restricts the power density output of HICs.

Currently, the majority of SIC and PIC electrolytes are organic electrolytes, which are made up of sodium- or potassium-ion-based salts and ester-based or ether-based organic solvents.[14, 73] The common salts in organic SIC and PIC electrolytes are sodium perchlorate ($NaClO_4$), Sodium hexafluorophosphate ($NaPF_6$), potassium hexafluorophosphate (KPF_6). The commonly used ester-based solvents include ethylene carbonate (EC), diethyl carbonate (DEC), propylene carbonate (PC), dimethyl carbonate (DMC), and ethyl methyl carbonate (EMC). The commonly used ether-based solvents include ethylene glycol dimethyl ether (DME), diethylene glycol dimethyl ether (DEGDME), tetraethylene glycol dimethyl ether (TEGDME). These solvents are usually utilized alone or in a mixture formed with different proportions.[190, 191] Additionally, fluoroethylene carbonate (FEC) sometimes is used as an additive to form a suitable SEI.[192] The knowledge of electrolyte application mainly comes from the investigation in battery research, and most of them are focusing on stabilizing the SEI formation.

3 Scope and target of this thesis

3.1 Dual-carbon capacitors

In recent years, developing sustainable electrochemical energy storage technologies has drawn much attention due to the environmental concern, resource shortage, and cost-efficiency pursue. To meet this expectation, the future SICs and PICs must be composed of components that are inexpensive, earth-abundant, and environmentally friendly. Carbon materials that are obtained from abundant carbonaceous materials with a minimum-energy-consumption process are an attractive low-cost and sustainable choice for SIC and PIC electrodes. Excitingly, carbon materials can be utilized not only as anodes but also as cathodes for SICs and PICs according to the above review of the anode and cathode developments in SICs and PICs. This circumstance is different from the battery electrode pairs. Constructing dual-carbon PICs and SICs is achievable.

In this thesis, two asymmetric dual-carbon PICs are assembled and investigated in chapter 4 and chapter 5. One symmetric dual-carbon SIC is assembled and investigated in chapter 6. For the first one, a high-performance oxygen-containing carbon nanofibers cathode is synthesized by a rational oxygen functionalization engineering, thereafter, a full dual-carbon PIC is configurated by utilizing the oxygen functionalized carbon as the cathode and its carbon precursor as the anode. For the second one, it demonstrates that graphite oxide cathode and pure graphite anode both have high rate capability in DME electrolyte. Inspired by this advantage, a fast dual-carbon PIC is configurated by the graphite oxide cathode and the pristine graphite anode. For the third one, it is found that the reduced graphite oxide also has a high rate capability and long cyclability for the anode of SIC in sodium-salt-based DME electrolyte. Therefore, a dual-carbon SIC is configurated by using reduced graphite oxide as both anode and cathode. It is worth noting that the carbon anode and the carbon cathode in each HIC are derived from the same resource, which is a highly recommendatory cost-efficiency strategy. As illustrated in Figure 3-1, the carbon cathode mainly stores both anions and cations, and the carbon anode only stores cations. This diagram is the full PIC configured by the graphite oxide cathode and graphite anode in DME electrolyte.

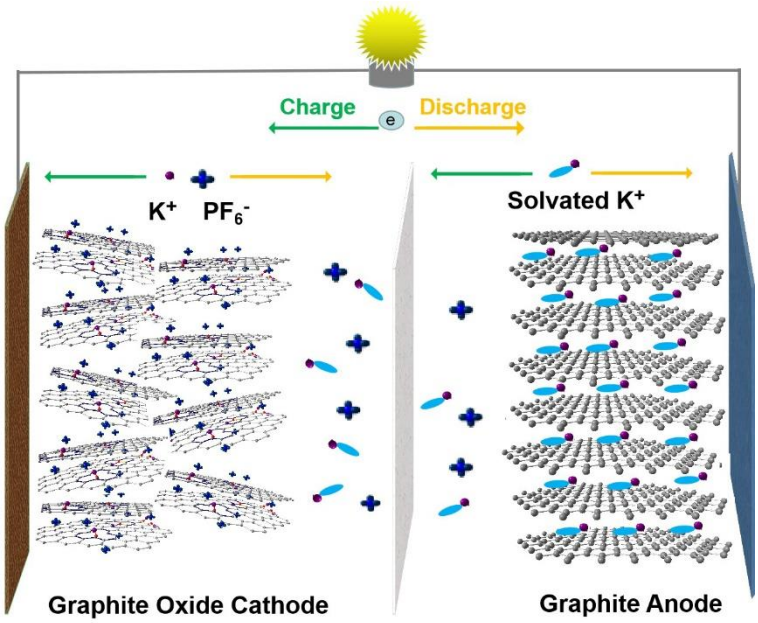

Figure 3-1 Illustration of the dual-carbon potassium-ion capacitor configurated by graphite oxide cathode and graphite anode in DME electrolyte.

3.2 Carbon cathode: Oxygen functionalization engineering

Inspired by the carbonyl-containing organic cathodes that utilize the redox reaction between oxygen functional groups and alkaline ions, i.e., $–C=O + e^- + M^+ \leftrightarrow –C–O–M$ (M represents alkaline ions), to realize reversible ion storage in LIBs, SIBs, and PIBs. Oxygen-containing functional groups also are introduced as the active sites for the carbon cathodes of PICs. Regulating oxygen-containing functional groups is an efficient strategy to enhance the ion storage of carbon cathodes. It is critical to have the ease to modify the surface of carbons with a large amount of oxygen functional groups. The edges of the graphene layers in carbons tend to show a higher chemical reactivity than the graphitic bases (the aromatic rings). Creating more edges of graphene layers is expected to increase the ease of surface functionalization. However, a few works have been reported for the PIC research so far, such as soft carbon,[86] $Ca_{0.5}Ti_2(PO_4)_3$@C,[134] $K_2Ti_6O_{13}$,[133] Nitrogen-doped $MoSe_2$/Graphene,[152] Oxygen-rich carbon nanosheets,[156] porous MXenes,[176] Onion-like carbon,[90] $FeSe_2$/N-C,[151] 3D nitrogen-doped framework carbon,[111] and AC-HC.[88] Most of them focus on developing anode materials for PICs, while active carbons (commercially available rather than lab-made samples) are commonly employed as cathodes. Therefore, from our point of view, searching for new cathode materials of PICs, especially for low-cost carbon cathode materials is

extremely urgent and present a timely issue for PIC research. Moreover, the mechanism investigation of potassium-ion adsorption on carbon cathode is rarely reported.

In this thesis, it is worth expecting that a soft carbon with lots of defects and a high degree of graphitization could be a better precursor to obtain an oxygen functionalized carbon for ion adsorption of the carbon cathode (Figure 3-2). Furthermore, through the control experiments, the understanding of the potassium-ion adsorption of the oxygen functional groups in carbon materials is further enhanced, which is crucial for PIC cathode research.

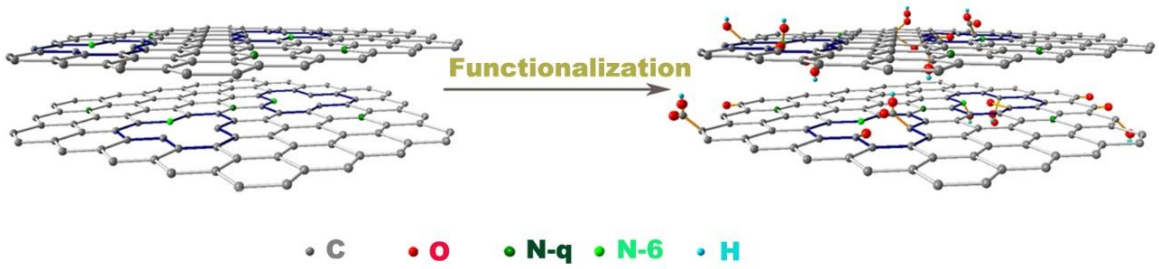

Figure 3-2 Illustration of oxygen functionalization of nitrogen-doped carbon.

3.3 Electrolyte identification

Most research of the hybrid ion capacitors, including LICs, SICs, and PICs is mainly focusing on developing new structures and new materials of the electrodes. The role of the electrolyte has not been identified. Until now, only a few works devoted their efforts to the electrolyte investigation in LICs and SICs. They prefer to optimize the SEI formation for the battery-type anodes by regulating the concentration of the electrolyte, adding addictive, and adjusting the combination of electrolyte salts or solvents. The effects of different electrolytes on the ion storage of cathodes are urgent to be investigated. It is because the carbon cathodes usually store both cations and anions in hybrid ion capacitors while the anodes only store cations. The energy storage mechanism of the capacitor carbon cathode is much different from that of the battery cathode. Thus, it can't directly learn from the batteries' electrolyte research, though they usually use the same electrolytes. The research in this field is still limited.

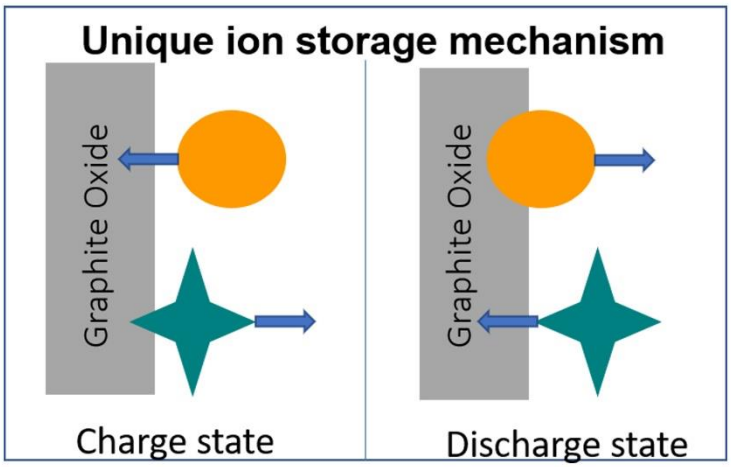

Figure 3-3 The charge and discharge process of the carbon cathodes in PICs.

According to the previous work in SICs and PICs, the cations adsorption and anions desorption occur during the charging process, and the anion adsorption and cation desorption occur during the discharging process.[88, 193] The anions and cations always diffuse in the opposite direction (Figure 3-3). The interaction between cations and anions plays a critical role. The cations and anions in different solvents have different capabilities of ion diffusion in the electrolytes and at the interface of the electrolyte/electrode. Therefore, it is significantly necessary to discuss the effects of different electrolytes on the ion storage of PHIC cathodes. Among all the electrolytes utilized in PIBs, KFP_6 is the most common solute, ethylene carbonate and diethyl carbonate (EC/PC), ethylene carbonate and propylene carbonate (EC/DEC) are the most common ester solvents, and dimethyl glycol (DME) is the most common ether solvent. A systemic understanding of the electrochemical characteristics in these three electrolytes is urgently needed to reveal the relationship between the electrolytes and performance for PICs. In this thesis, the target is to reveal the effect of the interaction between the cations and anions in ether and ester electrolytes for the dual-ion storage of carbon cathode.

3.4 Carbon anode: mechanism optimization

Carbon materials are the most popular candidates for the battery-type anodes of HICs. Currently, there are three different ion storage mechanisms. First, the graphitic carbons with ordered carbon layers can’t store sodium ions but potassium ions through the single-ion intercalation (Figure 3-4a). The diffusion and storage of potassium ions occur in (002) orientation of the ordered carbon layers. Generally, this reaction mechanism exhibits slow ion

storage kinetic due to the fewer exposures of the (002) orientation on the surface of graphitic carbon and the large size of potassium ions. Second, the graphitic carbon can store both sodium ions and potassium ions through the co-intercalation in ether electrolyte (Figure 3-4b). This reaction mechanism possesses high rate capability and great cyclability owing to the thermodynamic and chemical stability of the ion-solvent complexes in graphite layers and the fact that the complex avoids a sluggish desolvation process. However, due to the large size of the ion-solvent complex, only a low specific capacity can be obtained intrinsically. Third, carbon materials with abundant defects can store ions through adsorption (Figure 3-4c). The ion storage performs in three different forms: (i) the adsorption on defective sites, functional groups in a slop high voltage range, (ii) the adsorption on the randomly distributed carbon nanosheets in a slop medium voltage range, (iii) the pore filling in the nanovoids between the carbon layers in a low voltage plateau. This ion storage mechanism usually exhibits high rate capability because of the easily accessible active sites of capacitive-like redox reaction and fast ion diffusion kinetics.[72] However, the fast ion storage mechanism cannot completely utilize the carbon active sites, some ordered carbon layers in the defective carbon materials cannot store ions at high current density, which is a huge waste for enhancing the specific capacity. To better make use of these carbon layers, we would like to introduce the co-intercalation of the ion-solvent complexes as an additional ion-storage mechanism.

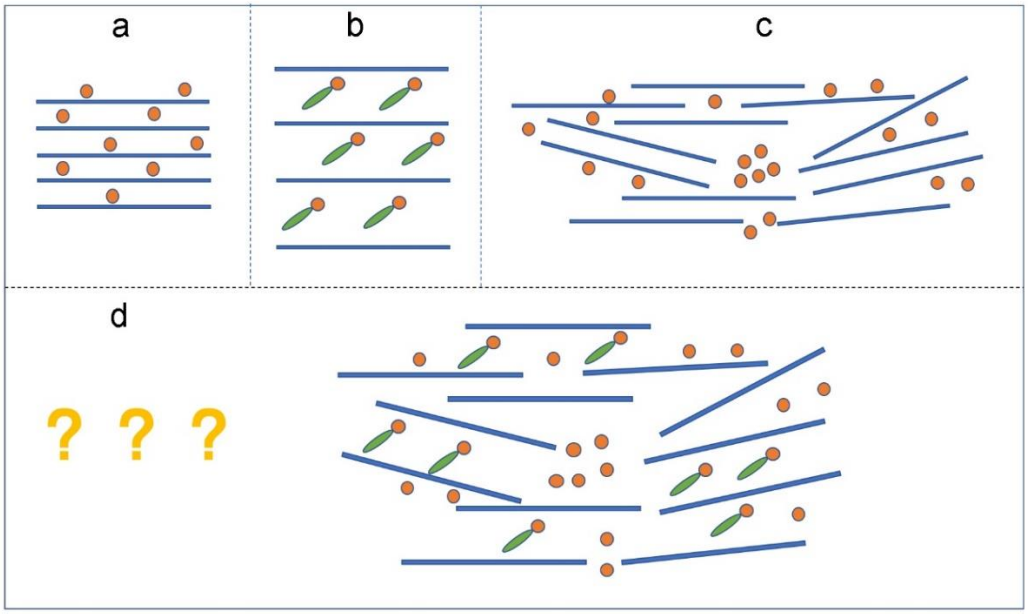

Figure 3-4 Illustration of the ion storage mechanisms for the carbon anodes.

In this thesis, a combination of adsorption mechanism and co-intercalation mechanism is proposed to realize both great rate capability and high specific capacity (Figure 3-4d**).** Carbon materials accommodate the sodium ions by a fast capacitive-like adsorption mechanism and a co-intercalation mechanism. The output voltage window based on this kind of mechanism is sloping, which is a rather anode of SICs than the anode of batteries. It coincidentally meets the requirement of pursuing high energy density and power density for SICs.

4 Oxygen functionalized carbon nanofibers as cathode of PICs

Based on our proposal, it is critical to have the ease of modifying the surface of the carbons with a large amount of oxygen functional groups. Creating more edges of graphene layers is expected to increase the ease of surface functionalization. Our previous work of PIB anodes has demonstrated that nitrogen-doping can effectively create defects on the graphene layers of carbons, which induces more edges of the layers. It encourages us to use nitrogen-doped carbons as a starting material to perform oxygen functionalization. In this chapter, by modifying nitrogen-doped carbon nanofibers (NC) using a solution of mixed strong acids, the oxygen-functionalized carbon nanofibers (ONC) are fabricated as PIC cathodes. The oxygen-containing functional groups are chemically bonded at the graphene edges, resulting in reversible storage of potassium ions in a high voltage window through surface faradic reaction. The ONC electrode exhibited a high reversible specific capacity and great rate capability. The electrochemical storage mechanism is investigated, and it reveals that the large reversible capacity and excellent rate capability are owing to a large surface-controlled capacity which is mainly realized by faradic reaction between K^+ and C=O. Furthermore, a cost-effective and "green" full PIC is demonstrated based on the ONC cathode and NC anode. This work manipulates one carbon material into both cathode and anode materials and paves a new approach for obtaining the PIC cathode materials.

4.1 Experimental section

4.1.1 Nitrogen-doped carbon nanofibers (NC) preparation

The nitrogen-doped carbon nanofibers were synthesized by a facile method reported in our previous work.[194] In a typical process, 0.8 g cetrimonium bromide (CTAB, $(C_{16}H_{33})$-$N(CH_3)_3Br$) was dissolved in 240 mL of 1 mol L^{-1} hydrochloric acid solution. After the formation of a transparent solution, 1.2 g ammonium persulfate (APS, $(NH_4)_2S_2O_8$) was then added to the above solution. A homogeneous white suspension was formed under magnetic stirring for 30 min. 1.6 mL pyrrole monomer was then dropwise added into the white suspension, and the polymerization was conducted in the ice bath (0–3℃) for 3 h under strongly stirring. Subsequently, a black precipitate of polypyrrole (PPy) was collected by filtration and washed with deionized water until the filtrate became colorless. The PPy precursor was dried at 80 ℃ in a vacuum oven for 24 h, and NC was obtained by annealing it at 1100 ℃ in N_2 atmosphere with a ramp rate of 5 ℃ min^{-1} for 2 h.

4.1.2 Oxygen-functionalized carbon nanofibers (ONC) preparation

In brief, 20 ml mixed strong acids solution of H_2SO_4/HNO_3 (vol. 3/1, 96% and 70%, respectively) was prepared in a 50 mL round-bottom flask. 150 mg as-prepared NC was then added into the acid solution and kept the flask in the oil bath at 50 ℃ under mild magnetic stirring for 1 h. After diluting the mixed solution, the ONC was washed until the solution became neutral and dried in a vacuum oven at 80 ℃ for 24 h before use. The comparison samples of ONC650, ONC800, and ONC950 were obtained through annealing PPy precursor at 650, 800, and 950 ℃ respectively, then conducting the oxygen functionalization with the same conditions. The oxygen functionalized active carbon material (OAC) and carbon nanotubes (OCNT) were obtained by the functionalization with commercial active carbons and carbon nanotubes.

4.1.3 Materials characterization

The scanning electron microscopy (SEM) was carried out on a Hitachi 434 S4800 to observe the morphology of the samples. The transmission electron microscopy (TEM) and elemental mapping were carried out on a JEOL JEM-435 2100F to analyze the construction of the samples. The crystal features of the samples were identified with the X-ray diffraction (XRD) pattern using an 18 KW D/MAX2500V PC diffractometer at a scan rate of 2° min^{-1}. The X-

ray photoelectron spectra (XPS) analysis was acquired with a Thermo 436 SCIENTIFIC ESCALAB 250Xi using an Al Kα (hυ = 1486.8 eV) as the excitation source. The Raman spectra analysis was carried out using an inVia Raman microscope with He-Ne laser (532 nm). Fourier transform infrared (FTIR) spectra were performed on an AVATAR 370.

4.1.4 Electrochemical measurements

The electrodes were fabricated by mixing 80 wt% as-synthesized carbon materials, 10 wt% Super P, and 10 wt% polyvinylidene fluoride (PVdF). Then, the slurry was coated on a copper foil using the doctorblade that controlled the loading mass of active materials to around 2.0 mg cm^{-2} and kept the foils in a vacuum oven at 110 ℃ for 12 hr. The electrochemical properties were measured using coin-cell configurations (CR 2032) which were assembled in an Ar-filled glove box. The electrolyte of 0.8 M KPF_6 in ethylene carbonate and propylene carbonate (*vol.* EC/PC = 1/1) also was prepared in the glove box. The separator was a glass microfiber filter (Whatman, Grade GF/B). The potassium foil was used as counter electrodes for the half cells. CV tests were carried out with various scan rates on a VSP electrochemical workstation (Bio-Logic, France). Galvanostatic charge/discharge tests were performed on a Land CT 2001A 449 battery testing system (Land, China) under different current densities at ambient temperature. For the full cell, the NC without functionalization was used as the anode electrode. The cathode limited configuration was used to prepare the anode and cathode films. The mass-loading ratio is around 1.3.

4.2 Results and discussions

4.2.1 Morphological and structural characterizations

The ONC nanofibers were obtained by a mixed-acid treatment of the NC nanofibers. The SEM images with different magnifications of the NC material and oxygen functionalized ONC material are shown in Figure 4-1. Figure 4-1a shows that the NC nanofibers display a 3D network structure. The nanofibers are formed uniformly, the sizes of carbon nanofibers are similar (Figure 4-1b). As shown in Figure 4-1c and 4-1d, the carbon nanofibers of ONC after the oxygen functionalization preserve the morphology of NC, suggesting that it has a minimal effect on the morphology of the carbons to functionalize them with the oxygen groups.

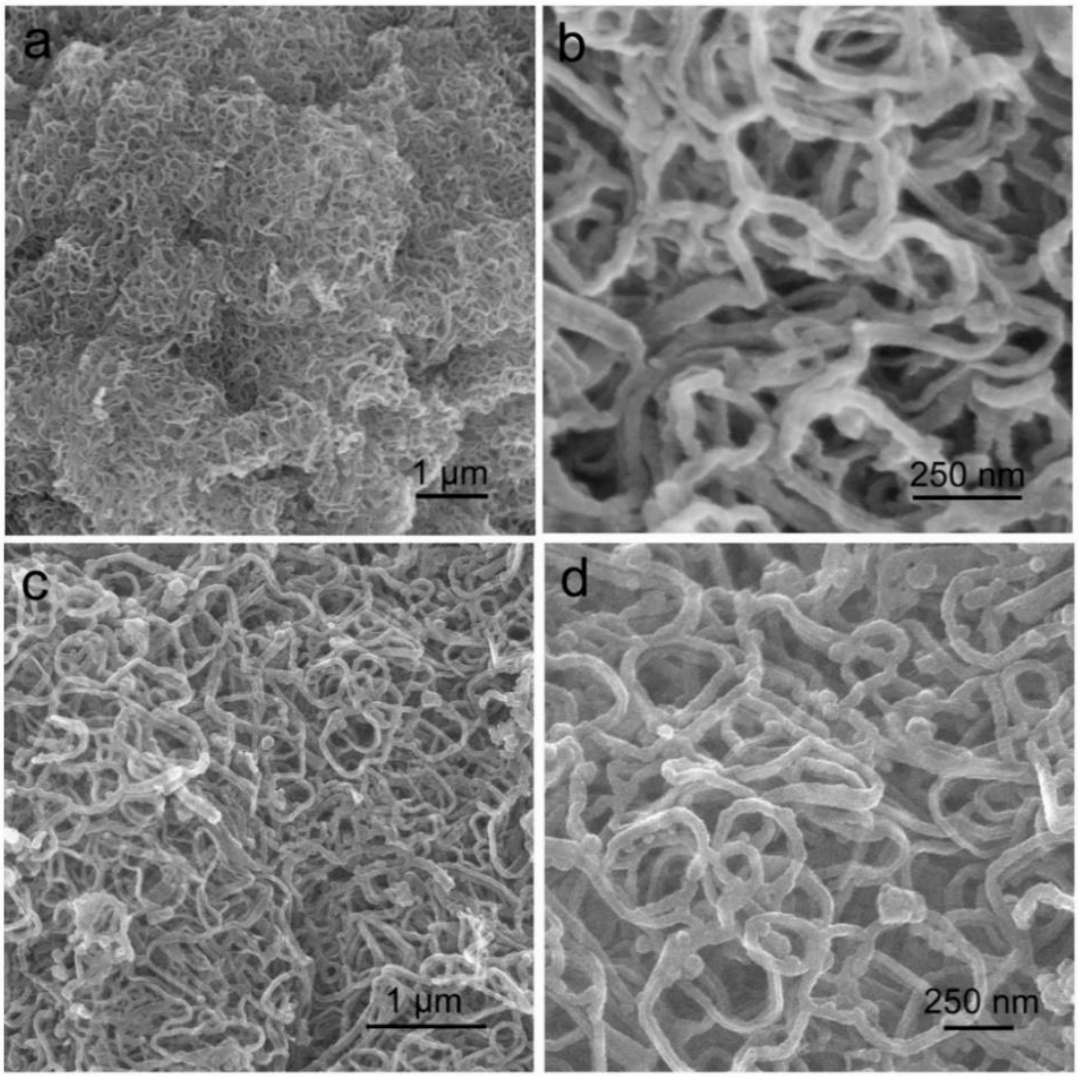

Figure 4-1 3D network carbon nanofibers (a) and (b) before, (c) and (b) after oxygen functionalization.

Figure 4-2a presents the high-magnification SEM image of ONC and shows that this 3D network consists of nanofibers with an average diameter of about 80 nm. The TEM image in Figure 4-2b further reveals the hollow inner of the ONC nanofibers. The thickness of the sidewalls is about 25 nm, forming tubes with an inner diameter of 30–40 nm. Such a 3D network assembled by the interconnected hollow nanofibers makes surface-reaction and electron transport effective. The high-resolution TEM (HRTEM) image in Figure 4-2c shows ONC possesses many micro-areas where short-range ordered graphene layers can be found. The micro-areas are separated by the micropores that can be considered as carbon defects, which creates abundant graphene edges. Thus, the redox-active oxygen groups can be easily functionalized.[195] As shown in the element mapping images (Figures 4-2d–g), carbon and oxygen distribute evenly over the entire nanofiber, further confirming the successful functionalization of the oxygen groups. The incorporation of oxygen also reduces the amount of nitrogen compared with NC.

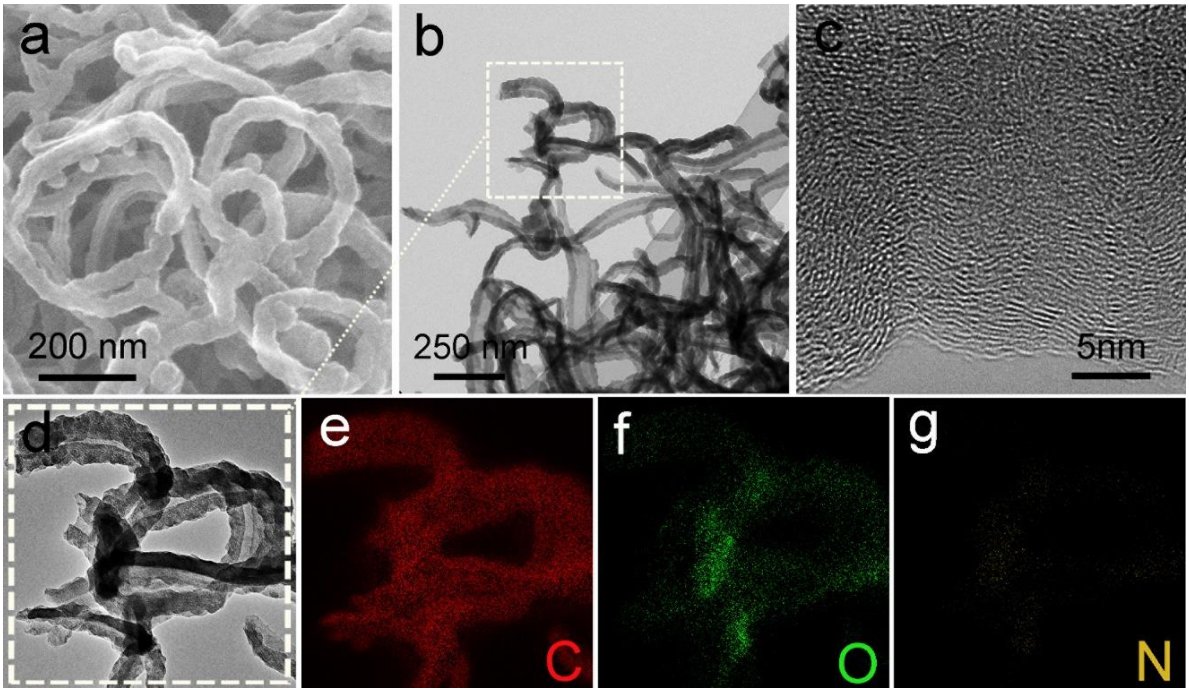

Figure 4-2 Structure characterization of ONC by electron microscopes. (a) SEM image. (b) TEM image. (c) HRTEM image. (d-g) Images of element mapping of C, N, O.

The structure of ONC and NC were studied by the characterizations of XRD, Raman spectroscopy, FTIR spectroscopy, and XPS spectroscopy. XRD patterns in Figure 4-3a show that both ONC and NC possess two peaks at around 25°and 43°, corresponding to (002) and

(101) planes of a disordered carbon, respectively. Upon functionalization, the oxygen functional groups modified at various locations on both sides of graphene layers can induce distortion of the inter-planar space, resulting in the widening of the diffraction peaks. The (002) peak of ONC shifts from 26° to 24°, indicating the expansion of the inter-planar spacing caused by the oxygen functional groups.[77] The Raman spectra of ONC and NC in Figure 4-3b both exhibit broad disorder-induced D-band located at 1353 cm^{-1}) and in-plane vibration G-band located at 1579 cm^{-1}.[193] The ratio of I_G/I_D generally is used to verify the graphitization degree of amorphous carbon materials (I_G and I_D are obtained from the absolute heights of the peaks). The calculated value of I_G/I_D decreases from 1.04 for NC to 0.94 for ONC after the functionalization, indicating a higher disordering degree of ONC, agreeing with the XRD results.

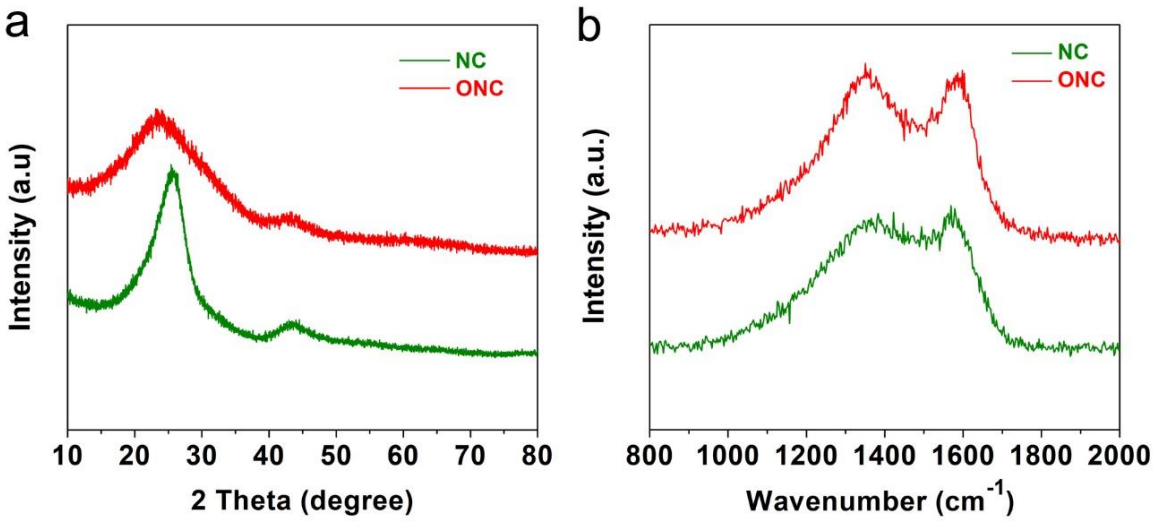

Figure 4-3 Structure characterizations of ONC and NC by spectroscopes. (a) XRD patterns. (b) Raman spectra.

4.2.2 Investigation of the chemical composition of NC and ONC electrodes

The FTIR spectrum of NC in Figure 4-4a exhibits the overlapping bands in the range of 1500-1600 cm^{-1}, corresponding to the C-sp^2 hybridization. It suggests the existence of abundant amounts of aromatic domains in NC material. In the spectrum of ONC, the overlapping bands located in the range of 750-1500 cm^{-1} are assigned to the C-O, C-O-C, and O-H vibrations. The peak of the ONC spectrum between 1600 and 1700 cm^{-1} corresponding to the COOH and C=O modes becomes much sharper, and there is a presence of a peak around 3400 cm^{-1}, which both suggest the existence of considerable oxygen functional groups in ONC material.[196, 197]

According to the comparison of the FTIR spectra, it confirms that oxygen-containing groups have been chemically bonded with the edges of the carbon rings after the functionalization. The XPS survey spectra in Figure 4-4b show a dramatic increase of the intensity of O1s peak in ONC, further demonstrating that the oxygen functionalization process is realized. The content of oxygen increases from 1.1% to 9.8%, meanwhile the composition of the C=C bond decreases from 75.8% to 69.9%. The results shall be the consequences of the harsh oxidation and destruction of the C-sp^2 aromatic structure of graphitic edges in the strongly oxidizing solution. A slight reduction in nitrogen content may be ascribed to acid corrosion and the addition of oxygen atoms. Figure 4-4c displays the close observation of the C1s XPS spectra of ONC and NC. The peaks are fitted to five components located at 284.7, 285.6, 286.7, 288.2, and 290.1 eV, corresponding to the C-sp^2 (C=C), C-sp^3 (C-C, C-O, C-N), C=O, COOH, and N-C=O groups, respectively.[198, 199] It is noted that the relative content of oxygen functional groups (C=O and COOH) increases in ONC, as compared with NC. As shown in Figure 4-4d, the analysis of the close observation of the C1s XPS spectra shows that the contents of C=O groups, C-O-C/C-OH groups, and COOH groups are about 36%, 45%, and 19%, respectively. It suggests that both C=O groups and C-O-C/C-OH groups play a crucial role in the K-ion storage. The ONC contains only N-6 and N-Q, and their content is sufficiently low (nearly 2%). Thus, it is not expected to meaningfully contribute to the charge storage capacity.

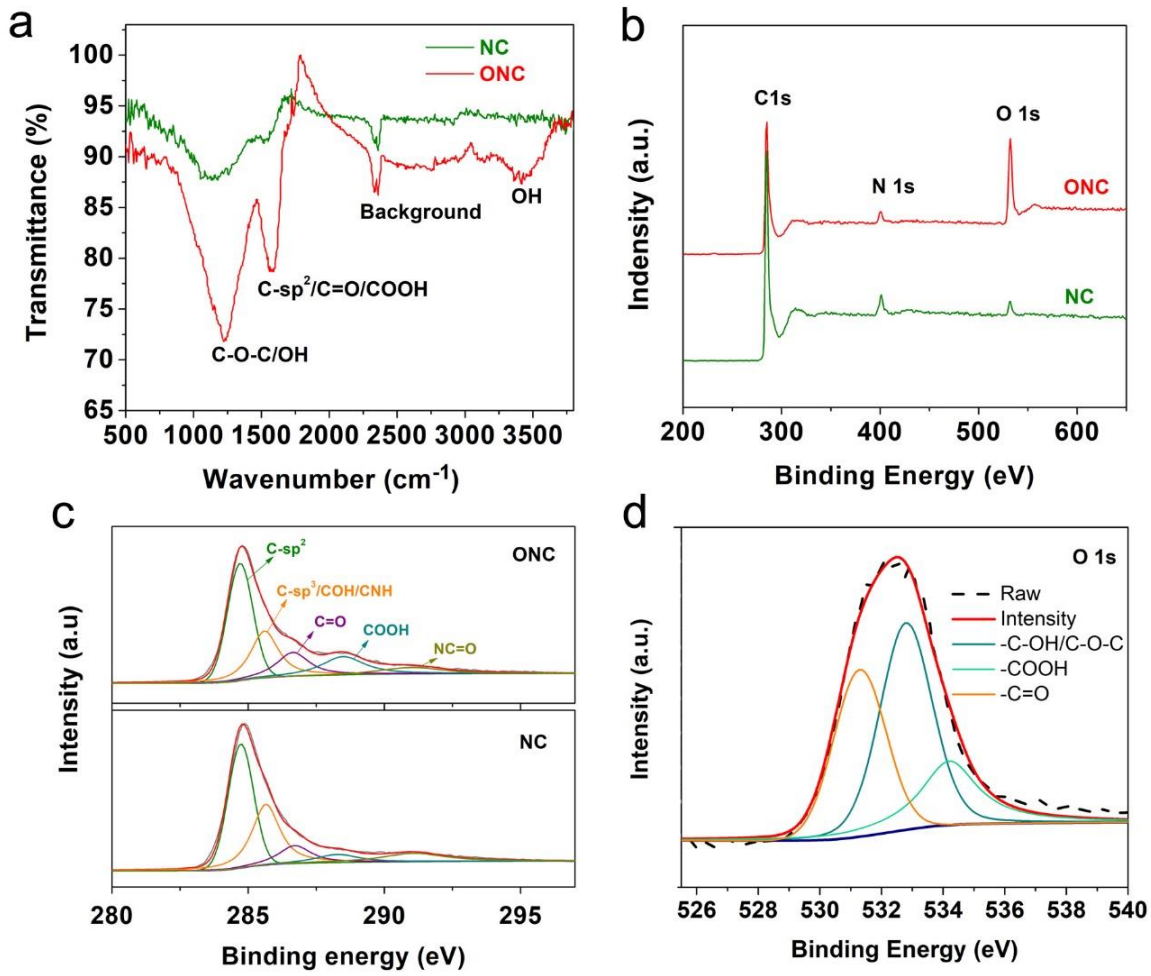

Figure 4-4 Chemical composition of NC and ONC. (a) FTIR spectra. (b) XPS survey spectra. (c) C 1s and (d) O 1s core level of XPS spectra.

4.2.3 Investigation of electrochemical performance of NC and ONC electrodes

To confirm that the oxygen functional groups are responsible for the charge storage, the electrochemical behaviors of NC and ONC are investigated in half cells in a voltage window of 1.2–4.2 V. As shown in Figure 4-5a, the first discharge capacity of the NC electrode is about 37 mAh g^{-1} at the current density of 50 mA g^{-1}, meaning that the potassium-ion storage is limited. The second discharge capacity increases to about 52 mAh g^{-1} because of the additional PF_6^--anion desorption. Nevertheless, the NC electrode can only achieve a stable reversible capacity of about 40 mAh g^{-1} after 30 cycles (Figure 4-5b).

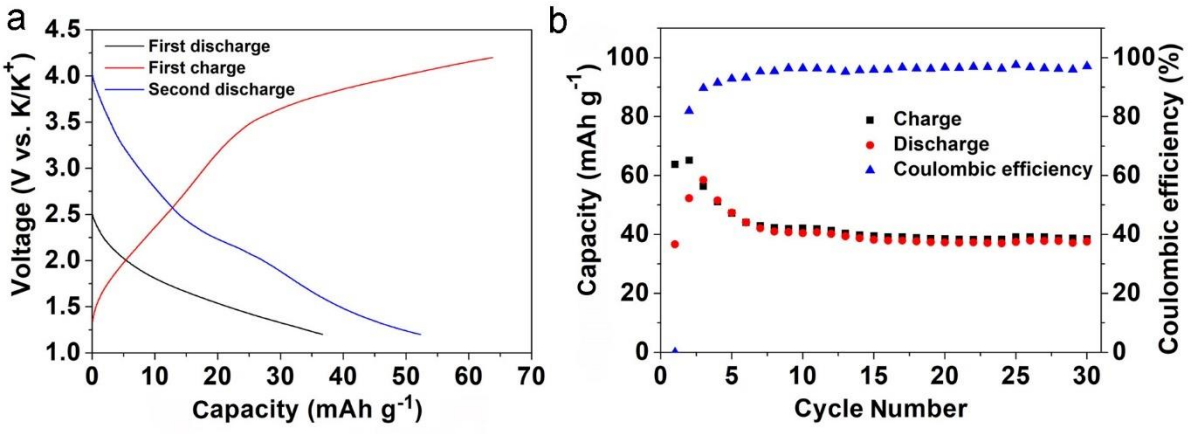

Figure 4-5 Electrochemical performance of NC cathode. (a) Charge-discharge profiles and (b) cycling performance at current density of 50 mA g^{-1}.

Subsequently, we carried out a complete electrochemical performance assessment for the ONC electrode after functionalized NC material, the cyclic voltammetry (CV) curves at a scan rate of 0.2 mV s^{-1} in Figure 4-6a display a quasi-rectangular shape with less defined peaks, suggesting the oxygen functional groups of ONC undergo a capacitive-like reaction which is responsible for electrochemical energy storage at the applied voltage window typically for cathode materials.[198] Figure 4-6b shows the cycling performance measured at a current density of 50 mA g^{-1}. The ONC electrode delivers a capacity of 130 mAh g^{-1} after 200 cycles, maintaining 70% of the discharge capacity of the 5th cycle. The coulombic efficiency (CE) increased to 95% after 10 cycles, demonstrating high reversibility of the charge storage derived from the reduction/oxidation of the oxygen functional groups. The obtained long-term reversible capacity is comparable or even higher than those of the conventional PIB cathodes (Table 4-1).

Table 4-1 Cycling performance comparison of as-prepared ONC nanofiber with conventional PIB cathodes.

Materials	**Current density/mA g^{-1}**	**Cycle number**	**Capacity retention/mAh g^{-1}**
This work	50	200	130
P2-Type $K_{0.6}CoO_2$[200]	100	120	40
$K_{0.7}Fe_{0.5}Mn_{0.5}O_2$ nanowires[201]	100	60	101
KVP_2O_7[202]	25	20	51
$K_xV_2O_5 \cdot nH_2O$ Nanobelts[203]	20	50	167
Crystalline PB nanocubes[204]	100	50	68
$K_{0.65}Fe_{0.5}Mn_{0.5}O_2$ Microspheres[205]	100	350	70
Prussian Blue Nanoparticles[206]	0.0017	2.3	1.5

As shown in Figure 4-6c and 4-6d, the charge-discharge processes are conducted by two different modes. The profiles display a sloping feature in the applied voltage window, which is consistent with the CV results and signals a surface-controlled charge storage mechanism. For the first charge mode, an initial charge capacity of 56 mAh g^{-1} is obtained, suggesting the concurrent occurrence of anion storage. While for the first discharge mode, the ONC delivers initial discharge and charge capacities of 160 and 224 mAh g^{-1}, respectively. The higher capacity of the charging process implies the contribution of both PF_6^--anion storage and potassium-ion storage to the total capacity.

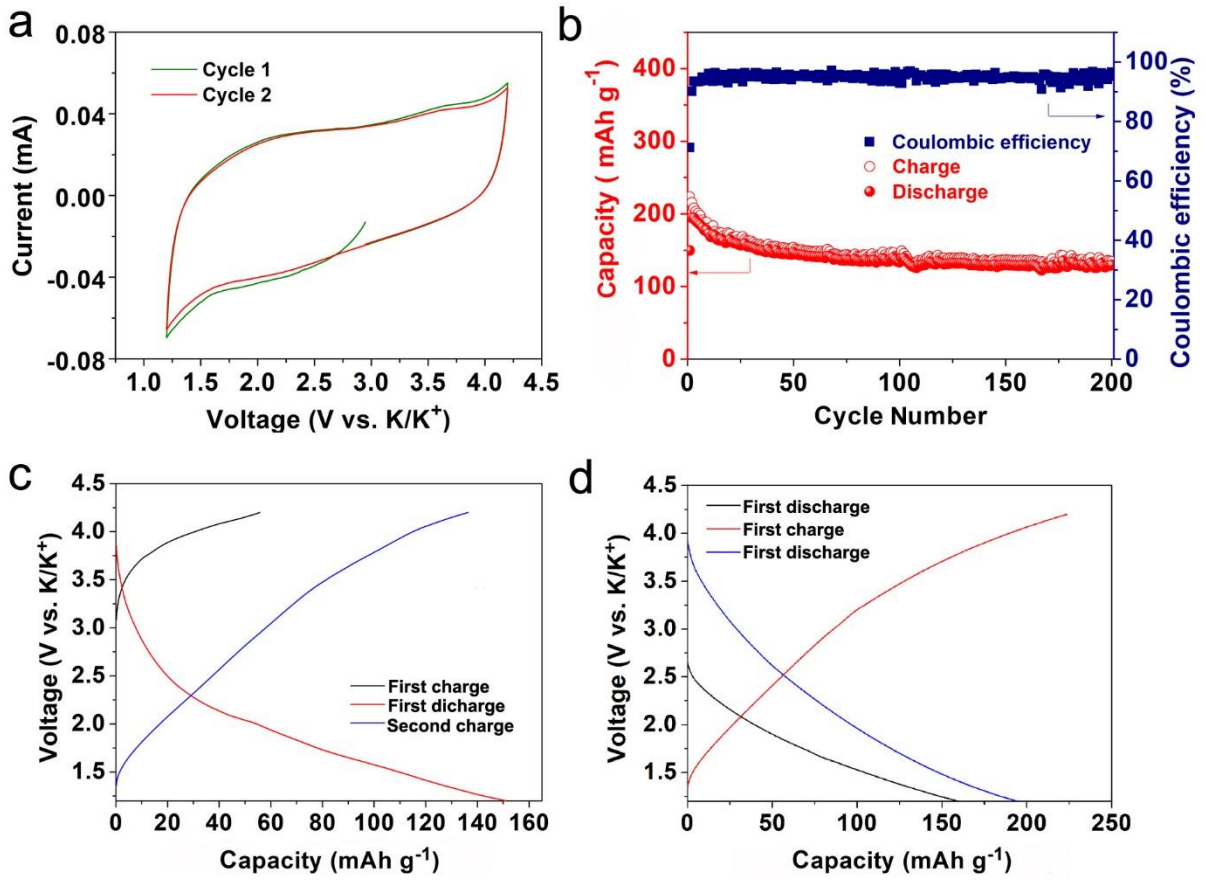

Figure 4-6 Electrochemical properties of the ONC electrode. (a) CV results at a scan rate of 0.2 mV s^{-1}. (b) Cycling performance at a current density of 50 mA g^{-1}. Galvanostatic test for (c) the first charge mode and (d) the first discharge mode.

The rate capability at various current densities is shown in Figure 4-7a. The ONC electrode exhibits reversible capacities of 194, 148, 123, 100, 85, 72, and 68 mAh g^{-1} at the current densities of 0.05, 0.1, 0.2, 0.5, 1.0, 2.0, and 5.0 A g^{-1}. The capacity recovers to 155 mAh g^{-1} when the current density is reduced back to 0.05 A g^{-1}. Moreover, it delivered a stable reversible capacity of 131 mAh g^{-1} for additional 50 cycles. The corresponding charge-discharge profiles are shown in Figure 4-7b. It reveals that almost no polarization between charging and discharging can be found, once again demonstrating that the oxygen functional groups enable the high reversibility and facile charge transport for the charge storage. Moreover, we investigated the ONC electrode at high current densities of 1.0 A g^{-1} and 2.0 A g^{-1}. As shown in Figure 4-7c, the capacity can remain 65 mAh g^{-1} after 1000 cycles and 48 mAh g^{-1} after 3000 cycles respectively. As previously pointed out, there have been very limited reports of conventional cathode materials that exhibit a practical capacity at 1.0 A g^{-1}. The

presented rate capability in our work not only shows a practical capacity at such a current density but also maintains among high capacities at the current densities well beyond 1.0 A g^{-1}.

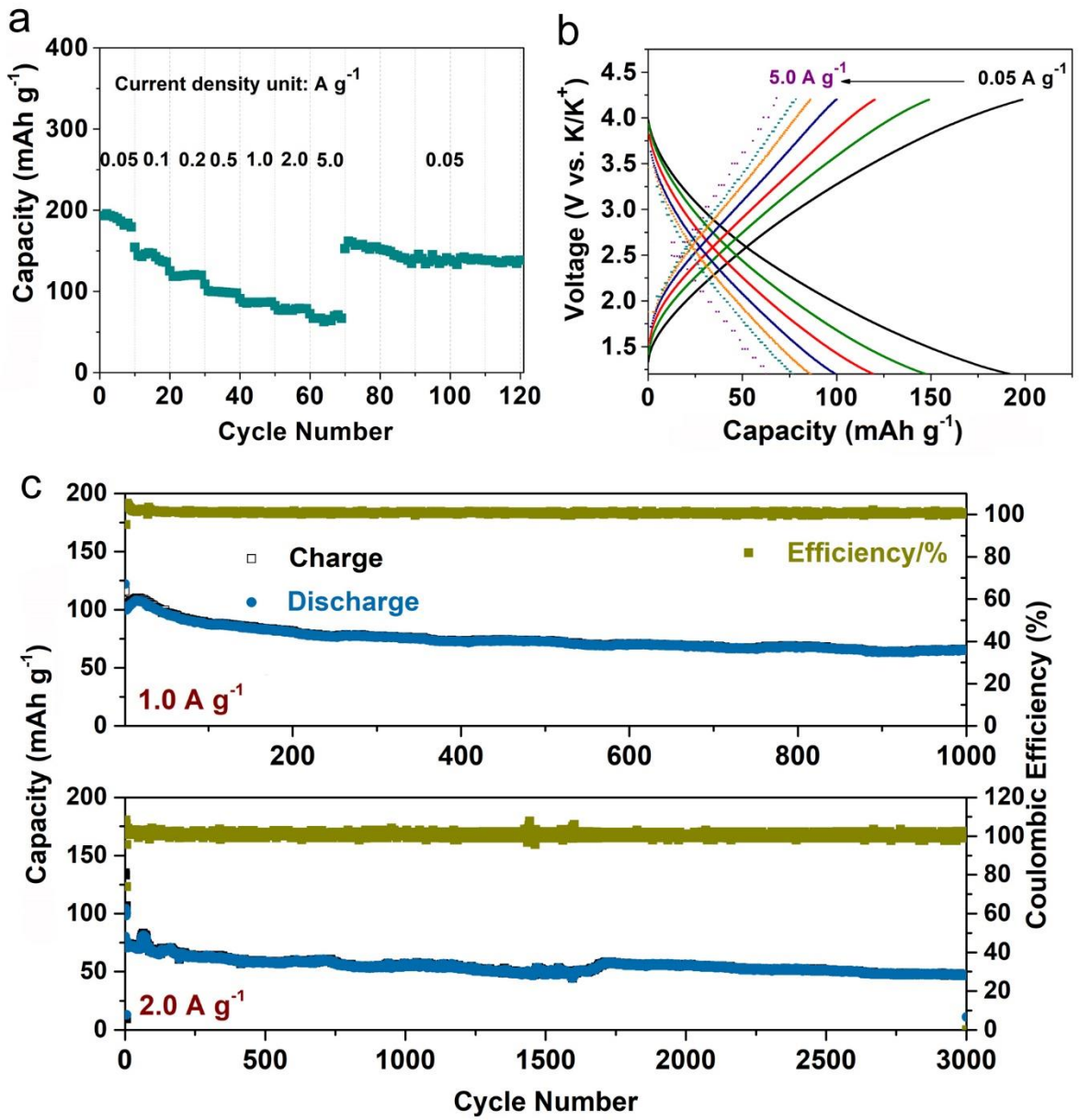

Figure 4-7 Electrochemical properties of the ONC electrode. (a) Rate capability at the current densities from 0.05 to 5.0 A g^{-1}. (b) Charge-discharge profiles at various current densities. (c) Cycling performance at the current densities of 1.0 and 2.0 A g^{-1}.

4.2.4 Undergoing electrochemistry of ONC electrode

To reveal the charge storage mechanism, we carried out the XPS measurement on the ONC electrode at different charge and discharge states. As shown in Figure 4-8a, the O 1s spectra can be fitted to three components of C=O, -OH/-O-, and COOH located at the binding energies of 530.2, 532, and 533 eV, respectively. The relative intensity of C=O to -OH/-O- decreases after the first discharge process and increases after the subsequent charge process. It is consistent with the redox reaction of -C=O - e ⇌ -C-O-, where the double bond of C=O is reduced to the single bond of C-O upon releasing an electron, while the opposite process occurs upon capturing an electron. It is worth noting that the relative intensity of C=O does not fully recover after the first charge process, presumably resulting from the competition between reversible and irreversible oxidation of the functional groups of -C-O- in ONC, which was observed in previous work.[207] Nevertheless, a significant decrease of the relative intensity after the second discharge process suggests a reversible reduction of C=O and thereby the reversible redox reaction can be confirmed. The results of the K 2p spectra shown in Figure 4-8b provide additional support to the presented charge storage mechanism of -C=O + K^+ - e ⇌ -C-O-K. The intensity of the peaks increases/decreases corresponding to each discharging/charging process, indicating the storage/release of K-ions by/from the oxygen functional groups, which is also in good agreement with the results of the O 1s. As we mentioned in the last section, anion storage also contributes to the overall charge storage. Since PF_6^- carries a negative charge, the change of its amount should be opposite to that of potassium ion. This phenomenon is exactly what we observed in the F and P spectra in Figure 4-8c, where the intensities of the F 1s, P 1s, and P 2p peaks all increase after the charging process and decrease after the subsequent discharge process.[87] However, the low absolute intensity and the relatively smaller change of F and P components compared with the O and K peaks undoubtedly suggest that the K-ion storage by the oxygen functional groups is the major contributor to the overall capacity.

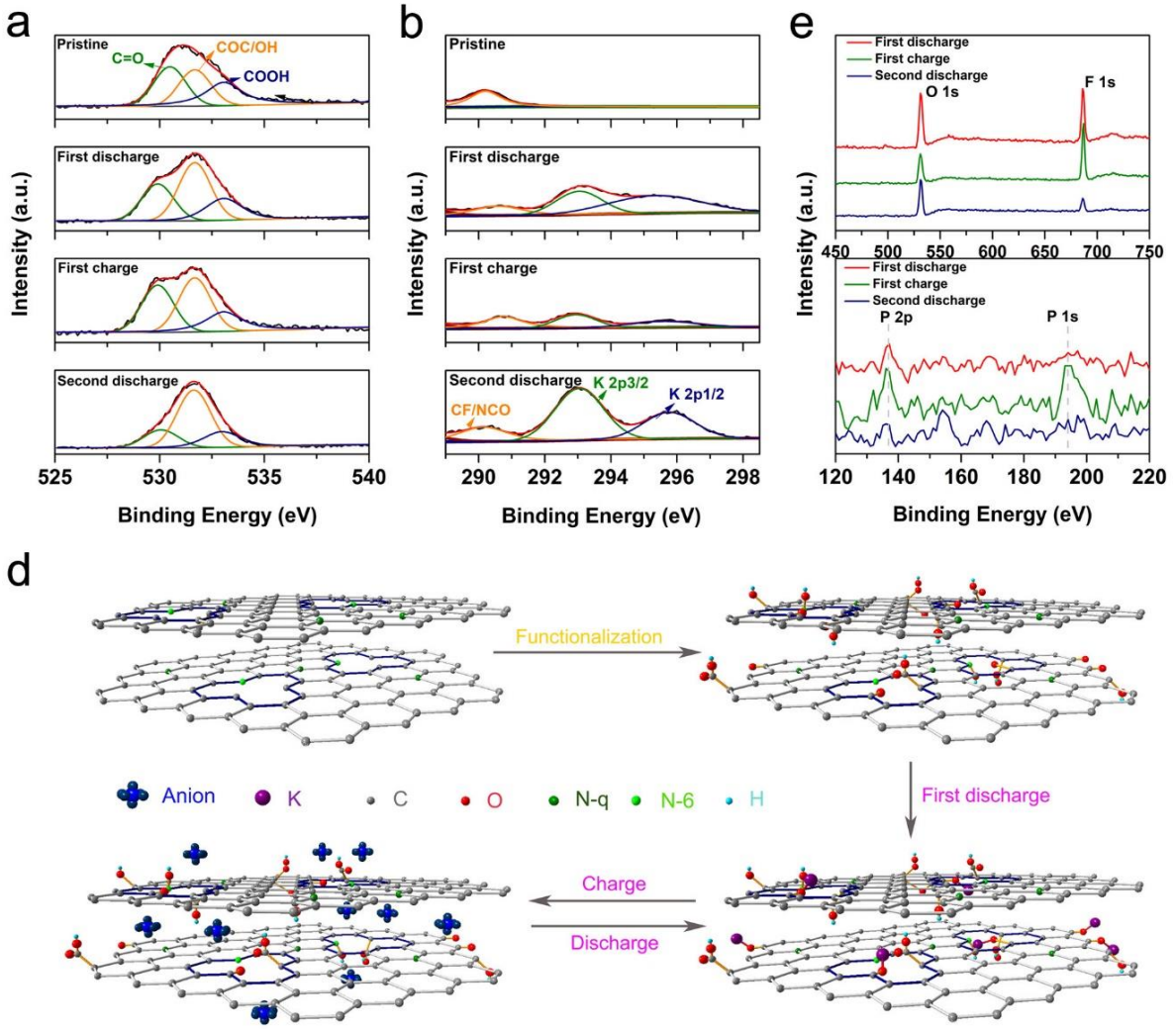

Figure 4-8 Electrochemical mechanism study with ex-situ XPS spectroscopes of ONC. (a) O 1s core level of XPS spectra at different charge and discharge states. (b) K 2p core level of XPS spectra screenshot from the figure of C 1s core level of XPS spectra. (c) F 1s core level of XPS spectra (upper), P 1s and P 2p core level of XPS spectra (lower). (d) Schematic illustration of charge and discharge processes of K-ions and anions in half cell.

According to the above analysis, the charge storage mechanism is illustrated in Figure 4-8d. The functionalization of the oxygen groups preferentially occurs at the defect sites of graphene layers induced by nitrogen doping. The functional groups of C=O are reduced to C-O upon the uptake of K-ions during the first discharge process. Thereafter, the reversible reduction/oxidization of C=O and the adsorption/desorption of PF_6^- take place during the subsequent cycles.

4.2.5 Analysis of the kinetics of potassium-ion storage

To further investigate the kinetics of the ONC electrodes, the CV curves at scan rates of 0.1 to 5.0 mV s^{-1} in Figure 4-9a were measured. The peak current obeys a power-law relationship with scan rate, which can be used to reveal the charge storage process according to the following equation:

$$i = av^b \qquad Eq.6$$

where *i*-value is peak current, *v*-value is scan rate, *a* and *b* are adjustable values. In principle, a *b*-value of 0.5 suggests domination of an ideal diffusion Faradaic reaction process, and a *b*-value of 1 suggests domination of an ideal surface faradaic reaction.[208] Figure 4-9b shows a good linear relationship based on the cathodic peak current, and the *b*-value is calculated to be 0.83, suggesting a surface-dominated process. The surface process contribution can be further quantitatively estimated according to the following equation:

$$Q = Q_\infty + const\ (v)^{-1/2} \qquad Eq.7$$

where *Q*-value is capacity, *v*-value is scan rate. Q_∞ is a constant value that is assigned to the ideal storage capacity at the infinity rate.[208, 209] In a plot of *Q* versus $v^{-1/2}$, the relationship between discharge capacity and scan rate can be established, and the linear regions represent capacity limited by semi-infinite linear diffusion-controlling whereas surface-controlled contributions are independent. As shown in Figure 4-9c, the ideal storage capacity by surface-controlling is estimated to be 0.087 mAh. The fast charge/discharge kinetics at high rates (> 1.0 mV s^{-1}) is dominated by a surface-controlled reaction. In addition, the level of the surface-control reaction contribution is also determined according to the relation of current density, *i*, with the combination of a capacitor-like index, k_1v, and a diffusion-controlled index, $k_2v^{1/2}$. At the scan rate of 1.0 mV s^{-1}, the surface-controlled contribution is 51.6% (Figure 4-9d). Similar to supercapacitors, the main factor for the high-rate charge/discharge is the transfer of ions and electrons to the surface of nanofibers rather than the conventional bulk diffusion. This is unsurprising since N–dopant in carbon precursor could induce more defects and edges of graphene layers, which results in more accessibility of bonding with oxygen-containing functional groups after a surface functionalization process.

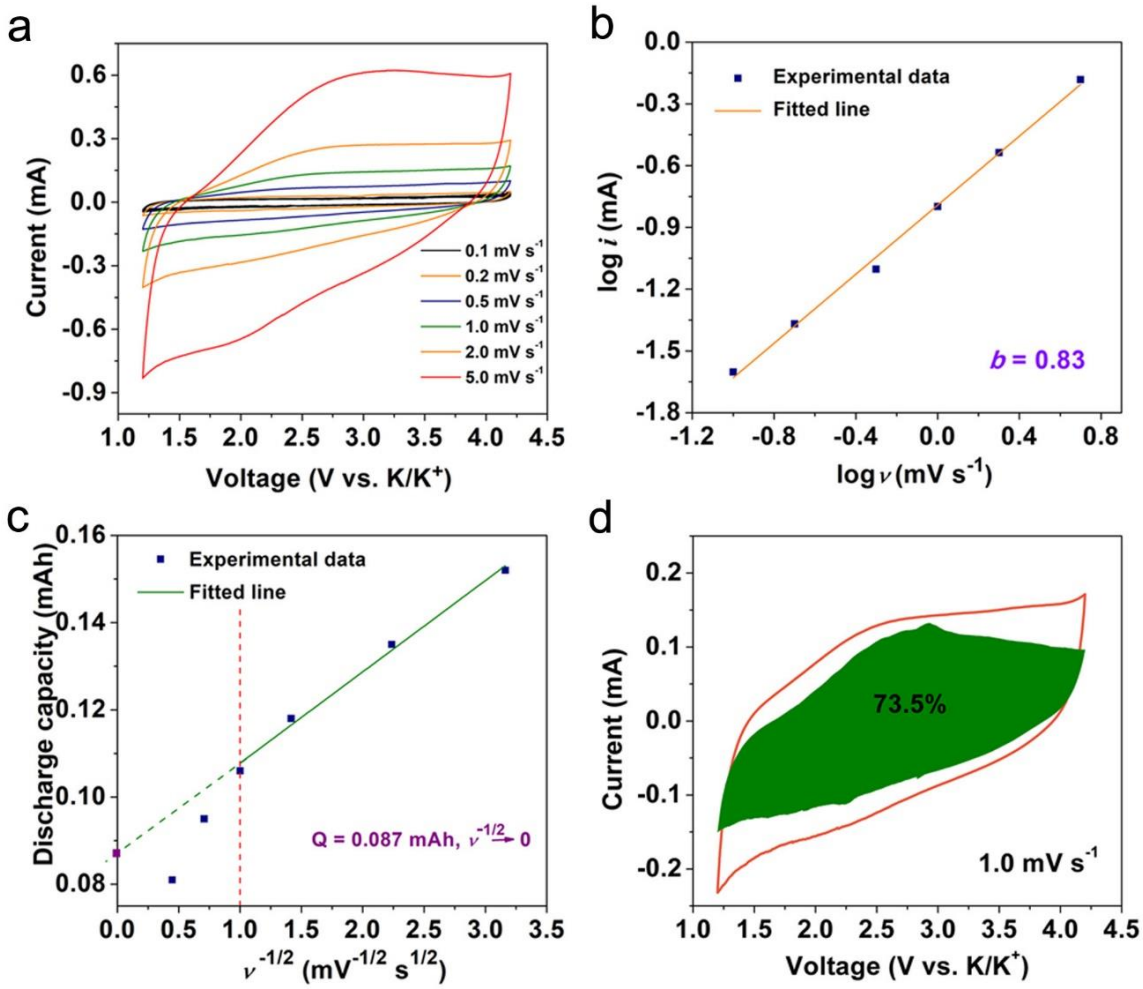

Figure 4-9 Quantitative analysis and illustration of K-storage process in ONC. (a) CV curves at various scan rates of 0.1 mV s^{-1} to 5.0 mV s^{-1}. (b) b value determination from anodic peaks currents. (c) Separation of diffusion-controlled capacity from capacitive-controlled capacity. (d) The contribution of surface reaction at 1.0 mV s^{-1}.

4.2.6 Discussion of optimal engineering of oxygen functionalization

The oxygen-containing groups and the stability of the surface reaction are two factors to achieve high capacity and cycling behavior. Those are relevant to the contents of oxygen-containing groups at the graphene edges and their graphitic environment (the aromatic rings). Therefore, increasing both graphene edges and the degree of graphitization that creates much stable redox-active sites are necessary. However, they are competing with each other. In principle, during the degree of graphitization increase, graphene edges will decrease for carbon materials. In this case, to understand the correlation and further explain the optimal performance of ONC, the control experiments are conducted, the comparisons of the cycling

performance in the carbon materials with the different functionalization conditions were carried out as well. All the carbon materials are tested by galvanostatic charge/discharge processes at 50 mA g^{-1} within the voltage window of 1.2–4.2 V. The ONC with different functionalized temperatures (40 ℃, 50℃, 60℃ and 70℃) and operation times (1h, 2h, and 3h) are investigated. As shown in Figure 4-10a and 4-10b, the ONC with the functionalized temperature of 50 ℃ and the operation time of 1h exhibits a higher storage capacity and more stable cyclability than the other samples obtained at various conditions. It can be speculated that the oxidation of concentrated H_2SO_4/HNO_3 destroys the graphitization of the carbon material while conducting the functionalization process, reducing the content of sp^2 hybridization. Functionalization under the conditions of a certain temperature and time ensures that the carbon material has a higher content of the oxygen functional groups while ensuring the redox reversibility of these functional groups.

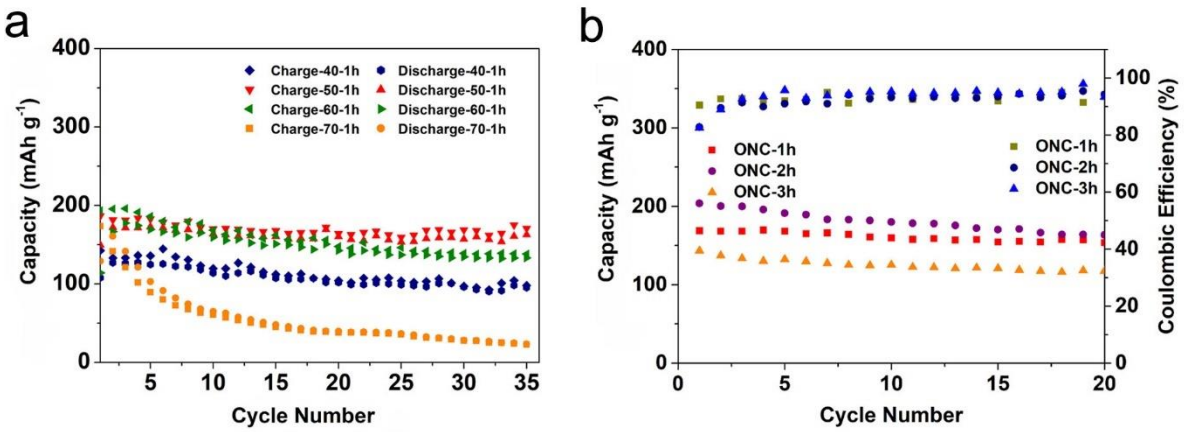

Figure 4-10 Electrochemical performances of the ONC electrodes with (a) different functionalized temperatures at 40 ℃, 50℃, 60℃ and 70℃), and (b) operation times for 1h, 2h, and 3h) in strong acids.

In addition, the different kinds of oxygen functionalized carbons using different carbon precursors are fabricated. As shown in Figure 4-11a–c, ONC with a higher degree of graphitization is more stable (capacity retention after 100 cycles: 69% for ONC1100; 63% for OCNT; 59% for NC800; 29% for OAC). Moreover, ONC possesses a better rate capability compared to other analogs. CNT is a graphitic carbon that possesses the highest degree of graphitization and lowest content of defects, it exhibits low capacity but excellent capacity retention. AC is a hard carbon that possesses a relatively low degree of graphitization and high content of defects, it exhibits high capacity but worse capacity retention. Overall, a soft carbon

with both lots of defects and a high degree of graphitization could be a better precursor for obtaining an oxygen functionalized carbon for ion adsorption. Moreover, the potassium-ion storage capabilities of the different NC materials of which possess different species of nitrogen defects are also different. The defects in the precursors of NC1100, NC950, and NC800 mainly are the N-6 and N-Q dopants which exist in carbon planes through sp^2 hybridizations, while those in NC650 mainly are the N-5 dopants which exist in carbon planes through sp^3 hybridizations. ONC cathodes possess approximate initial discharge capacities while initial charge capacity shows an obvious difference, ONC with higher sp^2 hybridization exhibits much better reversibility and cyclability. We speculate that the N-6 and N-Q dopants with the sp^2 hybridizations contribute extra electrons delocalization around nitrogen atoms, enhancing the aromaticity of carbon planes, especially at the carbon defects. The stronger aromaticity of carbon layers can enhance much delocalization of the electron in carbonyl groups, which might endow much higher stability of ONC at a higher temperature.

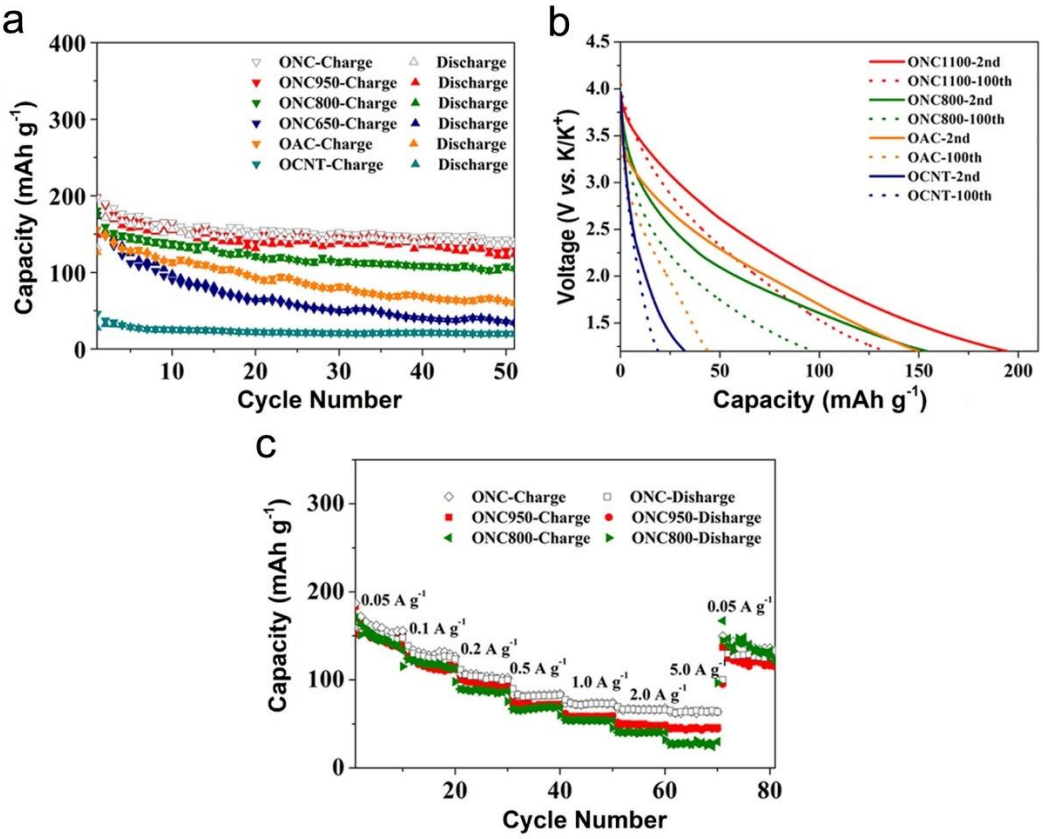

Figure 4-11 Electrochemical performances of oxygen functionalized carbons based on different carbon precursors. (a) Cycling performance at 50 mA g^{-1}. (b) Capacity retention after 100 cycles. (c) Rate performance of ONC analogues.

4.2.7 Full-carbon potassium-ion hybrid capacitor

To demonstrate the potential application of the proposed ONC cathode, a full dual-carbon PIC is configurated by using ONC as the cathode and NC as the anode. The rationale behind it is based on the high working voltage of ONC and the low working voltage of NC reported in our previous work (Figure 4-12).[194] Prior to the full-cell assembly, NC was activated by cycling in a half cell at 50 mA g^{-1} for 10 cycles.

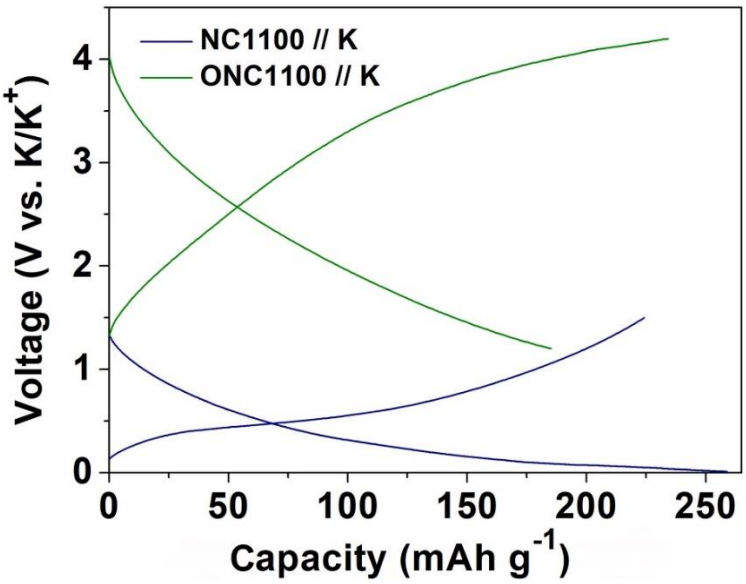

Figure 4-12 Illustration of charge and discharge profiles of cathode ONC and anode NC in half cells.

As shown in Figure 4-13a, K^+ cations and PF_6^- anions can be reversibly stored in ONC during charge and discharge processes, whereas NC only reversibly stores potassium ions. The first charge and second discharge profiles are shown in Figure 4-13b. The full cell displays a sloping profile in the voltage window of 0.5–3 V at a current density of 0.1 A g^{-1}, which is related to the similar feature of the ONC half cell. Figure 4-13c shows that the full cell delivers a charge capacity of 163 and a discharge capacity of 100 mAh g^{-1}, giving an initial CE of 62%. The CE then rapidly increases to 94% after 10 cycles. After 50 cycles, the full cell maintains a reversible capacity of 84 mAh g^{-1}. The rate performance of the full cell is shown in Figure 4-14d, where the discharge capacities of 73, 58, and 43 mAh g^{-1} were obtained at the current densities of 0.2 A g^{-1}, 0.5 A g^{-1}, and 1.0 A g^{-1}, respectively.

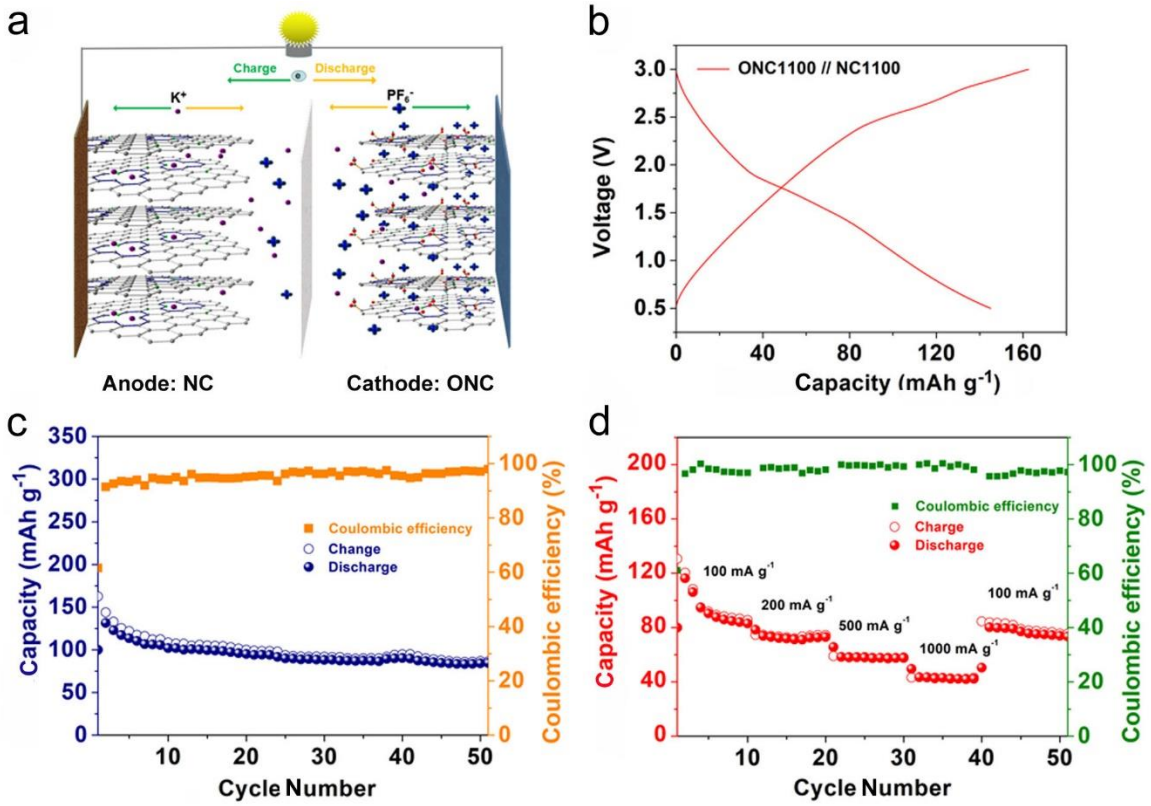

Figure 4-13 Electrochemical performances of the ONC//NC full cell. (a) Schematic illustration of the charge and discharge processes in full cell. (b) The first charge and second discharge profiles. (c) Cycling performance at the current density 100 mA g^{-1}. (d) Rate performance with various rates ranging from 100 mA g^{-1} to 1000 mA g^{-1}.

Remarkably, the novel ONC//NC PIC exhibits a high energy density of 135 Wh kg^{-1} and a high power density of 1500 W kg^{-1}. As shown in Figure 4-14, this performance is highly competitive among previously reported PIC works.[86, 88, 151, 152, 176, 210-212]

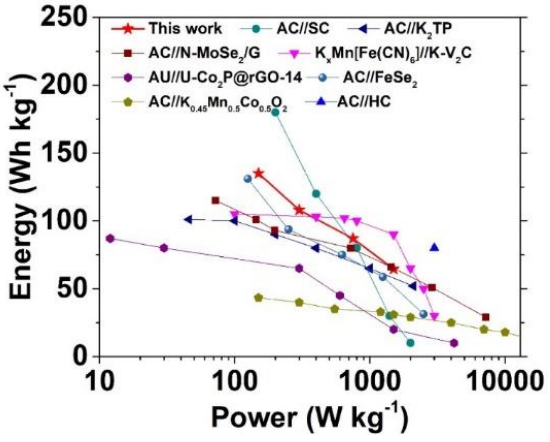

Figure 4-14 Ragone plot comparison of the ONC//NC cell with other PICs.

4.3 Conclusion

Benefiting from the surface-controlled reaction, the oxygen functionalized carbon nanofibers cathode exhibits a large capacity and great rate capability within a high voltage window for potassium-ion storage. The charge storage mechanism and rational material design highlight an important key element of storing large-sized ions. Surface faradic reaction dominated process instead of diffusion faradic reaction dominated process leads to the optimal performance of the promising PICs. We also find out a clue that a soft carbon precursor with suitable graphitization and defects would be a better choice for obtaining stable and oxygen-rich carbon in strong acids. Based on the oxygen functionalization enabled charge storage with a high voltage window, this work demonstrates an advanced potassium-ion-based full cell consisting of carbonaceous cathode and anode deriving from a single carbon source. It may shed light on designing high-performance PIC cathodes and open up an avenue towards future energy storage technologies with low cost and material sustainability.

5 Electrolyte effect on the oxygen functionalized carbon cathode of PICs

Identifying an effective electrolyte for enhancing the diffusion of both cation and anion is significantly necessary. Here, it is the first time to demonstrate that the electrochemical behavior of graphite oxide in ether electrolytes outperforms those in ester electrolytes for the cathode of PIC. The anion and cation are isolated effectively in dimethyl ether, which facilitates the hybrid-ion diffusion thus enhancing the electrochemical performance. This result provides a rational strategy to realize high-rate cations and anions storage on the carbon cathode. Furthermore, a capacitor prototype, graphite oxide cathode versus pristine graphite in ether electrolyte (GO‖DME‖PG), is proposed, which exhibits a large energy density at a high power density. Considering that all the components of the high-performance capacitor can be produced industrially, this work is a solid step to promote the commercialization of secondary ion capacitors.

5.1 Experimental section

5.1.1 Synthesis of graphite oxide

The graphite oxide (GO) nanosheets were prepared by modified Hummer's method.[213] Briefly, the graphite (1 g) and concentrated H_2SO_4 (23 mL, 95 wt% in water) were mixed and stirred in an ice bath. After the graphite powders were completely dispersed, add $NaNO_3$ (0.5 g) to the mixture and stir for 30 min. Next, $KMnO_4$ (3 g) was added to the mixture and stirred for another 1 h. The color of the mixture becomes dark green. After that, transfer the mixture to an oil bath and keep it at 32–35 ℃ for 30 mins while stirring. After the color of the mixture becomes brown, add distilled water (46 mL) slowly into the mixture within 15 mins, well controlling the temperature in the range of 95–98 ℃. Afterward, add additional warm distilled water (150 mL) to the mixture, followed by adding H_2O_2 (10 ml, 30 wt% in H_2O). Finally, the golden mixture was formed. The warm mixture was filtered and washed with distilled water until the supernatant was pH neutral. The dark brown slurry was transferred into a flask (50 mL) and annealed in a furnace with ambient air at 250 ℃ for 6 h.

5.1.2 Materials characterization

The microstructures and morphology of Go were observed using scanning electron microscopy, Hitachi 434 S4800 SEM and transmission electron microscopy, JEOL JEM-435 2100F TEM. The XRD pattern was characterized by an 18 KW D/MAX2500V PC diffractometer at a scan rate of 0.2° min^{-1}. The FTIR spectra were collected through Nicolet 6700 FT-IR spectrometer (Thermo), the 1 M electrolyte samples were tested with the assist of an attachment for liquid sample testing. Raman spectra were collected on a LabRAM HR Evolution Raman spectrometer with the incident laser light of 532 nm wavelength. Another attachment for liquid sample testing also was employed for the Raman spectra measurements of the 1M electrolytes. ^{19}F nuclear magnetic resonance (NMR) spectra of the electrolytes were collected by Bruker AV-III 600 MHz, using a co-axial internal insert filled with 0.05 M $LiPF_6$ in the deteriorated water (D_2O) as the reference.

5.1.3 Electrochemical measurements

The GO electrode was fabricated by mixing the GO nanosheets (90 wt%) and carboxymethyl cellulose (CMC, 10 wt%) in distilled water. After fully grinding, the slurry was coated on the Al foil and then dried in a vacuum oven at 110 ℃ for 24 h. The electrode film was punched

into circular pieces, the active mass on each piece was controlled to about 1.5 mg. The coin-cell was assembled in an N_2-filled glove box. The electrolytes including 1M KPF_6 in dimethyl glycol (DME), 1M KPF_6 in ethylene carbonate and diethyl carbonate (*vol.*, EC:DEC = 1:1), 1M KPF_6 in ethylene carbonate and propylene carbonate (*vol.*, EC:PC = 1:1) were also prepared in an N_2-filled glove box. The glass microfiber filter (Whatman, Grade GF/B) was used as the separator. The cyclic voltammetry (CV), galvanostatic intermittent titration technique (GITT), and electrochemical impedance spectroscopy (EIS) tests were performed on a VSP electrochemical workstation (Bio-Logic, France). Galvanostatic charging/discharging tests were performed on a Land CT 2001A 449 battery testing system (Land, China). For the full cell, the pristine graphite electrode was composed of commercial graphite powders (90 wt%) and CMC (10 wt%). The anodes were pre-potassiated by cycling in half cells.

5.2 Results and discussions

5.2.1 Structure and morphology of graphite oxide electrode

The high-magnification SEM image in Figure 5-1a shows the typical morphology of 2D GO nanosheets. The HRTEM image in Figure 5-1b shows the graphite powders are completely exfoliated to multiply graphene layers. The exfoliation process generates lots of mesopores and micropores on the graphene layers, indicating that there are many carbon defects on the surface of the GO nanosheets.[214] Moreover, GO nanosheets possess a high content of oxygen-containing functional groups. The element mapping further displays a homogeneous distribution of C and O elements in the GO nanosheets (Figure 5-1c–e). The GO nanosheets are verified that contain abundant defects and oxygen-containing functional groups. These defects and oxygen-containing functional groups are the effective hosts for the absorption of K^+ and PF_6^-.

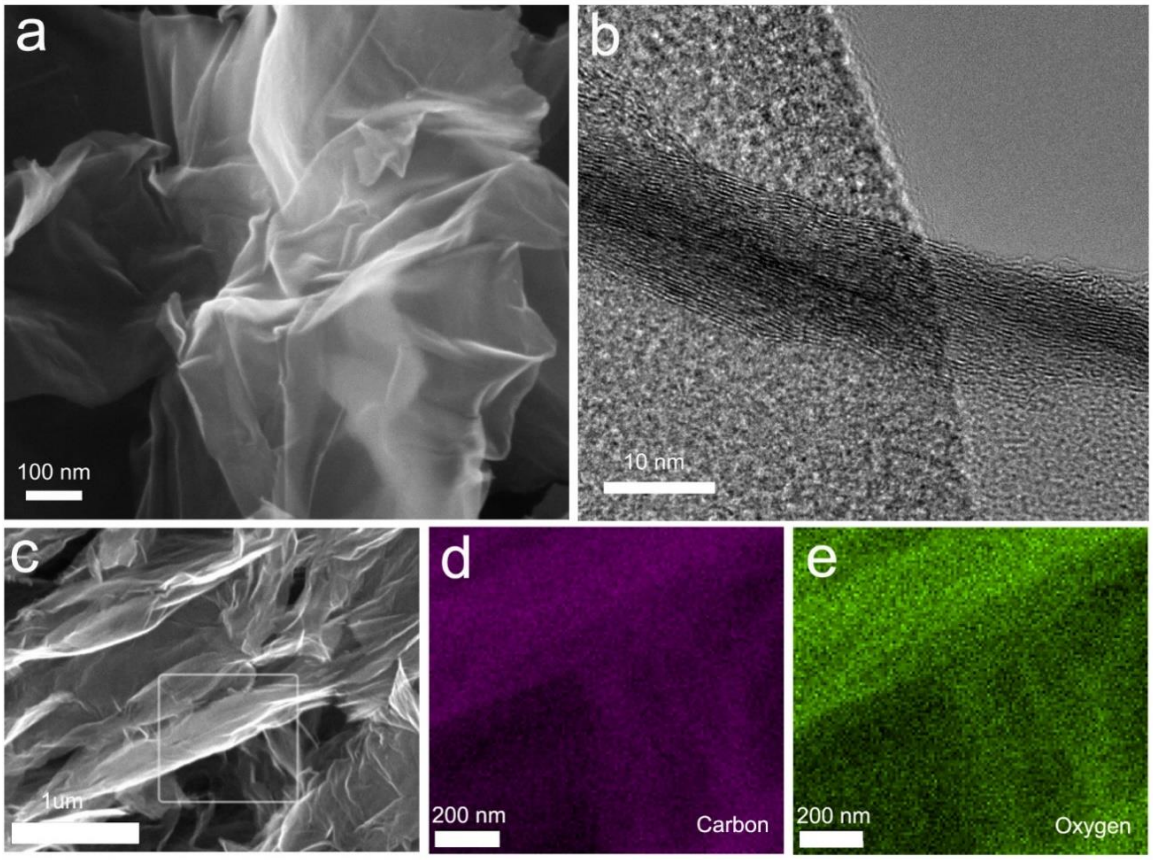

Figure 5-1 Structure characterization GO by electron microscopes. (a) SEM image. (b) HRTEM image. (c-e) Image of element mapping of C and O.

The carbon layer structure is further investigated by characterizations of XRD and Raman spectroscopy. As shown in Figure 5-2a, there are two broad peaks located at about 24° and 43° for the XRD pattern of GO nanosheets, corresponding to the (002) and (101) planes of the GO lattice structure. The relatively strong (002) peak shows a preferred orientation of the carbon lattice structure, suggesting a layered structure of the GO nanosheets. The Raman spectrum in Figure 5-2b displays that there are two peaks located at 1348 cm^{-1} and 1595 cm^{-1}, corresponding to the standard carbon D and G bands, respectively.[215] It further suggests that GO nanosheets possess ordered and disordered carbon layer structures, which is consistent with the result of TEM measurement.

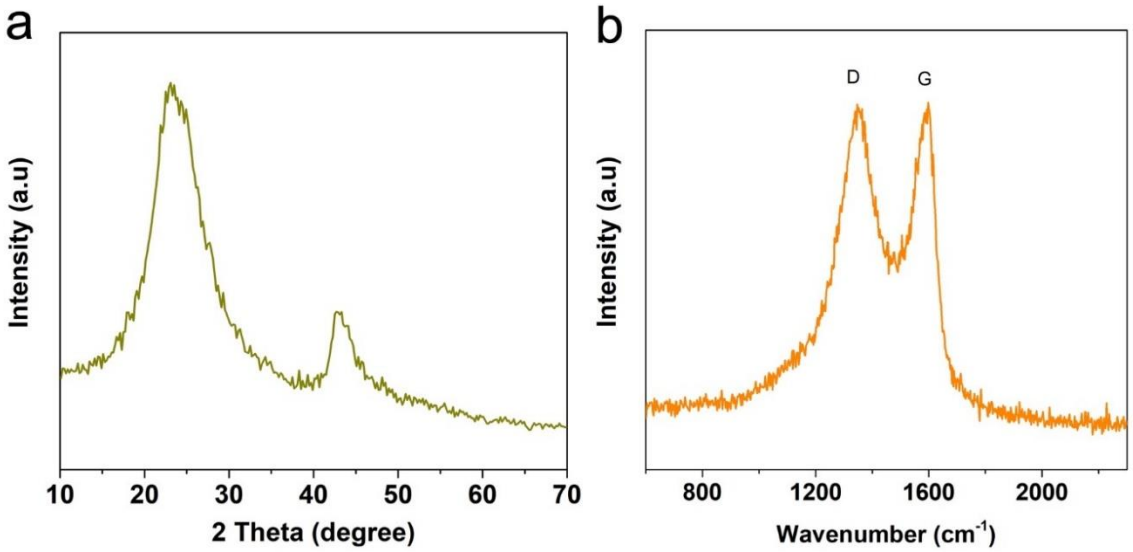

Figure 5-2 XRD pattern (a) and Raman spectrum (b) of GO nanosheets.

5.2.2 Electrochemical performances of GO nanosheets in different electrolytes

To investigate the electrochemical behaviors of as-prepared GO nanosheets in different electrolytes, we assemble a series of potassium metal capacitors using GO as the cathode against potassium metal as the anode respectively in DME, EC^DEC, and EC^PC electrolytes (labeled as GO-DME, GO-EC^DEC, and GO-EC^PC). The different configurations are tested within a voltage window of 1.5–4.5 V. The cyclic voltammetry (CV) curves at a scan rate of 0.2 mV s^{-1} for the initial 10 cycles are shown in Figure 5-3. The shape of the GO-DME (Figure 5-3a) looks much like a parallelogram than those of GO-EC^DEC (Figure 5-3b) and GO-EC^PC (Figure 5-3c), indicating a typical pseudocapacitive behavior for the GO-DME configuration.[193] Furthermore, GO-DME possesses quick access for the infiltration of

electrolytes, benefitting that it reaches the full-discharge state with only two cycles, while the other two configurations need multiple cycles.

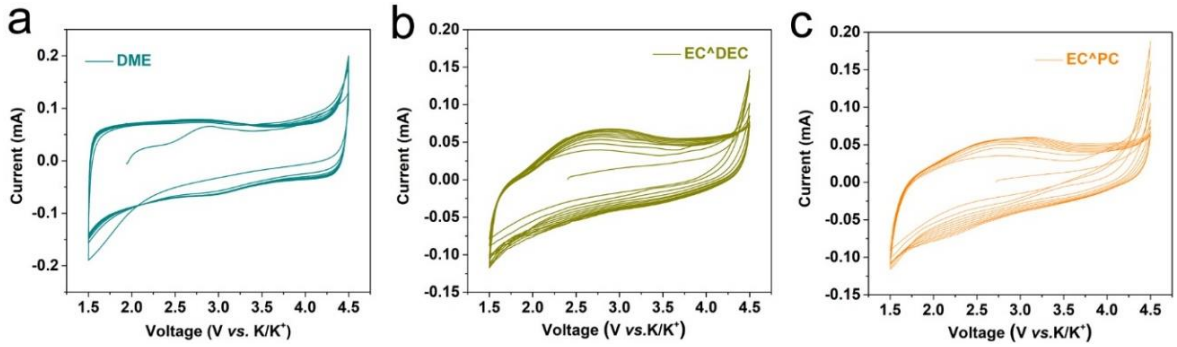

Figure 5-3 CV curves of the (a) GO-DME, (b) GO-EC^DEC, and (c) GO-EC^PC configurations at scan rate of 0.2 mV s^{-1}.

Figure 5-4a and 5-4b show the cycling stability and rate capability at various current densities, where the GO-DME exhibits the highest performance. It delivers capacities of 120, 111, 106, 97, and 83 mAh g^{-1} at 0.5, 1, 2, 5, and 10 A g^{-1}. Moreover, it maintains excellent cyclability during the next 900 cycles. However, GO-EC^DEC and GO-EC^PC respectively deliver lower capacities of 75 (62), 66 (52), 59 (35), 44 (11), and 31 (8) at the same rates. The initial charge and discharge capacities are shown in Figure 5-4c, GO-DME only needs a few cycles to reach full charge and discharge, while GO-EC^DEC and GO-EC^PC need more than 20 cycles. The charge and discharge profiles at various rates are shown in Figure 5-4d–f, the sloping plots are consistent with CV curves. It is worth noting that the polarization of GO-DME is much weaker than those of GO-EC^DEC and GO-EC@PC. This phenomenon is attributed to the stable and fast kinetics of ion storage in the DME electrolyte.

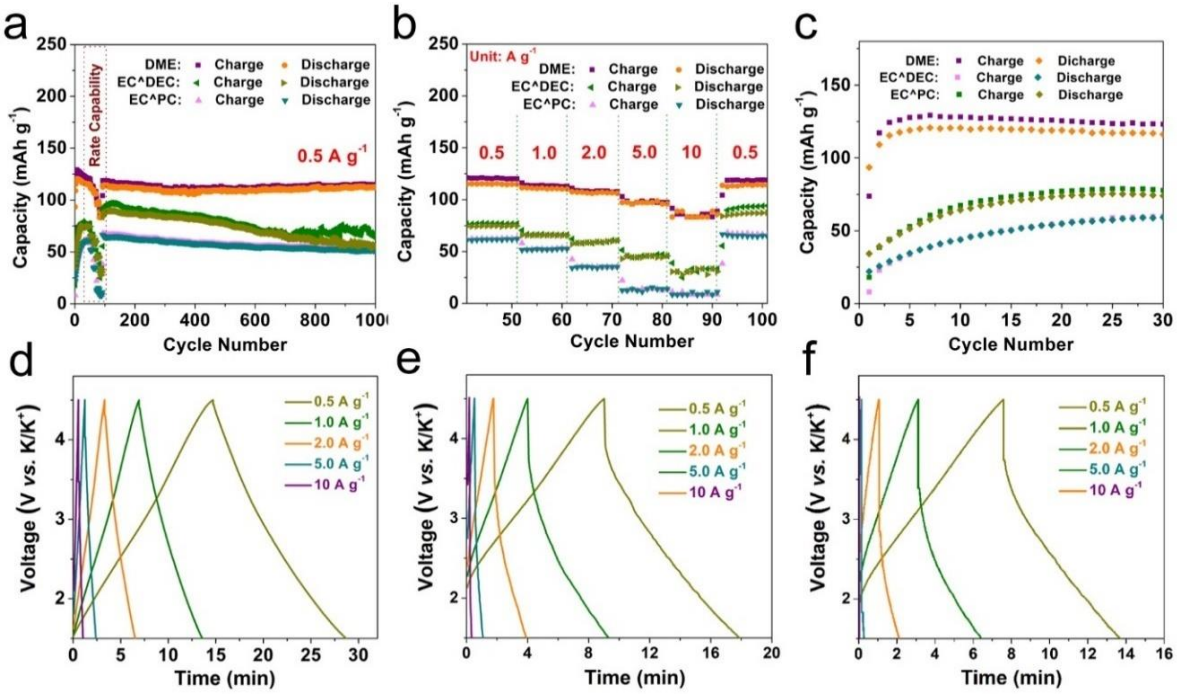

Figure 5-4 Electrochemical performance of GO in half-cell configurations. (a) cycling performance, (b) rate performance, and (c) initial charge and discharge behaviors of GO-DME, GO-EC^DEC, and GO-EC^PC at various current densities. Charge and discharge profiles of (d) GO-DME, (e) GO-EC^DEC, and (f) GO-EC^PC.

To further verify the electrolyte effect on the electrochemical performance, we employ a standard commercial active carbon (AC) material as the cathode and investigate its electrochemical performance in the different electrolytes. As shown in Figure 5-5a, the AC cathode in DME exhibits the highest rate capability. The relatively low specific capacity in all three electrolytes could ascribe to the low content of oxygen functional groups. The charge and discharge profiles at a high current density of 2.0 A g^{-1} in Figure 5-5b also show that the polarization in DME electrolyte is weaker than that in EC^DEC and GO-EC^PC electrolytes. Overall, the AC cathode in DME exhibits the best electrochemical properties, which is similar to the behavior of the GO cathode in DME.

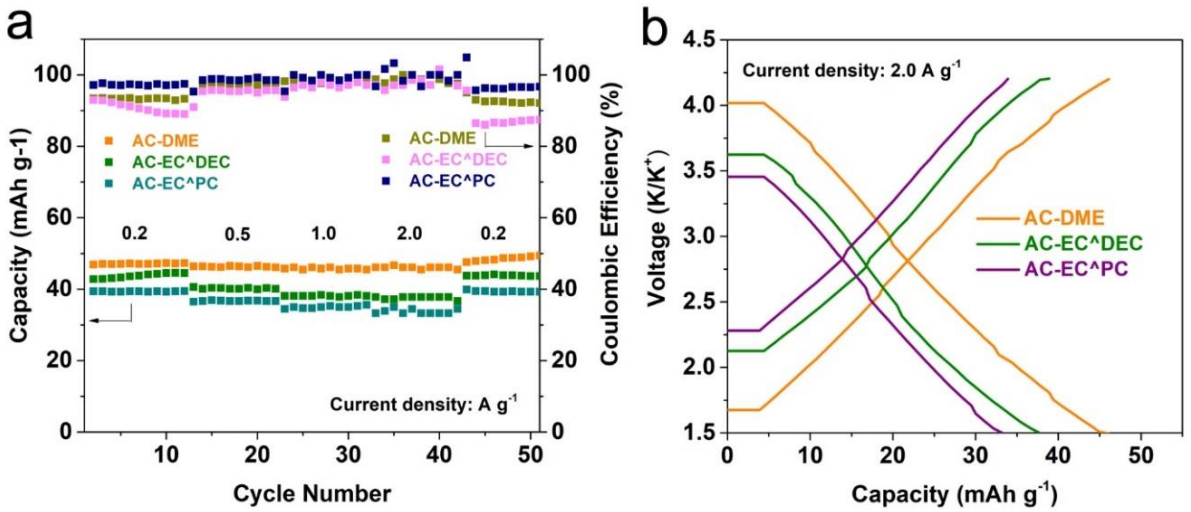

Figure 5-5 Electrochemical performances of the active carbon. (a) Rate capability at various current densities. (b) Charging and discharging profiles at 2 A g^{-1}.

To further demonstrate the fast charge and discharge property of GO-DME configuration, the GO-DME is charged and discharged at 2.0 A g^{-1}. As shown in Figure 5-6a, the specific capacity can maintain a high specific capacity of 99 mAh g^{-1} over 2500 cycles without obvious capacity decay. Moreover, the GO-DME is also tested under the condition of charging at a high current density of 2.0 A g^{-1} and discharging at a low current density of 0.5 A g^{-1}. As shown in Figure 5-6b, it exhibits a specific capacity of 98 mA g^{-1} over 500 cycles without observable decay. The charging process only takes 184 s, but it can maintain a high-capacity output for 987 s (Figure 5-6c), which shows a great potential of super-fast charging capability for GO-DME. In addition, the energy densities and power densities in the half cells are displayed in Figure 5-6d. Encouragingly, GO-DME possesses the capability to output almost twice the energy densities of GO-EC^DEC and GO-EC^PC at the same power density (calculation based on GO mass), which provides a basis for estimating its high energy density and power density in the full PICs. The fast charge and discharge performance without much degradation mainly benefit from the fast kinetics of hybrid-ion storage reactions that occur on or near the surface of GO nanosheets.

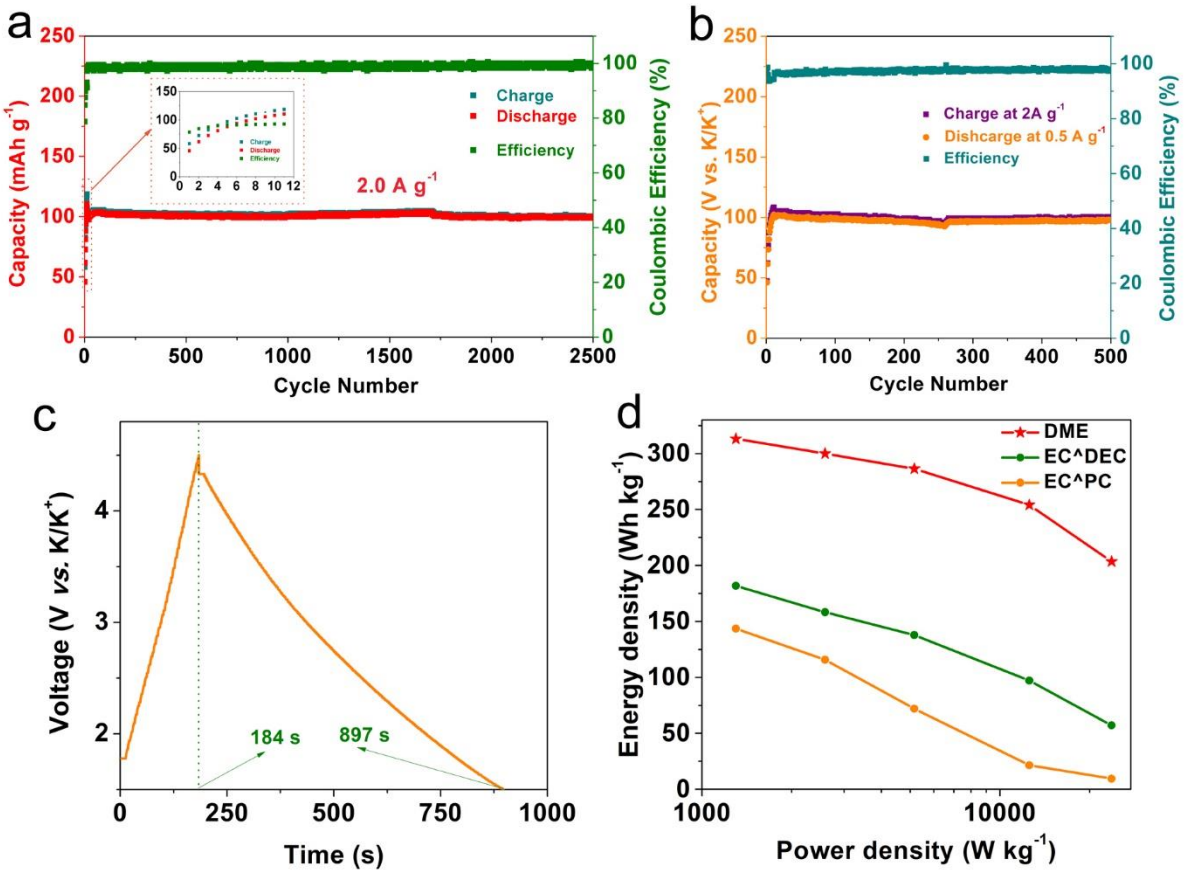

Figure 5-6 Electrochemical performance of GO nano sheets. (a) Cycling performance at high current density of 2.0 A g^{-1}, inset: initial cycling behavior. (b) Cycling performance under a charging current density of 2.0 A g^{-1} and discharging current density of 0.5 A g^{-1}. (c) Voltage-time profiles corresponding to fast charge-slow discharge mode. (d) Ragone plots of the half cells in the different electrolytes.

5.2.3 Ion storage kinetics analysis for GO nanosheets in different electrolytes

To investigate the kinetics of the electrodes, a series of CV measurements are conducted at scan rates from 0.5 to 10 mV s^{-1}. As shown in Figure 5-7a–c, in contrast to GO-EC^DEC and GO-EC^PC, the broad cathodic and anodic curves are maintained at high scan rates for GO-DME. In the cases of GO-EC^DEC and GO-EC^PC, their curves become steeper and show large polarization. To determine the different levels of their capacitive contributions, further quantitative analysis is performed according to the relationship between the current response, *i*, and scan rates, *v*, based on the following equation:

$$i = k_1 v + k_2 v^{1/2} \qquad Eq.8$$

where k_1v indicates the response of surface-controlled behavior, $k_2v^{1/2}$ indicates the diffusion-controlled behavior.[216, 217] By determining the k_1 constant, the surface-controlled contributions of the electrodes are clarified. As shown in Figure 5-7d, the comparably large contributions are obtained for all GO-DEM, GO-EC^DEC, and GO-ECPC. Thereby, a surface-dominated behavior is identified as the major charge storage mechanism for GO electrodes. Moreover, GO-DEM possesses the largest contribution compared with GO-EC^DEC and GO-EC^PC at each scan rate, suggesting the fastest kinetics dominated by the charge storage of GO-DME. Figure 5-7e and 5-7f show the fractions of the currents from capacitive domination and diffusion domination. The capacitive contribution enlarges from 83% to 92% with increasing scan rates, which complies with the general characteristic of electrochemical reaction kinetics for electrode materials. Therefore, the fastest kinetics for GO-DME is confirmed, which is consistent with its highest rate capability.

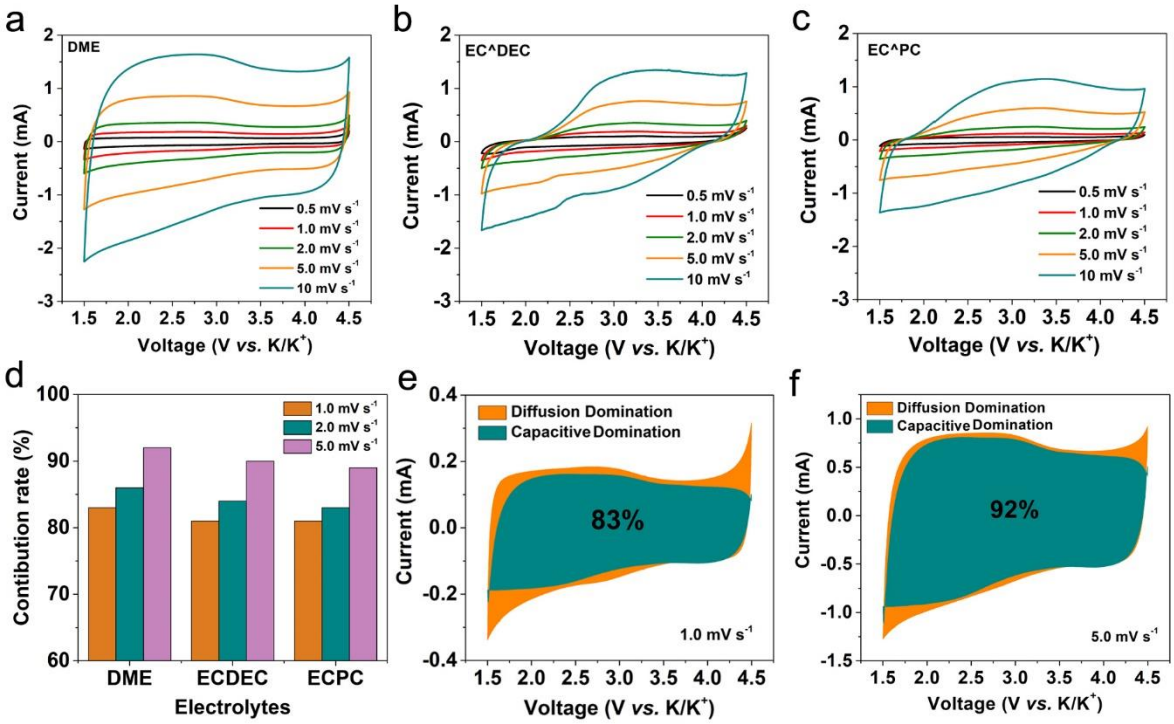

Figure 5-7 Quantitative analysis and illustration of the ion-storage process in GO nanosheets. CV curves at various scan rates of 0.5 mV s^{-1} to 10 mV s^{-1} of (a) GO-DEM, (b) GO-EC^DEC, and (c) GO-EC^PC. (d) Capacitive contribution in three electrolytes at different scan rates. Separation of capacitive domination from diffusion domination at (e) 1 mV s^{-1} and (f) 5 mV s^{-1}.

To further verify the position of the active sites, we carried out ex-situ Raman spectroscopy measurements to investigate the full-charged, full-discharged, and pristine states for the GO-DME. The ex-Raman spectra in Figure 5-8 show that there is almost no difference among the ratios of I_G/I_D at the different states, which suggests the limited variation of the carbon layer structure during the charging and discharging processes. It further demonstrates the position of the reaction active site is at or near the electrode interface.

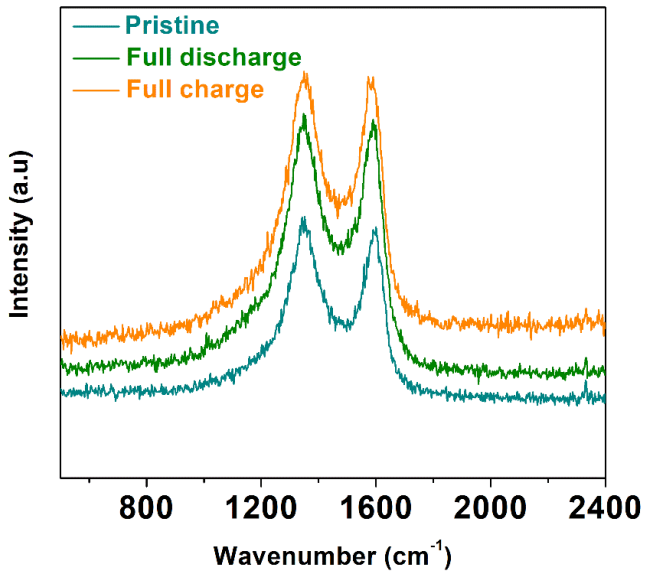

Figure 5-8 Ex-situ Raman spectra for the different ion-storage states of GO-DME.

The enhanced electrochemical performance of GO-DME indicates fast ion diffusion and electron transportation in the DME electrolyte. To further understand the fast charge and electron transfers, we conduct characterizations of galvanostatic intermittent titration technique (GITT) and electrochemical impedance spectroscopy (EIS). Figure 5-9a shows the potential responses of GO in the different electrolytes during the GITT measurements. The GO-DME displays the smallest overpotential for all relaxation periods, implying its better ion-diffusion kinetic. Based on the GITT data, the ion diffusion coefficient (D_{ion}) during discharge can be estimated according to the equation:[218]

$$D_K = \frac{4}{\pi\tau}\left(\frac{m_B V_M}{M_B S}\right)^2\left(\frac{\Delta E_S}{\Delta E_\tau}\right)^2 \qquad \left(t \ll \frac{L_2}{D}\right) \qquad Eq.9$$

where m_B, V_M, and M_B are the mass, molecular volume, and molar mass of the active materials, respectively; τ is the pulse time (s); S is the area of the electrode; $\triangle E_S$ and $\triangle E_\tau$ are determined

according to the description in Supplementary I. As shown in Figure 4-9b, GO-DME exhibits the highest values of D_{ion} among the function of most voltages, and the difference becomes more obvious in the lower ranges. As we know, the anion storage mainly occurs in a relatively higher voltage range while cation storage mainly occurs at a relatively lower voltage range for the carbon cathode in LICs, SICs, and PICs. Regarding this basis, we speculate that ion storage of potassium ions at the lower range is much faster for GO-DME. Figure 5-9c–e shows the electrochemical impedance spectroscopy (EIS) measurements for GO-DME, GO-EC^DEC, and GO-EC^PC after the 1st, 10th, and 50th cycles, respectively. The semicircles represent the interface resistances. They become smaller during the acceleration of cycle number, meaning the interface resistances for all samples decrease after cycling, which is attributed to the opening of the ion-diffusion pathway at GO interface layers. The results are consistent with the initial electrochemical performances for GO-DME, GO-EC^DEC, and GO-EC^PC. More importantly, in the case of GO-DME, the interface resistances corresponding to each cycle are exponentially lower than those of GO-EC^DEC and GO-EC^PC, indicating the lowest ion-diffusion barrier in DME electrolyte. It also agrees well with their difference in electrochemical behaviors.

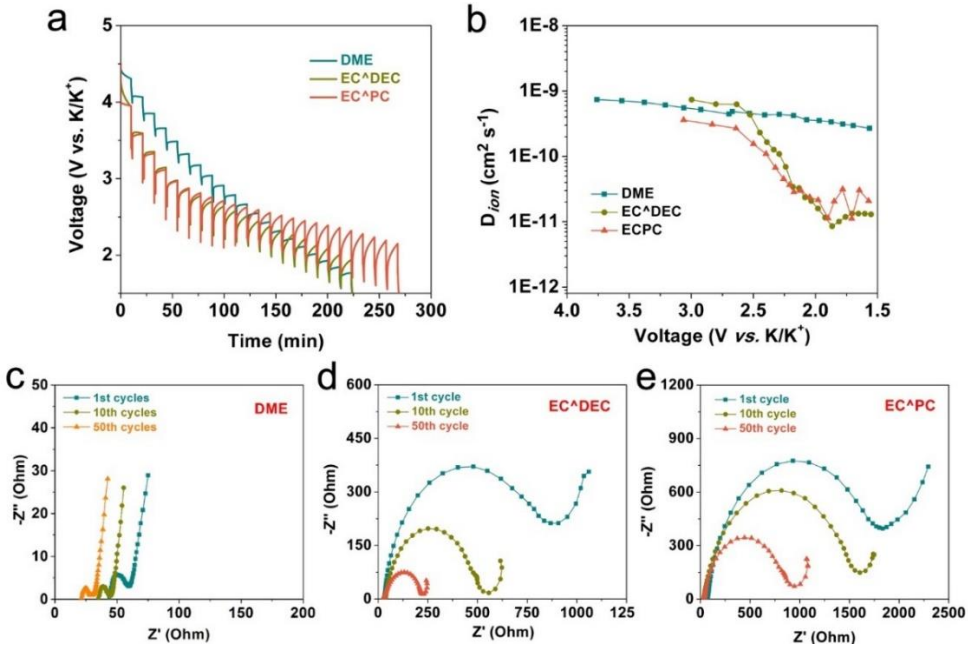

Figure 5-9 Electrochemical diffusion kinetics and impedance analysis for GO-DME, GO-EC^DEC, and GO-EC^PC. (a) GITT profiles of the discharging process. (b) Ion-diffusion coefficient as a function of the state of discharging process. Nyquist plots of (c) GO-DME, (d) GO-EC^DEC, and (e) GO-EC^PC.

5.2.4 Electrolyte properties and their roles in ion diffusion kinetics

Considering the obvious difference in the electrochemical behavior between the ether-based and ester-based electrolytes, we believe that there is an intrinsic reason that can interpret this phenomenon. As we know, many works have demonstrated that oxygen-functionalized carbons can reversibly store anions and cations within a high voltage window for hybrid-ion capacitors. Recently, it is also verified in the PICs. As illustrated in Figure 5-10a, unlike potassium ion batteries and dual-ion batteries, the graphite oxide with abundant oxygen-containing functional groups and defects can store both cations and anions at different active sites. Therefore, the interaction between the cation and anion plays a crucial role in the ionic transfer at the electrode interface, especially for the HICs. To further demonstrate this idea, we mainly focus on investigating the solvation environment of anions and cations in different electrolytes using FTIR spectroscopy, Raman spectroscopy, and NMR spectroscopy measurements. As shown in Figure 5-10b and 5-10c, the infrared spectra of the different electrolytes suggest that there are two different types of anion states that exist in the electrolytes, one is free $PF6^-$ which is assigned at the wavenumber of 839 cm^{-1}, another one is the K^+PF6^- contact ion pair which is assigned at the wavenumber of 857 cm^{-1} and 876 cm^{-1}.[219] It is found that the K^+ and $PF6^-$ in the EC^DEC (10.4%) and EC^PC (11.8%) are easy to form the K^+PF6^- contact ion pairs than that in DME (6.8%), as evaluated by the partition of ions pairs/free ions ratio. This result demonstrates that the anions and cations in DME are easy to be separated.[220] Figure 5-10d shows the Raman spectra of the different electrolytes. It is observed that there are similar peaks at about 740 cm^{-1} in the series of Raman spectra.[219] They are the P-F Raman vibrations in PF_6^- anions that provide information on the distance between $PF6^-$ and K^+, indicating the solvation structure of the electrolytes. Inset displays a blue shift at P-F peak position (Comparing DME-based electrolytes with EC^DEC- and EC^PC-based electrolytes), suggesting that the $PF6^-$ anions are positioned farther from K^+ cations in DME-based electrolyte. Moreover, it demonstrates that the $K^+[DME]_x$ clusters are much denser than the $K^+[EC]_x[DEC]_x$ and $K^+[EC]_x[DEC]_x$ clusters, resulting in the weaker interaction that K^+ makes contact with PF_6^- in DME-based electrolyte.[220] The ^{19}F-NMR peaks of the PF_6^- in DME-based electrolyte shift towards a lower magnetic field (Figure 5-10e), which further confirms the denser $K^+[DME]_x$ clusters.[221]

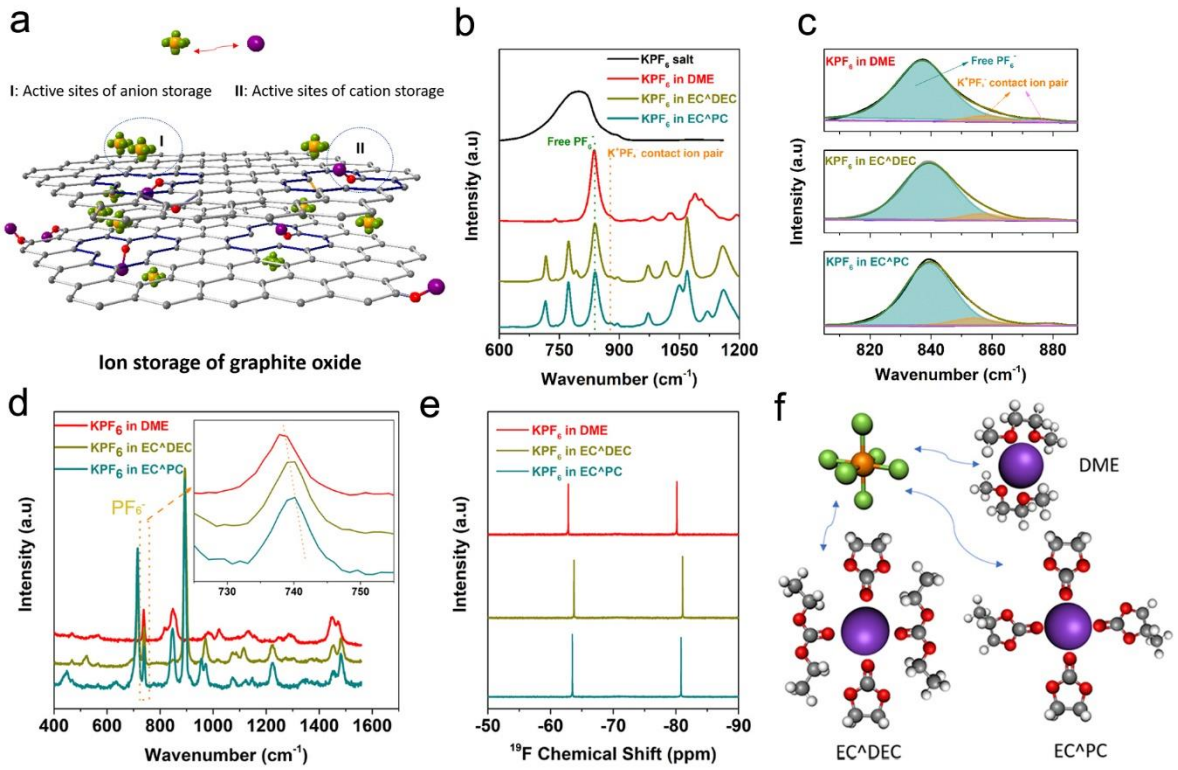

Figure 5-10 The characterization of the solvation structures in different electrolytes. (a) Illustration of the anion and cation storage on graphite oxide for PHICs. (b) FTIR spectroscopy of KPF_6 and 1.0 M KPF_6 dissolved in different solvents. (c) Relative content of free $PF6^-$ and K^+-$PF6^-$ contact ion pairs in different electrolytes. (d) Raman spectra of the different electrolytes; inset: the peak of K^+-$PF6^-$ contact ion pairs. (e) ^{19}F-NMR spectra of the anion $PF6^-$ in the different electrolytes. (f) Proposed coordination structure of solvating K^+ in the different solvents.

On that basis, it is assumed that each K^+ can coordinate with four oxygen-containing groups, thereby we can propose the universal coordination structures of the solvating K^+ in the different electrolytes. Note that this is an average coordination structure.[220] As shown in Figure 5-10f, we define that each K^+ coordinates with two DME molecules, while each K^+ coordinates with four ester molecules. The EC-, PC-, and DEC-based solvation structures are loose because of the branched structure of the carbonyl groups and carbon rings. The bidentate chelation of $K^+[DME]_2$ exhibits much condensed, therefore the $PF6^-$ is not easy to contact with the K^+ to form the K^+PF6^- contact ion pair. The DME solvent can separate the $PF6^-$ and K^+ effectively, giving the adequate freedom of movement of the PF_6^- anions and K^+ cations. These viewpoints are verified by the above analysis of the FTIR, Raman, and NMR spectra. In this

way, the $PF6^-$ anions possess different opportunities to contact with K^+ cations in the different solvents, which is accordant with their ion diffusion efficiencies. Thus, the more isolated cations and anions in electrolytes lead to much fast of ion diffusion. It further suggests that the solvent structure plays a crucial role in determining the fast kinetics of the anions and cations storage in the DME-based electrolyte. As shown in Figure 5-11, the solvated ions in ester electrolytes are more crowded than that in ether electrolytes, meaning the ion diffusion resistances in ester electrolytes are greater than that in ether electrolyte. Therefore, the ion diffusion in ether is faster than that in ester electrolytes. Furthermore, the cations in ether electrolyte are easier to be isolated, meaning that the interaction between the cations and anions in ether electrolyte is weaker than that in ester electrolytes. This weaker strength will make the cations and anions have the benefit of separating from each other and approaching the active sites.

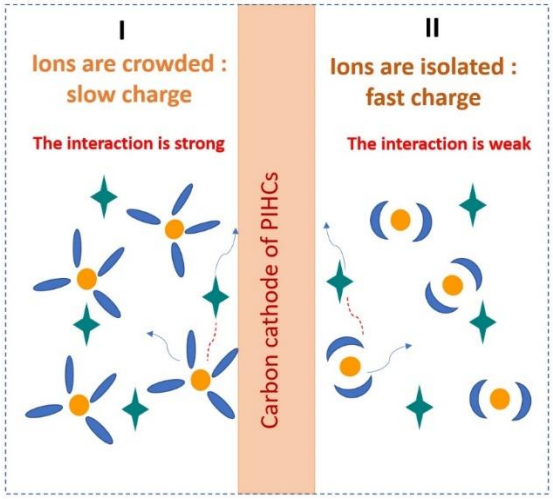

Figure 5-11 Illustration of the ion diffusion in ether and ester electrolytes.

5.2.5 Electrochemical performance of full PIC

Graphite as a commercial lithium-ion battery anode has been applied and developed for several decades. The manufacture and cost of fabricating graphite anode shall be sustainable and low cost. Selecting graphite as the anode of PIC could be one of the best choices. However, graphite cannot enable high-rate charge and discharge in ester electrolytes though it has been demonstrated the capability of reversible storing potassium ions. This drawback will rigorously limit the output power density of the capacitor. Moreover, graphite is also the precursor of fabricating graphite oxide, the industrial-scale fabrication of both electrodes will be much more cost-effective. In a word, it will be a solid step to promote the commercial

application of PIC if a suitable electrolyte can be selected so that these two electrode materials can exhibit ultra-high electrochemical performance.

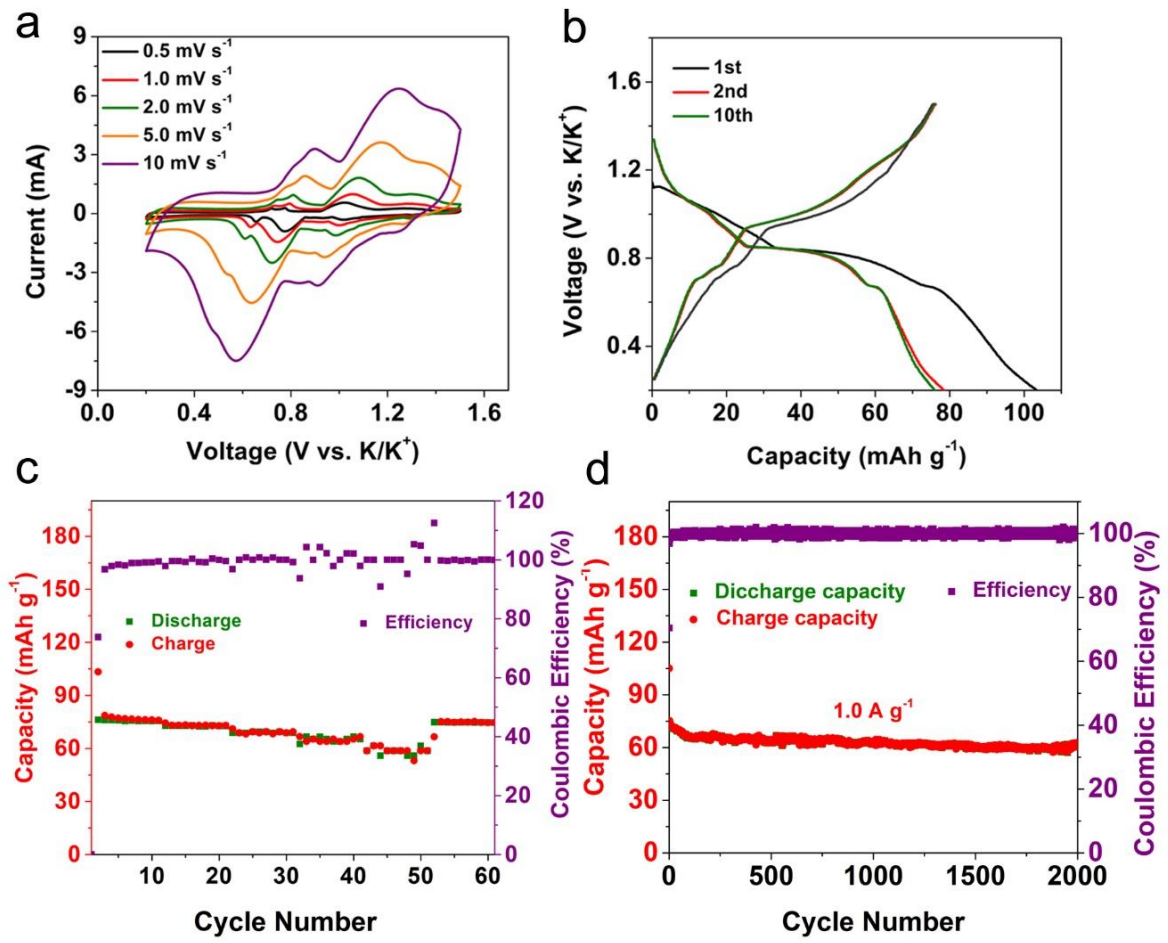

Figure 5-12 Electrochemical performance of commercial PG electrode. (a) CV curves. (b) Charge-discharge profiles at 0.5 A g^{-1}. (c) Rate performance at various current densities from 0.5–10 A g^{-1}. (d) Cycling performance at the current density of 1 A g^{-1}.

Herein, a full PIC is configurated by utilizing GO as the cathode, commercialized PG as the anode, and DME as the electrolyte solvent. This prototype is proposed as GO‖DME‖PG. The graphite anode is investigated in DME electrolyte within a voltage window of 0.01–1.5 V. As shown in Figure 5-12a, the CV curves of graphite anode at different scan rates possess two pairs of anodic and cathodic peaks, which is corresponding to the different states of the co-intercalation of K^+-solvent complex in graphite. Moreover, the reversible peaks observed at low and high rates show small deviation, meaning the high reversibility and small polarization of the co-intercalation ion storage in graphite in DME electrolyte. Figure 5-12b shows the discharge-charge profiles of graphite anode at the 1st, 2nd, and 10th cycles. The first discharge

capacity is higher than the second one, which is attributed to the SEI formation.[81] The profiles of the 2nd and 10th cycles are overlapped well, further indicating that the graphite anode possesses good reversibility and cyclability. As shown in Figure 5-12c, the graphite anode exhibits an excellent rate capability, it can deliver the capacities of 77, 73, 69, 64, and 59 mAh g^{-1} at current densities of 0.5, 1.0, 2.0, 5.0, and 10 A g^{-1}, respectively. This rate performance of the graphite anode in the ether electrolyte is much better than that in the ester electrolytes, suggesting a wise decision of using graphite as the anode in the GO-DME configuration. Figure 5-12d shows the long cycling performance of the graphite anode, and it can maintain a capacity of 63 mAh g^{-1} after 2000 cycles at a high current density of 1.0 A g^{-1}.

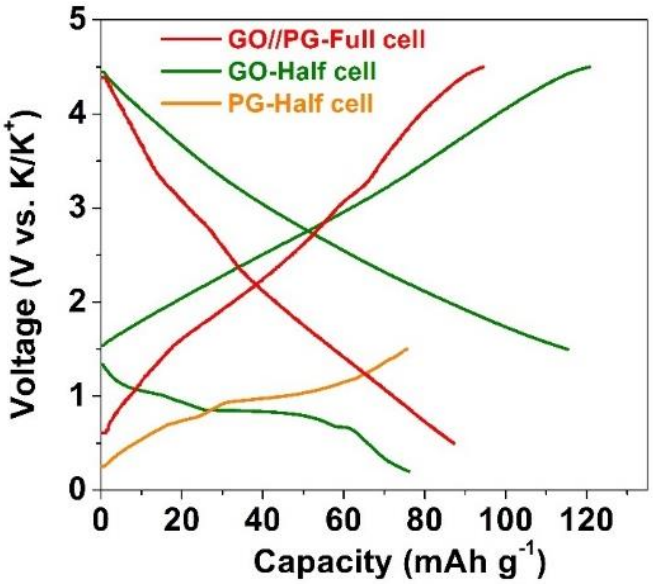

Figure 5-13 Charge-discharge profiles for the different cell configuration.

The full PICs are operated within the voltage window of 0.5–4.5 V according to the working voltage and capacities of GO and PG in half cells (Figure 5-13). The active mass ratio for the anode to cathode is fixed to be about 1.5. It is worth noting that this full PIC possesses a high voltage window output, which outperforms most of PICs that have been reported previously. The working mechanism of this prototype in the ether-based electrolyte is that the cathode reversibly stores the cations and anions through the electrode interface adsorption, the anode reversibly stores the cations through the co-intercalation (Figure 5-14a). Both adsorption and co-intercalation possess fast ion-storage kinetics, which enables an ultrafast potassium-ion capacitor. Figure 5-14b shows the excellent rate performance of GO‖DME‖PG capacitor at various high current densities, it delivers high capacities of 89, 85, 81, 76, and 72 mAh g^{-1} at

0.5, 1, 2, 5, and 10 A g^{-1}. The profiles in Figure 5-14c display the symmetric characteristic of capacitor devices without obvious polarization. Furthermore, as shown in Figure 5-4d, the capacitor exhibits a long-term cyclability which can cycle for up to 2500 cycles with 84% capacity retention. The energy/power densities of this capacitor are evaluated by multiplying the voltage and specific capacity factors. The Ragone plots in Figure 5-14e exhibit that the GO‖DME‖PG prototype can provide the highest energy/power densities, as compared with other reported PIHCs.[86, 88, 90, 119, 156, 176, 210, 211] A superb energy density of 190 Wh kg^{-1} can be obtained at a power density of 969 W kg^{-1}, even at a high power density of 21443 W kg^{-1}, an impressive energy density of 150 Wh kg^{-1} maintains (calculated based on total mass: 76 Wh kg^{-1} at 388 W kg^{-1}, 60 Wh kg^{-1} at 8577 W kg^{-1}). These values are also highly competitive with the reported LICs and SICs.[31] Here, considering that the anode and electrolyte sources are commercialized, and GO fabrication can be industrialized too, once again it highlights the attractiveness of our proposed prototype. We believe that GO‖DME‖PG could be a priority prototype to be further improved with industrial-style engineering optimization.

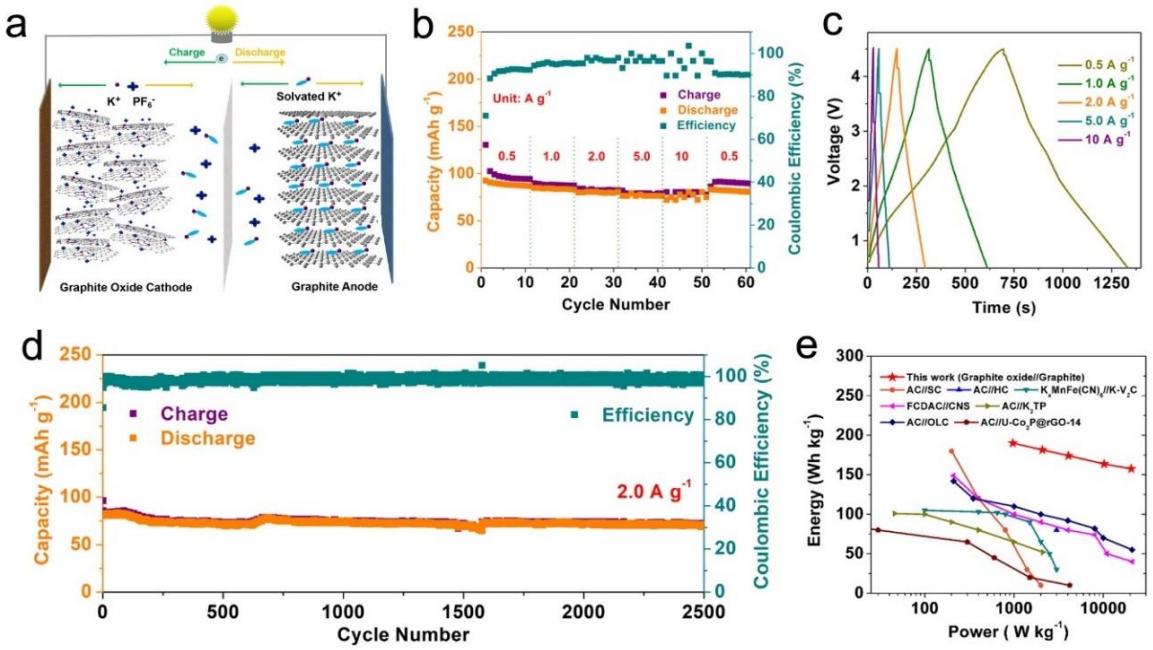

Figure 5-14 Electrochemical performances of the GO‖DME‖PG capacitor. (a) Schematic illustration of the charging and discharging process in the full potassium-ion capacitor. (b) Rate performance and (c) rate profiles at various rates. (d) Cycling performance at 2 A g^{-1}. (e) Ragone plots in comparison with other previously reported PIHCs (Calculated based on cathode active mass).

5.3 Conclusion

A systematic investigation of the relationship between the electrochemical performances and electrolytes demonstrates that the interaction between the cations and anions in electrolytes plays a crucial role in determining the ion-storage behavior for the carbon-based cathode of PICs. The DME solvent can separate cations and anions effectively compared to the EC^DEC and EC^PC solvents, which contributes to more freedom of ion diffusion in PICs. On that basis, a capacitor prototype, GO‖DME‖PG, is proposed. The fast ion-storage kinetics of the ion adsorption on the cathode and the co-intercalation on the anode enables a superior electrochemical performance which exhibits a high energy density of 190 Wh kg^{-1} at 969 W $kg^{-1}_{Cathode}$, 150 Wh kg^{-1} at 21443 W $kg^{-1}_{Cathode}$. More broadly, this work suggests a new idea of identifying electrolytes that can achieve enhanced high-rate performance for the carbon-based PICs.

6 Synergy between adsorption and co-intercalation enables superior sodium-ion storage for SIC anode

The electrochemical mechanism of carbon anode materials in SICs generally involves the adsorption at the positions of the defects and electrode surface, and single-ion insertion in expanded carbon layers. However, the single-ion insertion mechanism is intrinsically sluggish due to the large size of sodium ions, which significantly restricts the graphite oxides to achieve superior rate performance. Fortunately, the co-intercalation mechanism demonstrated in graphite intrinsically possesses superior fast ion-storage kinetic. In this regard, integrating the adsorption mechanism with the co-intercalation mechanism may greatly enhance the rate capability of sodium-ion storage in the carbon materials which possess both ordered and disordered carbon layers. We take reduced graphite oxide (RGO) as an example to realize this proposal. The RGO electrode exhibits a superior rate capability in DME electrolyte. The reaction mechanism shows that the ion storage of RGO undergoes co-intercalation and surface adsorption. As compared with the traditional mechanism, this new combination mechanism could efficiently make use of the active sites in the ordered carbon layers in graphite oxides. Furthermore, we utilize RGO as the cathode and anode to assemble a symmetrical sodium-ion capacitor. The full capacitor outputs high energy density and power density, demonstrating enormous potential as the supplementary power supply for practical applications.

6.1 Experimental section

The RGO anode electrodes are fabricated by annealing the GO nanosheets at different temperatures. The fabrication detail of GO is described in chapter 5.1.1. The RGO200, RGO400, and RGO600 electrode materials are obtained by respectively annealing the GO nanosheets at 200 ℃, 400 ℃, and 600 ℃. The battery assembly, material characterizations, and electrochemical investigations are conducted using the same methods and instruments as described in chapter 5.1.2 and chapter 5.1.3. As shown in Figure 6-1a–b, the SEM images of RGO nanosheets show similar morphology to the GO, as described in Chapter 5.2. HRTEM image further demonstrates that as-prepared RGO nanosheets also possess a high content of disordered carbon layers and ordered carbon layers, which is a typical characteristic of RGO material.[214] In this regard, the RGO anode material is very suitable for investigating the adsorption and intercalation mechanisms for sodium-ion storage.

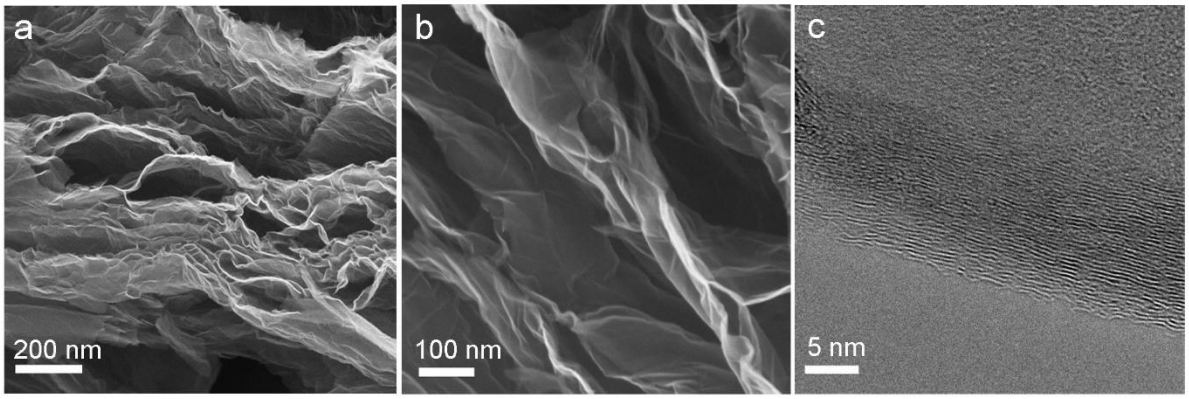

Figure 6-1 (a) low- and (b) high-magnification SEM images of the RGO nanosheets. (c) HRTEM image of the RGO nanosheets.

6.2 Results and discussions

6.2.1 Electrochemical performance of RGO in different electrolytes

To identify the best object for further studying its electrochemical behavior in different electrolytes, the rate performance tests on the RGO200, RGO400, and RGO600 electrodes are systematically conducted in different electrolytes. All the cells are configurated by utilizing RGO nanosheets as the working electrodes and sodium metal as the counter electrodes. Among all the electrolytes utilized in SIBs, $NaPF_6$ is one of the most common solutes. The mixtures of ethylene carbonate/diethyl carbonate (EC/PC) and ethylene carbonate/propylene carbonate (EC/DEC) are the most common ester solvents, and dimethyl glycol (DME) is the most common ether solvent.[190, 222] Therefore, $NaPF_6$ in DME, EC/DEC, and EC/PC are prepared and utilized to assemble the cells. Their rate performances are investigated at various current densities ranging from 0.1, 0.2, 0.5, 1.0, 2.0, 5.0, 10, and 20 A g^{-1}. Figure 6-2a shows that RGO200 in EC/PC delivers the highest specific capacity at the low current density of 0.1 A g^{-1}, whereas RGO200 in DME delivers the highest specific capacity of 100 mAh g^{-1} at the high current density of 20 A g^{-1}. This feature changed after we tested the RGO400 and RGO600. As shown in Figure 6-2b and 6-2c, RGO in DME exhibits a greater rate capability as compared with RGO in EC/DEC and EC/PC. Especially, RGO400 in DME shows the best rate capability, it delivers the specific discharge capacity of 259, 244, 229, 210, 196, 179, 167, and 166 mAh g^{-1} with the increasing current densities. As a contrast, RGO400 in EC/DEC delivers the specific discharge capacity of 220, 198, 175, 152, 130, 96, 61, and 33 mAh g^{-1}, RGO in EC/PC delivers the specific discharge capacity of 255, 210, 176, 153, 129, 90, 53, and 29 mAh g^{-1} at the same current densities. In addition, RGO400 in DME exhibits a better recovery capability after cycling at various current densities. Its capacity can maintain a high capacity of 256 mAh g^{-1} when the cell is tested at the current density of 0.1 A g^{-1} again.

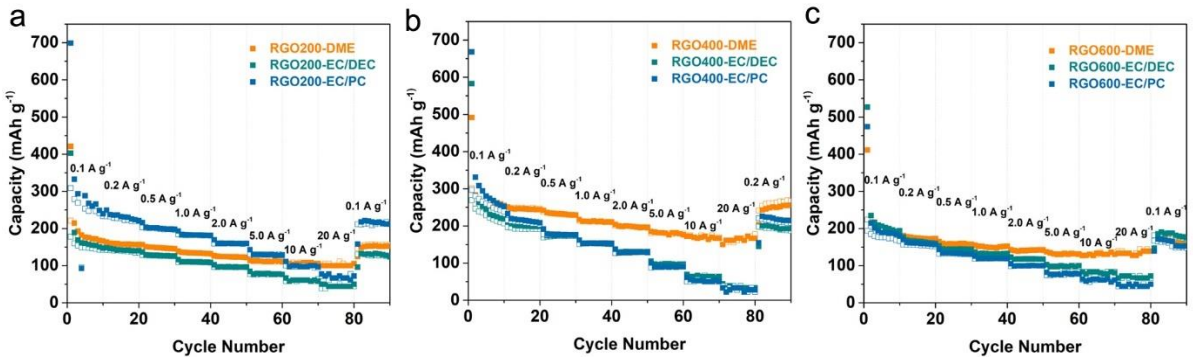

Figure 6-2 The rate performance of (a) RGO200, (b) RGO400, and (c) RGO600 in different electrolytes.

The corresponding charge-discharge profiles are shown in Figure 6-3. All the profiles are sloping without charge-discharge plateaus. It is because the graphite oxides possess inhomogeneous carbon layers including the short-range ordered carbon layers and disordered carbon layers that store sodium ions with different binding energy, outputting various charge-discharge reaction potentials. Furthermore, as compared with the electrodes in EC/DEC (Figure 6-3b, 6-3e, and 6-3h) and EC/PC (Figure 6-3c, 6-3f, and 6-3i) electrolytes, the electrodes in DME (Figure 6-3a, 6-3d, and 6-3g) clearly exhibit the minimum polarization. This result may be attributed to the fast ion-storage kinetics of the RGO electrodes in the DME electrolyte. Since the ion-storage kinetics in ether electrolytes is faster than that in ester electrolytes, we speculate that the co-intercalation mechanism occurred in the short-range carbon layers of electrodes in the DME electrolyte.

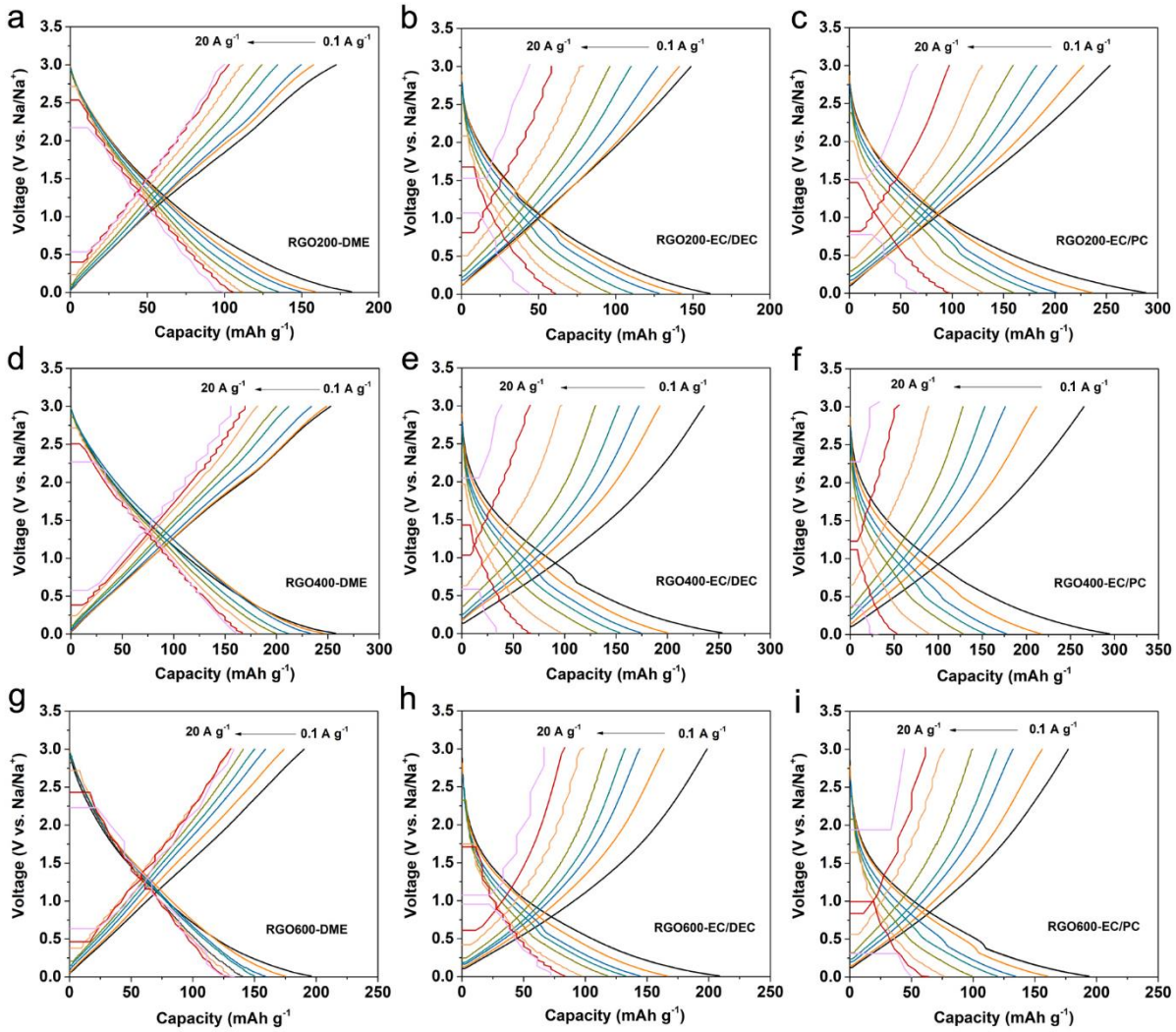

Figure 6-3 Charge-discharge profiles of RGO200 in (a) DME, (b) EC/DEC, and (c) EC/PC electrolytes. Charge-discharge profiles of RGO400 in (d) DME, (e) EC/DEC, and (f) EC/PC electrolytes. Charge-discharge profiles of RGO600 in (g) DME, (h) EC/DEC, and (i) EC/PC electrolytes.

Based on the above investigation, the RGO400 electrode is selected to further study the electrochemical behavior in the different electrolytes. The CV curves of RGO400-DME, RGO400-EC/DEC, and RGO400-EC/PC are investigated in the voltage window of 0.01–3 V at the scan rate of 0.2 mV s^{-1}. As shown in Figure 6-4a, the CV curves of RGO400 in DME display a quadrate shape which is obviously different from the CV curves of RGO400 in EC/DEC (Figure 6-4b) and EC/PC (Figure 6-4c) electrolytes. It indicates that the ion-storage behavior of RGO400 in DME electrolyte is similar to the pseudocapacitive electrochemical behavior.[193, 198] Moreover, another big difference between them is the first cathodic scan. In

Figure 6-4b and **6-4c**, the broad peaks below 0.5 V could be attributed to the overlapping responses of the reversible ion storage reactions and irreversible side reactions. The reversible reactions include the ion adsorption at the surface and defects of the carbon layers, redox reaction between the sodium ions and some doped oxygen-containing functional groups. The irreversible reactions include reactions of electrolyte decomposition (SEI formation) and the reactions between the sodium ions and some other doped oxygen-containing functional groups. The peaks at around 0.35 V can be attributed to the irreversible ion intercalation between the carbon layers.[223] In the case of DME electrolyte, the overlapping peaks are broader, which is attributed to the higher voltage of co-intercalation instead of the single ion intercalation.

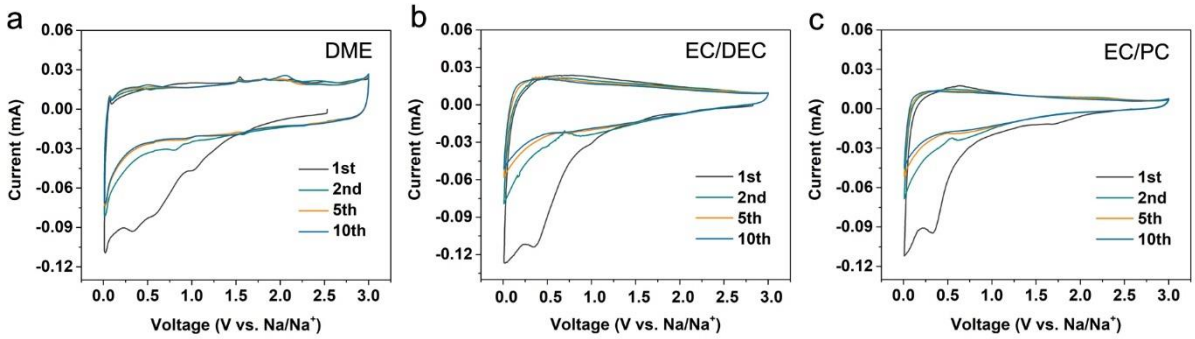

Figure 6-4 Initial CV curves of RGO400-DME, RGO400-EC/DEC, and RGO400-EC/PC at the scan rate of 0.2 mV s^{-1}.

The long cycling performances of the RGO400-DME, RGO400-EC/DEC, and RGO400-EC/PC electrodes at a low current density of 50 mA g^{-1} are also assessed. As shown in Figure 6-5a, an interesting phenomenon is observed that the capacity of RGO400-DME first decreases then gradually increases with the cycle number increasing, while RGO400-EC/DEC and RGO400-EC/PC just decrease continuously. The initial capacity decrease for all three samples is ascribed to the irreversible side reactions and SEI formation reactions. The subsequent capacity increase for RGO400-DME and the capacity decrease for RGO400-EC/DEC and RGO400-EC/PC can be attributed to the better or worse evolution of the carbon layer structure after the sodiation and desodiation processes. For the electrode of RGO400-DME, the co-intercalation of Na^+-solvent complex in carbon layers may create some new active sites for the sodium-ion storage, which leads to the capacity increase. In addition, the charge capacity and discharge capacities of RGO400-DME overlap each other after 5 cycles, whereas it takes at least 20 cycles for RGO400-EC/DEC and RGO400-EC/PC to reach the overlap. It demonstrates the fewer side reactions and thinner SEI formation in DME electrolyte. Figure

6-5b–d shows the corresponding charge and discharge profiles at the 1st, 10th, 50th, and 100th cycles. The first charge and discharge capacities are 331 and 555 mAg g^{-1} for RGO400-DME, 433 and 1328 mAh g^{-1} for RGO400-EC/DEC, and 432 and 1098 mAh g^{-1} for RGO400-EC/PC, giving the first-cycle coulombic efficiencies of 60%, 33%, and 39%, respectively. The initial coulombic efficiency in DME electrolyte is apparently higher than that in EC/DEC and EC/PC electrolytes. It is attributed to the limited side reactions in DME electrolyte. A similar trend has been observed in the previous works in LIBs and SIBs.[224] Moreover, the charge and discharge profiles of RGO400-DME at the 10th, 50th, and 100th cycles are sloping curves with several small plateaus, whereas those of RGO400-EC/DEC and RGO400-EC/PC are sloping and smooth curves. The more and more apparent plateaus are induced by the increasing active sites for the additional sodium-ion reversible storage reactions. In the end, the RGO400-DME, RGO400-EC/DEC, and RGO400-EC/PC electrodes respectively deliver capacities of 403, 280, and 205 mAh g^{-1} after 100 cycles. It further demonstrates that the RGO400 electrode favors DME electrolyte.

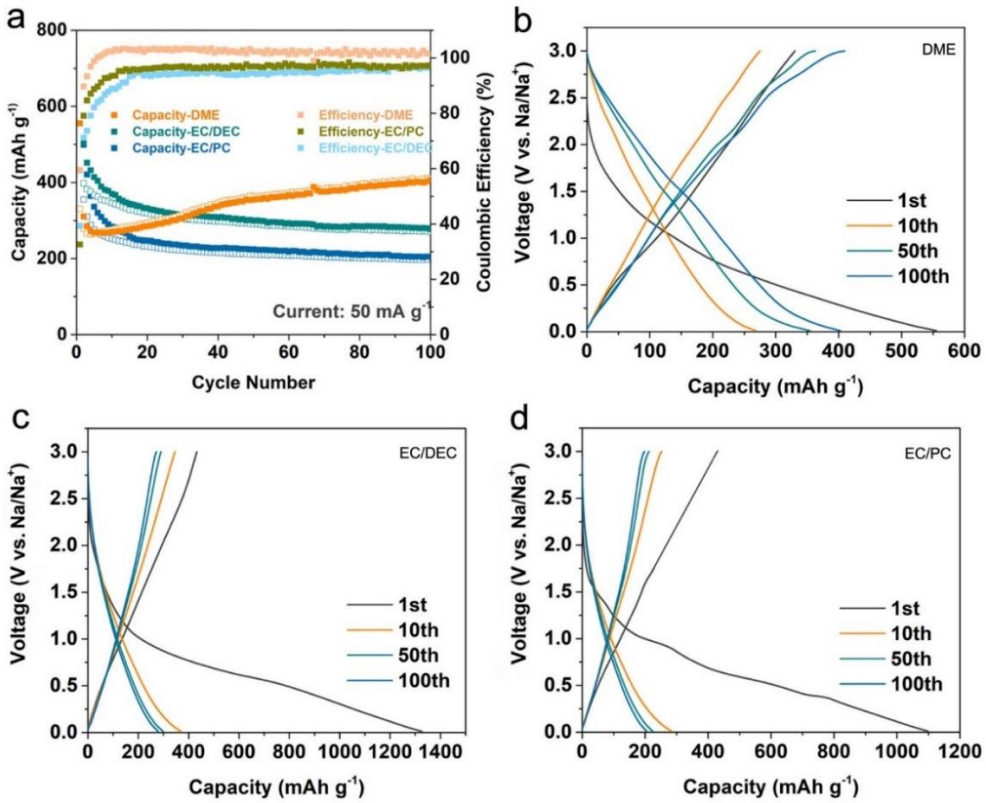

Figure 6-5 (a) Cycling performance of RGO400-DME, RGO400-EC/DEC, and RGO400-EC/PC at 50 mA g^{-1}. The corresponding charge-discharge profiles of (a) RGO400-DME, (b) RGO400-EC/DEC, and (c) RGO400-EC/PC at the 1st, 10th, 50th, and 100th cycle.

6.2.2 Ion-storage kinetics analysis

To investigate the kinetics o0f the electrodes in different electrolytes, the CV measurements at scan rates of 0.2 to 10 mV s^{-1} are carried out. In contrast to the cases of RGO400-EC/DEC and RGO400-EC/PC, the broad sodiation/desodiation peaks in the case of RGO400-DME (Figure 6-6a) are maintained at high scan rates, and the desodiation peaks toward low voltage and sodiation peaks toward high voltage can be clearly observed. The cathodic and anodic peaks of RGO400-EC/DEC (Figure 6-6b) and RGO400-EC/PC (Figure 6-6c) electrodes become steeper and show large polarization. The difference between the shapes of the CV curves suggests that the ion-storage kinetics of RGO400-DME possesses a capacitor-like characteristic.

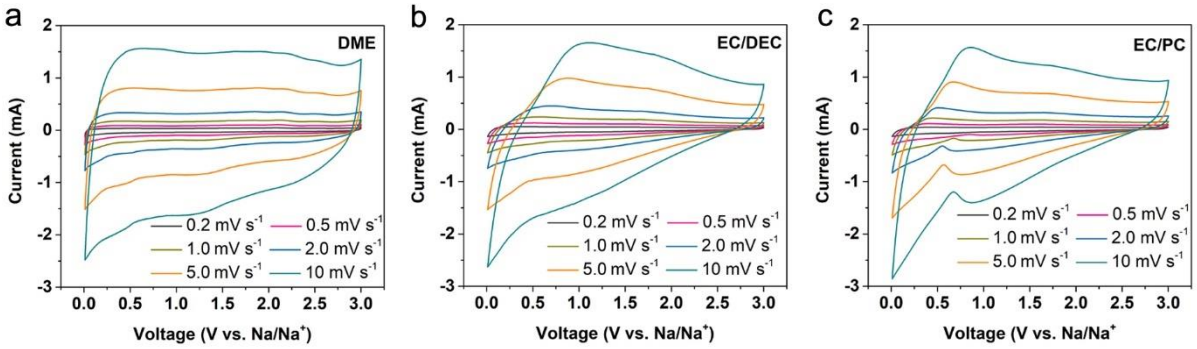

Figure 6-6 CV curves of (a) RGO400-DME, (b) RGO400-EC/DEC, and (c) RGO400-EC/PC electrodes using various scan rates of 0.2–10 mV s^{-1}.

Further analysis quantitatively determines the contribution of the capacitor-like capacitance by using the relationship of the current response, i, with the combination of capacitor-like behavior (k_1v) and diffusion behavior ($k_2v^{1/2}$), obeying the equation:

$$i = k_1 v + k_2 v^{1/2} \qquad Eq.10$$

by calculating the k_1 and k_2, the two different ion-storage characteristics can be differentiated.[194, 225] As shown in Figure 6-7a, the contribution proportions of the capacitor-like behavior of RGO-DME are higher than 50% at different scan rates, suggesting the dominance of the ion-storage kinetics is capacitive characteristic. Moreover, the contributions enlarge with increasing scan rates for all RGO electrodes. It is because the retardation of the ion diffusion and electron transfer in the bulk of the active materials at high scan rates results in the decrease of the diffusion-controlled ion storage reactions, which leads to the domination of the surface reversible reactions. A similar trend can be observed in many reported works in

SICs and SIBs. Figure 6-7b–d show that the specific capacitor-like contribution fractions of RGO400-DME, RGO400-EC/DEC, and RGO400-EC/PC are 73%, 51%, and 51%, respectively. The above results demonstrate that the major energy-storage mechanism of RGO400-DME exhibits the capacitor-like characteristic enabling the outstanding rate capability.

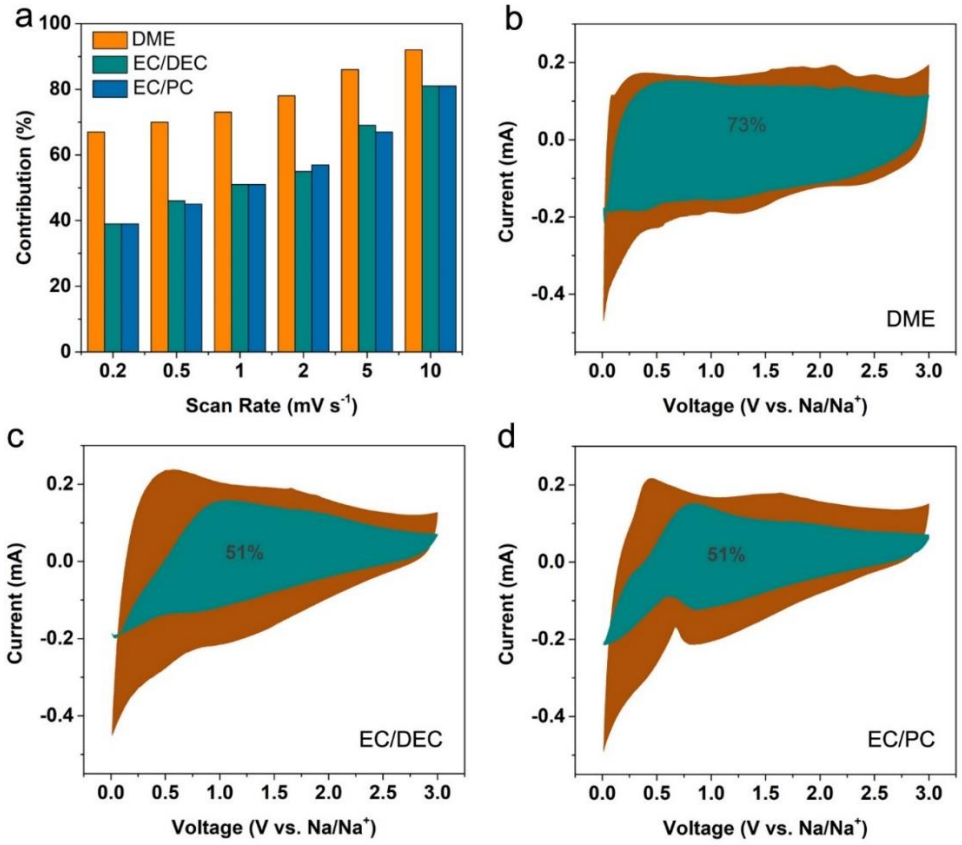

Figure 6-7 (a) Contribution of the capacitor-like behavior in the RGO400-DME, RGO400-EC/DEC, and RGO400-EC/PC electrodes at different scan rates. Separation of the contribution fractions at scan rate of 1.0 mV s^{-1} in (b) RGO400-DME, (c) RGO400-EC/DEC, and (d) RGO400-EC/PC.

The EIS measurement is performed to investigate the charge transfer kinetics of RGO400 before and after cycling in various electrolytes. The semicircle of the Nyquist plot in the middle frequency region is related to the charge transfer impedance (R_{ct}), while the linear part of the Nyquist plot in the low-frequency region is related to the Warburg impedance (Z_w).[226] In this measurement, the applied voltage of the alternating current is 5.0 mV and the applied frequency ranges from1.0 MHz to 50 mHz. The EIS measurements are conducted for the fresh,

the 5th-cycle, and the 50th-cycle cell. Figure 6-8a shows the EIS spectra of RGO-DME. For the fresh cell, the diameter of the semicircle is the largest, indicating the highest R_{ct}. While after 5 cycles, the diameter of the semicircle shortens sharply, corresponding to the sharp decrease of the R_{ct}. This phenomenon is commonly observed in the electrode materials for SICs and SIBs, which is attributed to the enhancement of the contact between the electrode and electrolyte after certain cycles. Furthermore, the diameter of the semicircle continuously shortens, suggesting that the potassiation and depotassiation may activate the surface reaction thus enhancing the charge transfer at the interface. This result agrees well with the electrochemical behavior of the RGO400 at the low current density. In the cases of RGO400-EC/DEC (Figure 6-8b) and RGO400-EC/PC (Figure 6-8c), For the fresh cells, they display a similar phenomenon as compared to RGO400-DME, exhibiting the largest diameters of the semicircles. However, the R_{ct} values of the three samples are different, which is attributed to the wettability of carbon materials in different electrolytes. Another critical difference is the increasing trend of the R_{ct} values of RGO400-EC/DEC and RGO400-EC/PC from the 5th-cycle to the 50th-cycle cells, which can be correlated to the thick SEI formation in EC/DEC and EC/PC electrolytes. The above observations are consistent well with electrochemical behaviors of RGO400-EC/DEC and RGO400-EC/PC.

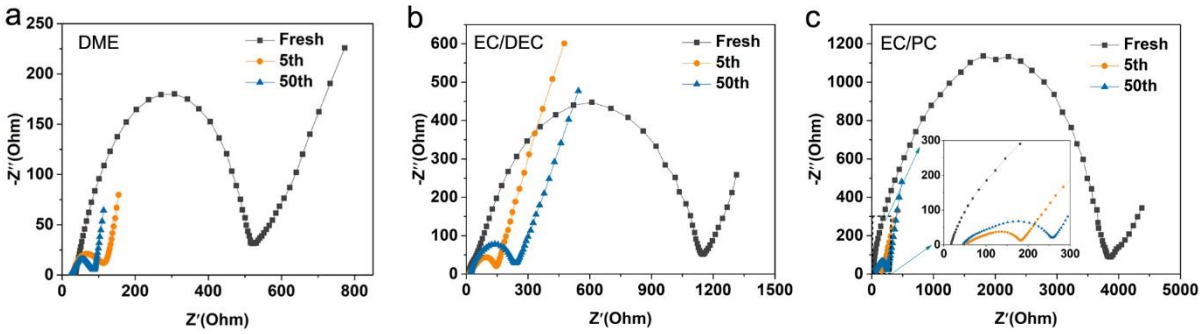

Figure 6-8 EIS Nyquist plots of the (a) RGO400-DME, (b) RGO400-EC/DEC, and (c) RGO400-EC/PC electrodes.

6.2.3 Ion-storage mechanism investigation

The intrinsic reason for the outstanding electrochemical behavior of RGO400-DME could be the advantage of its unique ion storage mechanism. To further verify this consequence, the HRTEM images of RGO400 are characterized after the 1st discharge process in different electrolytes. Through the comparison of those three electrodes with the pristine RGO400, the change of the carbon layer structures of RGO400 can be observed after the sodium-ion storage

in different electrolytes. As shown in Figure 6-9a, the distinct feature of the pristine RGO400 is that the carbon layer structure consists of ordered carbon layers and short-range ordered carbon layers. After the sodium-ion storage in the RGO, the carbon layer structure of RGO400-DME becomes more disordered, and it is basically difficult to observe the short-range ordered carbon layers (Figure 6-9b). The phenomenon should be ascribed to the co-intercalation of the solvated-Na^+ complexes in the ordered carbon layers in DME electrolyte, and the large solvated-Na^+ complexes deform the ordered carbon layer.[227] Whereas the carbon layer structures of RGO-EC/DEC (Figure 6-9c) and RGO-EC/PC (Figure 6-9d) have a minor change, the short-range carbon layers still can be observed in both electrodes. It implies that the sodium-ion storage order carbon layers are unable to efficiently store sodium ions in EC/DEC and EC/PC electrolytes.

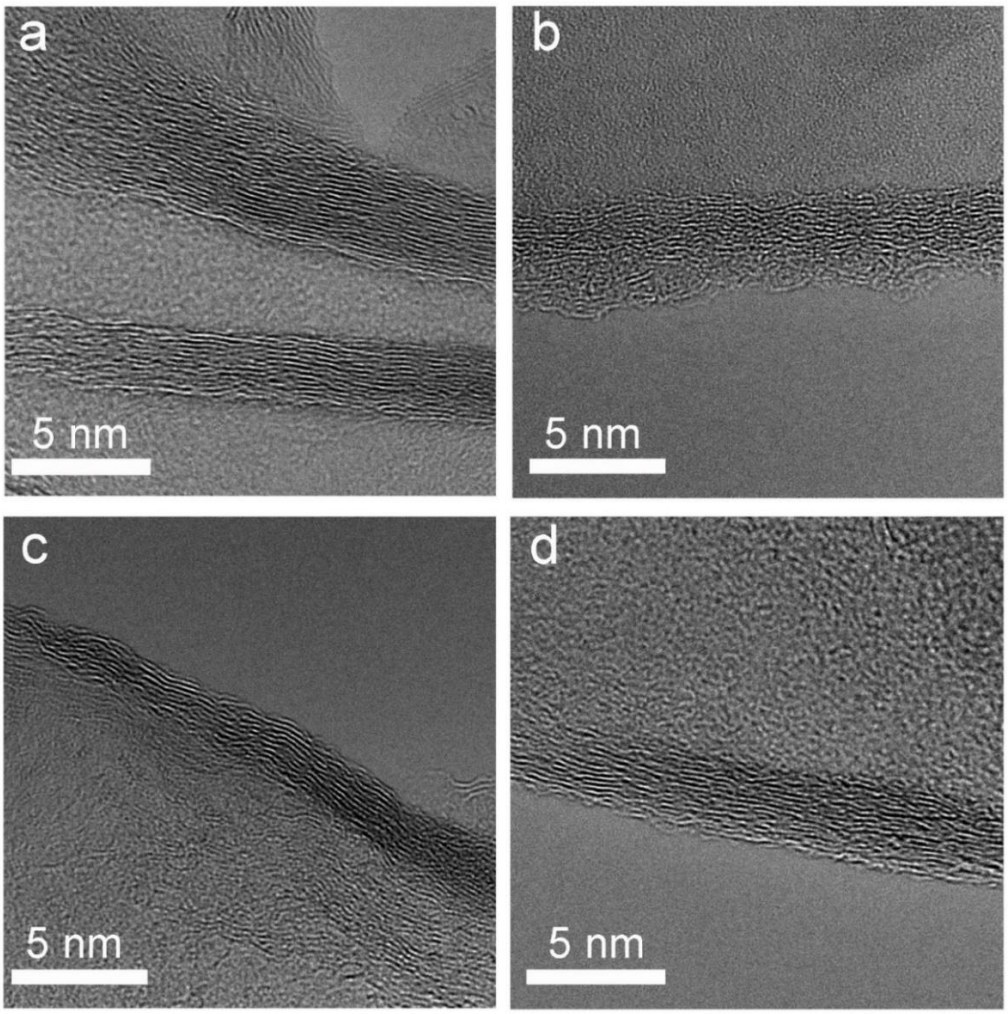

Figure 6-9 HRTEM images of (a) pristine RGO400, (b) RGO400-DME, (c) RGO400-EC/DEC, and (d) RGO400-EC/PC after the 1st discharge at current density of 500 mA g^{-1}.

The change of carbon layer structures of RGO400 is further investigated by the Raman spectra. The G-band is a characteristic feature of ordered carbon layers for a carbon material, while D-band is corresponding to the disordered carbon layers. Raman spectroscopy is a sensitive measurement to interpret the variation of the carbon layer structure.[99] As shown in Figure 6-10a, the intensity of the D-band is lower than that of the G-band for pristine RGO400, which is similar to the results for RGO-EC/DEC (Figure 6-10c) and RGO-EC/PC (Figure 6-10b) after the 1st discharge process. Whereas the intensity of the D-band is higher than that of the G-band for RGO-DME (Figure 6-10b). Correspondingly, the value of I_D/I_G of RGO-400 is 1.01, which is higher than that of RGO-EC/DEC (0.99), RGO-EC/PC (0.98), and pristine RGO400 (0.98). This result again demonstrates that the carbon layers of RGO400-DME become more disordered after sodium-ion storage, while RGO-EC/DEC and RGO-EC/PC still preserve their ordered carbon layers.

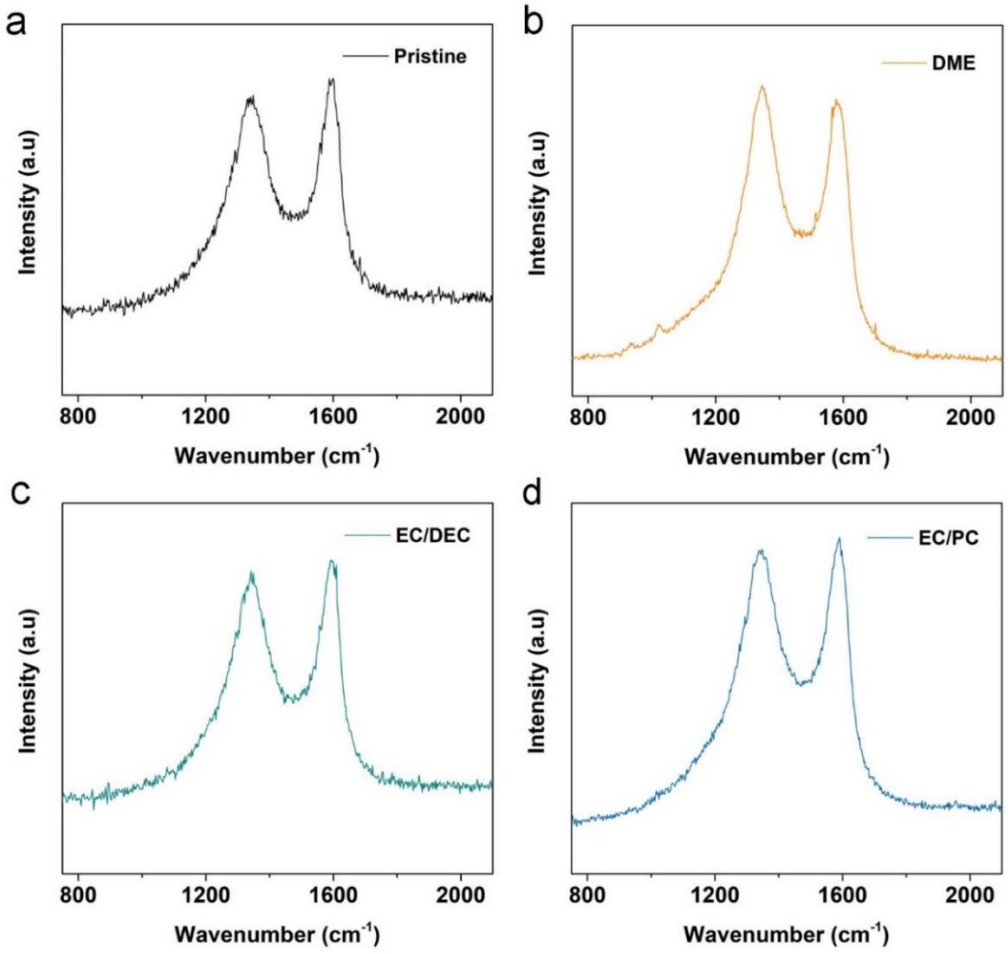

Figure 6-10 Raman spectra of (a) pristine RGO400, (b) RGO400-DME, (c) RGO400-EC/DEC, and (d) RGO400-EC/PC after the 1st discharge process at current density of 500 mA g^{-1}.

The HRTEM images and Raman spectra all demonstrate that RGO400-DME has an obvious structure variation for the carbon layers, which suggests the occurrence of the co-intercalation in RGO400 carbon layers in DME electrolyte. By cooperating the co-intercalation mechanism with the adsorption mechanism, RGO400 can efficiently store sodium ions utilizing not only the defect and nanovoids of the carbon layers but also the ordered carbon layers. The specific capacity of RGO400-DME is improved. Furthermore, owing to the fast kinetics of co-intercalation, the rate capability of RGO400-DME is enhanced.

6.2.4 Full ion capacitor assembly

According to the sloping shape of charge and discharge profiles of RGO400-DME, it is better to employ it as the anode of SICs instead of SIBs. The fast charge and discharge properties also comply with the rule of developing SIC electrodes. To assemble a symmetric SIC, RGO400‖DME‖RGO400, the pre-potassiation on the RGO400 needs to be conducted in the half cell by charging and discharging at 50 mA g^{-1} within a voltage window of 0.01–3 V for 10 cycles. Through tuning the mass loading ratio of the cathodic and anodic RGO400, the optimum matching of a proper voltage window and capacity for the full SIC can be realized. As shown in Figure 6-11a, the symmetric SIC exhibits high capacities of 76, 70, 63, 55, 53 mAh g^{-1} at current densities of 0.5, 1.0, 2.0, 5.0, and 10 A g^{-1}. The corresponding voltage-time profiles in Figure 6-11b also show that the SIC can achieve fast full charge and discharge within minutes. Furthermore, the cycling performance of the symmetric SIC also is investigated (Figure 6-11c), delivering a high capacity of 54 mAh g^{-1} at the current density of 5.0 A g^{-1}. Figure 6-11d presents the Ragone plot of the SIC based on the total mass of both electrodes. The SIC can deliver an energy density up to 92 Wh kg^{-1} at a power density output of 631 W kg^{-1}, even at a very high power density of 10896 W kg^{-1}, it still maintains an impressive energy density of 48 Wh kg^{-1}. The high energy and power density outputs of the demonstrated symmetric SIC are superior to those of previously reported SICs and are even comparable to the state-of-the-art LICs.[121, 228, 229]

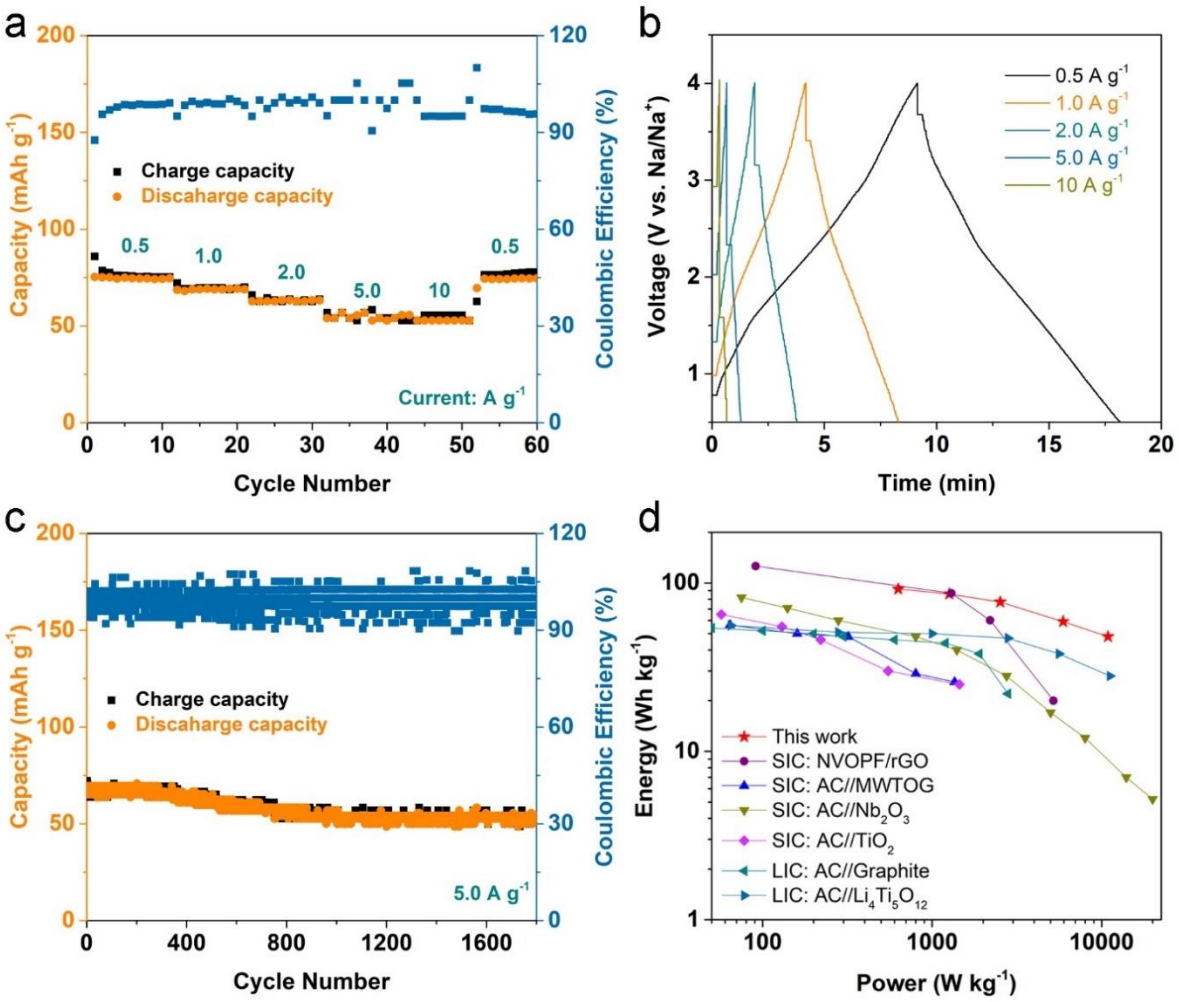

Figure 6-11 (a) Rate performance of the symmetric SIC: RGO400‖DME‖RGO400 at various current densities from 0.5 to 10 A g^{-1}. (b) Corresponding charge-discharge profiles. (c) Cycling performance at current density of 5.0 A g^{-1}. (d) Ragone plots of RGO400‖DME‖RGO400 and the reported state-of-the-art hybrid SICs and LICs.

6.3 Conclusion

The electrochemical performance of RGO400 has been systematically studied in different electrolytes. The RGO400 in DME outperforms that in EC/DEC and EC/PC in terms of the reversible storage capacity, rate capability, and cyclability. It can deliver a high specific capacity of 403 mAh g^{-1} at the current density of 50 mA g^{-1}, even at 20 A g^{-1}, it still maintains a specific capacity of 166 mAh g^{-1}. The analysis of the ion storage kinetics and mechanism demonstrates that RGO400 can store sodium ions through a combination mechanism of adsorption and co-intercalation in DME electrolyte, which is different from the conventional ion storage mechanism in EC/DEC and EC/PC electrolytes, endowing the RGO400 electrode with improved sodium-ion storage performance. Finally, a full SIC is assembled by using RGO400 as both cathode and anode. It also exhibits an excellent energy storage performance with a high energy density of 91 Wh kg^{-1} and a high power density of 10896 W kg^{-1}.

7 Summary and outlook

In summary, three different strategies are introduced to improve the ion storage performance of PICs and SICs by focusing on the investigations of three major components of HICs, cathode, electrolyte, and anode. The main contributions of this dissertation are concluded in the following aspects:

(1) Creating more and stable active sites for the potassium-ion storage of PIC cathode:

The nitrogen-doped soft carbon nanofibers are fabricated as the precursor since they contain many defects for the subsequent oxygen functionalization. After immersing them in a strong acid mixture, the highly oxygen functionalized carbon nanofibers are obtained. The oxygen functionalized carbon nanofibers exhibit an improved electrochemical performance for the cathode of PICs. The ion storage kinetics and mechanism studies demonstrate that the surface redox reactions dominate the ion storage enabling high rate capability, and the major surface redox reactions are the reversible reactions between potassium ions and oxygen-containing functional groups. Furthermore, a series of different carbon materials are investigated as the precursors for preparing oxygen functionalized carbon cathode for PICs. It demonstrates that the graphitization and defect are key factors for the ion-storage performance. The high graphitization carbon materials possess stable ion storage capability, while the carbon materials with abundant defects possess high ion storage capacity. Finally, a full dual-carbon PIC is configurated by using the nitrogen-doped carbon precursor as the anode and oxygen functionalized carbon nanofibers as the cathode. It exhibits a high energy density of 135 Wh kg^{-1} and a high power density of 1500 W kg^{-1}. This work may shed light on designing high-performance PIC cathodes and open up an avenue towards future energy storage technologies with low cost and material sustainability.

(2) Identifying suitable electrolyte for dual-ion storage of PIC cathode:

The graphite oxide nanosheets are utilized as the cathode for PIC. A systematic investigation of the cathode in three different electrolytes is carried out. The electrochemical performances show that the cathode in DME electrolyte outperforms that in EC^DEC and EC@PC electrolytes. The ion storage kinetics analysis shows that the cathode in DME is better than that in EC^DEC and EC@PC electrolytes, which further demonstrates that ion storage in DME is faster. The characterizations of the electrolytes demonstrate that the cations are isolated by the solvents, suggesting a weaker interaction between the cations and anions in DME

electrolyte. It endows the ions with more freedom of diffusion, which plays a key role in the dual-ion storage. Furthermore, a low-cost full dual-carbon PIC is configurated by using pristine graphite as the anode and graphite oxide as the cathode in DME electrolyte, GO‖DME‖PG. Owing to the fast ion storage kinetics of the adsorption mechanism on the cathode and co-intercalation mechanism on the anode, the full PIC exhibits a high energy density of 190 Wh kg^{-1} and a high power density of 21443 W kg^{-1}. In consideration of the low-cost graphite, graphite oxide, and electrolyte, the proposed PIC could be a priority prototype to be further improved with industrial-style engineering optimization. This work suggests a new idea of identifying electrolytes that can achieve enhanced high-rate performance for the carbon-based HICs. The proposed prototype may take a solid step for the commercialization application of PICs.

(3) New mechanism development for the ion storage of SIC anode:

The reduced graphite oxide nanosheets are utilized as the anode for SIC. The high rate capability of sodium-ion storage is achieved in DME electrolyte. It delivers a high capacity of 166 mAh g^{-1} at a current density of 20 A g^{-1}. The fast ion storage kinetics is demonstrated in DME electrolyte, which benefits the high rate of performance. Furthermore, the ion-storage mechanism investigations reveal that the ordered carbon layers in reduced graphite oxide can be efficiently utilized in DME electrolyte by co-intercalation of the Na^+-solvent complexes. The combination of the adsorption and co-intercalation mechanisms is totally different from the reported sodium-ion storage mechanisms of carbon materials anodes. Finally, a symmetric dual-carbon SIC is configurated by using the reduced graphite oxide as both anode and cathode. It exhibits a high electrochemical performance with a high energy density of 91 Wh kg^{-1} and a high power density of 10896 W kg^{-1}. This work proposed a new combination ion storage mechanism for sodium-ion storage in carbon materials. It may broaden the research field of carbon anode materials for SICs.

Based on the above three strategies, further research about carbon materials in PICs and SICs could focus on many other directions accordantly. First, increasing active sites of cation storage. As discussed in this dissertation, cation storage can be promoted by increasing oxygen functional groups. However, many other functional groups can store cation with high voltage windows. New functional groups need to be discovered to store cation for the carbon materials of PICs and SICs. Second, increasing active sites of anion storage. The anion storage generally occurs at a high voltage, giving a high energy density output. Exploring functional groups for

storing anions could be essential for improving the energy density of PICs and SICs. Third, investigating the role of electrolyte salt for dual-ion storage. In this dissertation, the influence of the electrolyte solvents is discussed for the dual-ion storage, but the electrolyte salt as another crucial component of electrolyte also needs to be studied. Last, optimizing the ordered and disordered carbon layer structures or discovering new carbon materials for better utilization of the new ion storage mechanism proposed in this dissertation.

8 Bibliography

[1] D. Larcher, J.M. Tarascon, Towards greener and more sustainable batteries for electrical energy storage, Nature Chemistry, 7 (2015) 19–29.

[2] N.S. Lewis, Powering the planet, MRS Bulletin, 32 (2007) 808–820.

[3] International energy agency key world energy statistics 2011 (IEA, 2011); available at http://www.iea.org/publications/freepublications/publication/key_world_energy_stats-1.pdf.

[4] Y.-H. Zhu, X. Yang, T. Sun, S. Wang, Y.-L. Zhao, J.-M. Yan, X.-B. Zhang, Recent progresses and prospects of cathode materials for non-aqueous potassium-ion batteries, Electrochemical Energy Reviews, 1 (2018) 548–566.

[5] C. Zhang, H. Zhao, Y. Lei, Recent research progress of anode materials for potassium-ion Batteries, Energy & Environmental Materials, 3 (2020) 105–120.

[6] C. Vaalma, D. Buchholz, M. Weil, S. Passerini, A cost and resource analysis of sodium-ion batteries, Nature Reviews Materials, 3 (2018) 1–11.

[7] Y. Liu, D. He, R. Han, G. Wei, Y. Qiao, Nanostructured potassium and sodium ion incorporated Prussian blue frameworks as cathode materials for sodium-ion batteries, Chemical Communications, 53 (2017) 5569–5572.

[8] J. Xu, S. Dou, X. Cui, W. Liu, Z. Zhang, Y. Deng, W. Hu, Y. Chen, Potassium-based electrochemical energy storage devices: Development status and future prospect, Energy Storage Materials, 34 (2021) 85–106.

[9] N. Yabuuchi, K. Kubota, M. Dahbi, S. Komaba, Research development on sodium-ion batteries, Chemical Reviews, 114 (2014) 11636–11682.

[10] H. Kim, J.C. Kim, M. Bianchini, D.-H. Seo, J. Rodriguez-Garcia, G. Ceder, Recent progress and perspective in electrode materials for K-ion batteries, Advanced Energy Materials, 8 (2018) 1702384.

[11] R. Rajagopalan, Y. Tang, X. Ji, C. Jia, H. Wang, Advancements and challenges in potassium ion batteries: A comprehensive review, Advanced Functional Materials, 30 (2020) 1909486.

[12] J.C. Pramudita, D. Sehrawat, D. Goonetilleke, N. Sharma, An initial review of the status of electrode materials for potassium-ion batteries, Advanced Energy Materials, 7 (2017) 1602911.

[13] A. Eftekhari, Z. Jian, X. Ji, Potassium secondary batteries, ACS Applied Materials & Interfaces, 9 (2017) 4404–4419.

[14] M. Liu, L. Chang, Z. Le, J. Jiang, J. Li, H. Wang, C. Zhao, T. Xu, P. Nie, L. Wang, Emerging potassium-ion hybrid capacitors, ChemSusChem, 13 (2020) 5837–5862.

[15] R. Verma, P.N. Didwal, J.Y. Hwang, C.J. Park, Recent progress in electrolyte development and design strategies for next-generation potassium-ion batteries, Batteries & Supercaps, 4 (2021) 1–24.

[16] J.-Y. Hwang, S.-T. Myung, Y.-K. Sun, Recent progress in rechargeable potassium batteries, Advanced Functional Materials, 28 (2018) 1802938.

[17] Y. Wang, P. Niu, J. Li, S. Wang, L. Li, Recent progress of phosphorus composite anodes for sodium/potassium ion batteries, Energy Storage Materials, 34 (2021) 436–460.

[18] M. Chen, E. Wang, Q. Liu, X. Guo, W. Chen, S.-L. Chou, S.-X. Dou, Recent progress on iron-and manganese-based anodes for sodium-ion and potassium-ion batteries, Energy Storage Materials, 19 (2019) 163–178.

[19] J. Chen, B. Yang, B. Liu, J. Lang, X. Yan, Recent advances in anode materials for sodium- and potassium-ion hybrid capacitors, Current Opinion in Electrochemistry, 18 (2019) 1–8.

[20] X. Wu, Y. Chen, Z. Xing, C.W.K. Lam, S.S. Pang, W. Zhang, Z. Ju, Advanced carbon-based anodes for potassium-ion batteries, Advanced Energy Materials, 9 (2019) 1900343.

[21] H. Hou, X. Qiu, W. Wei, Y. Zhang, X. Ji, Carbon anode materials for advanced sodium-ion batteries, Advanced Energy Materials, 7 (2017) 1602898.

[22] N.S. Choi, Z. Chen, S.A. Freunberger, X. Ji, Y.K. Sun, K. Amine, G. Yushin, L.F. Nazar, J. Cho, P.G. Bruce, Challenges facing lithium batteries and electrical double-layer capacitors, Angewandte Chemie International Edition, 51 (2012) 9994–10024.

[23] W. Raza, F. Ali, N. Raza, Y. Luo, K.-H. Kim, J. Yang, S. Kumar, A. Mehmood, E.E. Kwon, Recent advancements in supercapacitor technology, Nano Energy, 52 (2018) 441–473.

[24] D. Lin, Y. Liu, Y. Cui, Reviving the lithium metal anode for high-energy batteries, Nature Nanotechnology, 12 (2017) 194–206.

[25] J.R. Miller, P. Simon, Electrochemical capacitors for energy management, Science, 321 (2008) 651–652.

[26] P. Simon, Y. Gogotsi, Materials for electrochemical capacitors, Nanoscience and Technology: A Collection of Reviews from Nature Journals, (2010) 320–329.

[27] P. Simon, Y. Gogotsi, B. Dunn, Where do batteries end and supercapacitors begin?, Science, 343 (2014) 1210–1211.

[28] M. Winter, R.J. Brodd, What are batteries, fuel cells, and supercapacitors?, Chemical Reviews, 104 (2004) 4245–4270.

[29] T. Nagaura, Development of rechargeable lithium batteries, JRC Battery Newsletter, (1991) 10–18.

[30] Y. Ding, Z.P. Cano, A. Yu, J. Lu, Z. Chen, Automotive Li-ion batteries: current status and future perspectives, Electrochemical Energy Reviews, 2 (2019) 1–28.

[31] J. Ding, W. Hu, E. Paek, D. Mitlin, Review of hybrid ion capacitors: From aqueous to lithium to sodium, Chemical Reviews, 118 (2018) 6457–6498.

[32] B.E. Conway, Electrochemical supercapacitors: scientific fundamentals and technological applications, Springer Science & Business Media, 2013.

[33] W. Zuo, R. Li, C. Zhou, Y. Li, J. Xia, J. Liu, Battery-supercapacitor hybrid devices: recent progress and future prospects, Advanced Science, 4 (2017) 1600539.

[34] D.P. Dubal, O. Ayyad, V. Ruiz, P. Gomez-Romero, Hybrid energy storage: the merging of battery and supercapacitor chemistries, Chemical Society Reviews, 44 (2015) 1777–1790.

[35] J. Cao, A. Emadi, A new battery/ultracapacitor hybrid energy storage system for electric, hybrid, and plug-in hybrid electric vehicles, IEEE Transactions on Power Electronics, 27 (2011) 122-132.

[36] V. Aravindan, J. Gnanaraj, Y.-S. Lee, S. Madhavi, Insertion-type electrodes for nonaqueous Li-ion capacitors, Chemical Reviews, 114 (2014) 11619–11635.

[37] A. Muzaffar, M.B. Ahamed, K. Deshmukh, J. Thirumalai, A review on recent advances in hybrid supercapacitors: Design, fabrication and applications, Renewable and Sustainable Energy Reviews, 101 (2019) 123–145.

[38] A. González, E. Goikolea, J.A. Barrena, R. Mysyk, Review on supercapacitors: Technologies and materials, Renewable and Sustainable Energy Reviews, 58 (2016) 1189–1206.

[39] Y. Firouz, N. Omar, J.-M. Timmermans, P. Van Den Bossche, J. Van Mierlo, Lithium-ion capacitor–Characterization and development of new electrical model, Energy, 83 (2015) 597–613.

[40] R. Jia, G. Shen, D. Chen, Recent progress and future prospects of sodium-ion capacitors, Science China Materials, 63 (2020) 185–206.

[41] M. Soltani, S.H. Beheshti, A comprehensive review of lithium ion capacitor: development, modelling, thermal management and applications, Journal of Energy Storage, (2020) 102019.

[42] T. Nakayama, W. Tachihara, M. Toda, M. Ishida, H. Hasegawa, K. Hiraoka, N. Kakizaki, Improvement of converter efficiency in partial load using temporary storage with lithium-ion capacitor, 2014 49th International Universities Power Engineering Conference (UPEC), IEEE, (2014) 1–6.

[43] Z. Chen, D. Boroyevich, R. Burgos, F. Wang, Characterization and modeling of 1.2 kv, 20 A SiC MOSFETs, 2009 IEEE Energy Conversion Congress and Exposition, IEEE, (2009) 1480–1487.

[44] S. Lambert, V. Pickert, J. Holden, X. He, W. Li, Comparison of supercapacitor and lithium-ion capacitor technologies for power electronics applications, 5th IET International Conference on Power Electronics, Machines and Drives (PEMD 2010), IET, (2010) 1–5.

[45] R.B. Sepe, A. Steyerl, S.P. Bastien, Lithium-ion supercapacitors for pulsed power applications, 2011 IEEE Energy Conversion Congress and Exposition, IEEE, (2011) 1813–1818.

[46] F. Ciccarelli, A. Del Pizzo, D. Iannuzzi, Improvement of energy efficiency in light railway vehicles based on power management control of wayside lithium-ion capacitor storage, IEEE Transactions on Power Electronics, 29 (2013) 275–286.

[47] M. Soltani, J. Ronsmans, S. Kakihara, J. Jaguemont, P. Van den Bossche, J. Van Mierlo, N. Omar, Hybrid battery/lithium-ion capacitor energy storage system for a pure electric bus for an urban transportation application, Applied Sciences, 8 (2018) 1176.

[48] M. Uno, K. Tanaka, Spacecraft electrical power system using lithium-ion capacitors, IEEE Transactions on Aerospace and Electronic Systems, 49 (2013) 175–188.

[49] M. Uno, A. Kukita, Cycle life evaluation based on accelerated aging testing for lithium-ion capacitors as alternative to rechargeable batteries, IEEE Transactions on Industrial Electronics, 63 (2015) 1607–1617.

[50] F. Jonas, L. Schrader, Conductive modifications of polymers with polypyrroles and polythiophenes, Synthetic Metals, 41 (1991) 831–836.

[51] G.G. Amatucci, F. Badway, A. Du Pasquier, T. Zheng, An asymmetric hybrid nonaqueous energy storage cell, Journal of the Electrochemical Society, 148 (2001) A930.

[52] A. Jagadale, X. Zhou, R. Xiong, D.P. Dubal, J. Xu, S. Yang, Lithium ion capacitors (LICs): Development of the materials, Energy Storage Materials, 19 (2019) 314–329.

[53] C. Han, H. Li, R. Shi, L. Xu, J. Li, F. Kang, B. Li, Nanostructured anode materials for non-aqueous lithium ion hybrid capacitors, Energy & Environmental Materials, 1 (2018) 75-87.

[54] B. Li, J. Zheng, H. Zhang, L. Jin, D. Yang, H. Lv, C. Shen, A. Shellikeri, Y. Zheng, R. Gong, Electrode materials, electrolytes, and challenges in nonaqueous lithium-ion capacitors, Advanced Materials, 30 (2018) 1705670.

[55] K. Turcheniuk, D. Bondarev, V. Singhal, G. Yushin, Ten years left to redesign lithium-ion batteries, Nature, 559 (2018) 467–470.

[56] D. Kundu, E. Talaie, V. Duffort, L.F. Nazar, The emerging chemistry of sodium ion batteries for electrochemical energy storage, Angewandte Chemie International Edition, 54 (2015) 3431–3448.

[57] H. Wang, C. Zhu, D. Chao, Q. Yan, H.J. Fan, Nonaqueous hybrid lithium-ion and sodium-ion capacitors, Advanced Materials, 29 (2017) 1702093.

[58] J. Yuan, X. Hu, Y. Liu, G. Zhong, B. Yu, Z. Wen, Recent progress in sodium/potassium hybrid capacitors, Chemical Communications, 56 (2020) 13933–13949.

[59] Y. Zhang, J. Jiang, Y. An, L. Wu, H. Dou, J. Zhang, Y. Zhang, S. Wu, X. Zhang, M. Dong, Sodium ion capacitors: materials, mechanism and challenges, ChemSusChem, 13 (2020) 2522–2539.

[60] Y. Xu, M. Zhou, Y. Lei, Nanoarchitectured array electrodes for rechargeable lithium- and sodium-ion batteries, Advanced Energy Materials, 6 (2016) 1502514.

[61] M.D. Slater, D. Kim, E. Lee, C.S. Johnson, Sodium-ion batteries, Advanced Functional Materials, 23 (2013) 947-958.

[62] S.W. Kim, D.H. Seo, X. Ma, G. Ceder, K. Kang, Electrode materials for rechargeable sodium-ion batteries: potential alternatives to current lithium-ion batteries, Advanced Energy Materials, 2 (2012) 710–721.

[63] Z. Chen, V. Augustyn, X. Jia, Q. Xiao, B. Dunn, Y. Lu, High-performance sodium-ion pseudocapacitors based on hierarchically porous nanowire composites, ACS Nano, 6 (2012) 4319-4327.

[64] Z. Jian, W. Luo, X. Ji, Carbon electrodes for K-ion batteries, Journal of the Amercian Chemical Society, 137 (2015) 11566–11569.

[65] A.P. Cohn, N. Muralidharan, R. Carter, K. Share, L. Oakes, C.L. Pint, Durable potassium ion battery electrodes from high-rate cointercalation into graphitic carbons, Journal of Materials Chemistry A, 4 (2016) 14954–14959.

[66] S. Komaba, T. Hasegawa, M. Dahbi, K. Kubota, Potassium intercalation into graphite to realize high-voltage/high-power potassium-ion batteries and potassium-ion capacitors, Electrochemistry Communications, 60 (2015) 172–175.

[67] Y.N. Chen, W. Luo, M. Carter, L.H. Zhou, J.Q. Dai, K. Fu, S.Lacey, T.Li, J.Y. Wan, X.G. Han, Y.P. Bao, L.B. Hu, Organic electrode for non-aqueous potassium-ion batteries, Nano Energy, 18 (2015) 205–211.

[68] A. Le Comte, Y. Reynier, C. Vincens, C. Leys, P. Azaïs, First prototypes of hybrid potassium-ion capacitor (KIC): An innovative, cost-effective energy storage technology for transportation applications, Journal of Power Sources, 363 (2017) 34–43.

[69] P. Cai, K. Zou, X. Deng, B. Wang, M. Zheng, L. Li, H. Hou, G. Zou, X. Ji, Comprehensive understanding of sodium-Ion capacitors: Definition, mechanisms, configurations, materials, key technologies, and future developments, Advanced Energy Materials, 11 (2021) 2003804.

[70] G. Li, Z. Yang, Z. Yin, H. Guo, Z. Wang, G. Yan, Y. Liu, L. Li, J. Wang, Non-aqueous dual-carbon lithium-ion capacitors: a review, Journal of Materials Chemistry A, 7 (2019) 15541–15563.

[71] X. Deng, K. Zou, P. Cai, B. Wang, H. Hou, G. Zou, X. Ji, Advanced battery-type anode materials for high-performance sodium-ion capacitors, Small Methods, 4 (2020) 2000401.

[72] J. Kim, M.S. Choi, K.H. Shin, M. Kota, Y. Kang, S. Lee, J.Y. Lee, H.S. Park, Rational design of carbon nanomaterials for electrochemical sodium storage and capture, Advanced Materials, 31 (2019) 1803444.

[73] B. Wang, X. Gao, L. Xu, K. Zou, P. Cai, X. Deng, L. Yang, H. Hou, G. Zou, X. Ji, Advanced carbon materials for sodium-ion capacitors, Batteries & Supercaps, 4 (2021) 538–553.

[74] S. Natarajan, Y.S. Lee, V. Aravindan, Biomass-derived carbon materials as prospective electrodes for high-energy lithium-and sodium-ion capacitors, Chemistry–An Asian Journal, 14 (2019) 936–951.

[75] J. Ruan, F. Mo, Z. Chen, M. Liu, S. Zheng, R. Wu, F. Fang, Y. Song, D. Sun, Rational construction of nitrogen-doped hierarchical dual-carbon for advanced potassium-ion hybrid capacitors, Advanced Energy Materials, 10 (2020) 1904045.

[76] J. Zhao, X.X. Zou Y.J. Zhu, Y.H. Xu, C.S. Wang, Electrochemical intercalation of potassium into graphite, Advanced Functional Materials, 26 (2016) 8103–8110.

[77] Y. Wen, K. He, Y. Zhu, F. Han, Y. Xu, I. Matsuda, Y. Ishii, J. Cumings, C. Wang, Expanded graphite as superior anode for sodium-ion batteries, Nature Communications, 5 (2014) 4033.

[78] Z. Xing, Y. Qi, Z. Jian, X. Ji, Polynanocrystalline graphite: A new carbon anode with superior cycling performance for K-ion batteries, ACS Applied Materials & Interfaces, 9 (2017) 4343–4351.

[79] K. Share, A.P. Cohn, R. Carter, B. Rogers, C.L. Pint, Role of nitrogen doped graphene for improved high capacity potassium ion battery anodes, ACS Nano, 10 (2016) 9738–9744.

[80] W. Luo, J. Wan, B. Ozdemir, W. Bao, Y. Chen, J. Dai, H. Lin, Y. Xu, F. Gu, V. Barone, L. Hu, Potassium ion batteries with graphitic materials, Nano Letters, 15 (2015) 7671–7677.

[81] L. Li, L. Liu, Z. Hu, Y. Lu, Q. Liu, S. Jin, Q. Zhang, S. Zhao, S.L. Chou, Understanding high-rate K(+)-solvent co-intercalation in natural graphite for potassium-ion batteries, Angewandte Chemie International Edition, 59 (2020) 12917–12924.

[82] H. Kim, J. Hong, G. Yoon, H. Kim, K.-Y. Park, M.-S. Park, W.-S. Yoon, K. Kang, Sodium intercalation chemistry in graphite, Energy & Environmental Science, 8 (2015) 2963–2969.

[83] B. Cao, Q. Zhang, H. Liu, B. Xu, S.L. Zhang, T.F. Zhou, J.F. Mao,W.K. Pang, Z.P. Guo, A. Li, J.S. Zhou, X.H. Chen, H.H. Song, Graphitic carbon nanocage as a stable and high power anode for potassium-ion batteries, Advanced Energy Materials, 8 (2018) 1801149.

[84] B. Jache, P. Adelhelm, Use of graphite as a highly reversible electrode with superior cycle life for sodium-ion batteries by making use of co-intercalation phenomena, Angewandte Chemie International Edition, 126 (2014) 10333–10337.

[85] Z.-L. Xu, G. Yoon, K.-Y. Park, H. Park, O. Tamwattana, S.J. Kim, W.M. Seong, K. Kang, Tailoring sodium intercalation in graphite for high energy and power sodium ion batteries, Nature Communications, 10 (2019) 1–10.

[86] L. Fan, K. Lin, J. Wang, R. Ma, B. Lu, A nonaqueous potassium-based battery-supercapacitor hybrid device, Advanced Materials, 30 (2018) 1800804.

[87] S. Chen, J. Wang, L. Fan, R. Ma, E. Zhang, Q. Liu, B. Lu, An ultrafast rechargeable hybrid sodium-based dual-ion capacitor based on hard carbon cathodes, Advanced Energy Materials, 8 (2018) 1800140.

[88] Z. Xu, M. Wu, Z. Chen, C. Chen, J. Yang, T. Feng, E. Paek, D. Mitlin, Direct structure-performance comparison of all-carbon potassium and sodium ion capacitors, Advanced Science, 6 (2019) 1802272.

[89] H.-J. Kang, Y.S. Huh, W.B. Im, Y.-S. Jun, Molecular cooperative assembly-mediated synthesis of ultra-high-performance hard carbon anodes for dual-carbon sodium hybrid capacitors, ACS Nano, 13 (2019) 11935–11946.

[90] J. Chen, B. Yang, H. Li, P. Ma, J. Lang, X. Yan, Candle soot: onion-like carbon, an advanced anode material for a potassium-ion hybrid capacitor, Journal of Materials Chemistry A, 7 (2019) 9247–9252.

[91] Y. Liu, Q. Ru, Y. Gao, Q. An, F. Chen, Z. Shi, M. Zheng, Z. Pan, Constructing volcanic-like mesoporous hard carbon with fast electrochemical kinetics for potassium-ion batteries and hybrid capacitors, Applied Surface Science, 525 (2020) 146563.

[92] H. Luo, M. Chen, J. Cao, M. Zhang, S. Tan, L. Wang, J. Zhong, H. Deng, J. Zhu, B. Lu, Cocoon silk-derived, hierarchically porous carbon as anode for highly robust potassium-ion hybrid capacitors, Nano-Micro Letters, 12 (2020) 1–13.

[93] P. Wang, Z. Gong, K. Ye, Y. Gao, K. Zhu, J. Yan, G. Wang, D. Cao, N-rich biomass carbon derived from hemp as a full carbon-based potassium ion hybrid capacitor anode, Applied Surface Science, 553 (2021) 149569.

[94] F. Huang, W. Liu, Q. Wang, F. Wang, Q. Yao, D. Yan, H. Xu, B.Y. Xia, J. Deng, Natural N/O-doped hard carbon for high performance K-ion hybrid capacitors, Electrochimica Acta, 354 (2020) 136701.

[95] J. Zhu, J. Roscow, S. Chandrasekaran, L. Deng, P. Zhang, T. He, K. Wang, L. Huang, Biomass-derived carbons for sodium-ion batteries and sodium-ion capacitors, ChemSusChem, 13 (2020) 1275–1295.

[96] A. Kamiyama, K. Kubota, T. Nakano, S. Fujimura, S. Shiraishi, H. Tsukada, S. Komaba, High-capacity hard carbon synthesized from macroporous phenolic resin for sodium-ion and potassium-ion battery, ACS Applied Energy Materials, 3 (2019) 135–140.

[97] Y. Shen, C. Huang, Y. Li, Y. Zhou, Y. Xu, Y. Zhang, A. Hu, Q. Tang, X. Song, C. Jiang, Enhanced sodium and potassium ions storage of soft carbon by a S/O co-doped strategy, Electrochimica Acta, 367 (2021) 137526.

[98] J. Xu, Z. Liu, F. Zhang, J. Tao, L. Shen, X. Zhang, Bacterial cellulose-derived carbon nanofibers as both anode and cathode for hybrid sodium ion capacitor, RSC Advances, 10 (2020) 7780–7790.

[99] J. Ding, Z. Li, K. Cui, S. Boyer, D. Karpuzov, D. Mitlin, Heteroatom enhanced sodium ion capacity and rate capability in a hydrogel derived carbon give record performance in a hybrid ion capacitor, Nano Energy, 23 (2016) 129–137.

[100] K. Liao, H. Wang, L. Wang, D. Xu, M. Wu, R. Wang, B. He, Y. Gong, X. Hu, A high-energy sodium-ion capacitor enabled by a nitrogen/sulfur co-doped hollow carbon nanofiber anode and an activated carbon cathode, Nanoscale Advances, 1 (2019) 746–756.

[101] H. Jin, X. Feng, J. Li, M. Li, Y. Xia, Y. Yuan, C. Yang, B. Dai, Z. Lin, J. Wang, Heteroatom-doped porous carbon materials with unprecedented high volumetric capacitive performance, Angewandte Chemie International Edition, 131 (2019) 2419–2423.

[102] H.D. Pham, J.F. Fernando, M. Horn, J. MacLeod, N. Motta, B. Doherty, A. Payne, A.K. Nanjundan, D. Golberg, D. Dubal, Multi-heteroatom doped nanocarbons for high performance double carbon potassium ion capacitor, Electrochimica Acta, 389 (2021) 138717.

[103] J. Li, X. Hu, G. Zhong, Y. Liu, Y. Ji, J. Chen, Z. Wen, A general self-sacrifice template strategy to 3D heteroatom-doped macroporous carbon for high-performance potassium-ion hybrid capacitors, Nano-Micro Letters, 13 (2021) 1–15.

[104] Y. Yi, H. Ma, X. Lian, Q. Mei, Z. Zeng, Y. Zhao, C. Lu, W. Zhao, W. Guo, Z. Liu, Harmonized edge/graphitic-nitrogen doped carbon nanopolyhedron@nanosheet

composite via salt-confined strategy for advanced K-ion hybrid capacitors, InfoMat, 3 (2021) 891–903.

[105] C. Wang, F. Wang, Z. Liu, Y. Zhao, Y. Liu, Q. Yue, H. Zhu, Y. Deng, Y. Wu, D. Zhao, N-doped carbon hollow microspheres for metal-free quasi-solid-state full sodium-ion capacitors, Nano Energy, 41 (2017) 674–680.

[106] G. Zhong, S. Lei, X. Hu, Y. Ji, Y. Liu, J. Yuan, J. Li, H. Zhan, Z. Wen, Facile synthesis of P-doped carbon nanosheets as janus electrodes of advanced potassium-ion hybrid capacitor, ACS Applied Materials & Interfaces, 13 (2021) 29511–29821.

[107] C. Yang, M. Zhang, N. Kong, J. Lan, Y. Yu, X. Yang, Self-supported carbon nanofiber films with high-level nitrogen and phosphorus co-doping for advanced lithium-ion and sodium-ion capacitors, ACS Sustainable Chemistry & Engineering, 7 (2019) 9291–9300.

[108] Q. Yu, T. Dong, R. Qiu, H. Wang, Sulfur and nitrogen dual-doped carbon nanofiber with enlarged interlayer distance as a superior anode material for sodium-ion capacitors, Materials Research Bulletin, 138 (2021) 111211.

[109] B. Yang, J. Chen, S. Lei, R. Guo, H. Li, S. Shi, X. Yan, Spontaneous growth of 3D framework carbon from sodium citrate for high energy-and power-density and long-life sodium-ion hybrid capacitors, Advanced Energy Materials, 8 (2018) 1702409.

[110] K. Wang, N. Wang, J. He, Z. Yang, X. Shen, C. Huang, Preparation of 3D architecture graphdiyne nanosheets for high-performance sodium-ion batteries and capacitors, ACS Applied Materials & Interfaces, 9 (2017) 40604–40613.

[111] B. Yang, J. Chen, L. Liu, P. Ma, B. Liu, J. Lang, Y. Tang, X. Yan, 3D nitrogen-doped framework carbon for high-performance potassium ion hybrid capacitor, Energy Storage Materials, 23 (2019) 522–529.

[112] F. Sun, X. Liu, H.B. Wu, L. Wang, J. Gao, H. Li, Y. Lu, In situ high-level nitrogen doping into carbon nanospheres and boosting of capacitive charge storage in both anode and cathode for a high-energy 4.5 V full-carbon lithium-ion capacitor, Nano Letters, 18 (2018) 3368–3376.

[113] R. Thangavel, A.G. Kannan, R. Ponraj, G. Yoon, V. Aravindan, D.-W. Kim, K. Kang, W.-S. Yoon, Y.-S. Lee, Surface enriched graphene hollow spheres towards building ultra-high power sodium-ion capacitor with long durability, Energy Storage Materials, 25 (2020) 702–713.

[114] X. Li, M. Chen, L. Wang, H. Xu, J. Zhong, M. Zhang, Y. Wang, Q. Zhang, L. Mei, T. Wang, Nitrogen-doped carbon nanotubes as an anode for a highly robust potassium-ion hybrid capacitor, Nanoscale Horizons, 5 (2020) 1586–1595.

[115] D. Li, C. Ye, X. Chen, S. Wang, H. Wang, A high energy and power sodium-ion hybrid capacitor based on nitrogen-doped hollow carbon nanowires anode, Journal of Power Sources, 382 (2018) 116–121.

[116] H. Wang, D. Mitlin, J. Ding, Z. Li, K. Cui, Excellent energy–power characteristics from a hybrid sodium ion capacitor based on identical carbon nanosheets in both electrodes, Journal of Materials Chemistry A, 4 (2016) 5149–5158.

[117] C. Cui, H. Wang, M. Wang, X. Ou, Z. Wei, J. Ma, Y. Tang, Hollow carbon nanobelts codoped with nitrogen and sulfur via a self-templated method for a high-performance sodium-ion capacitor, Small, 15 (2019) 1902659.

[118] F. Hu, S. Liu, S. Li, C. Liu, G. Yu, C. Song, W. Shao, T. Zhang, X. Jian, High and ultra-stable energy storage from all-carbon sodium-ion capacitor with 3D framework carbon as cathode and carbon nanosheet as anode, Journal of Energy Chemistry, 55 (2021) 304–312.

[119] X. Hu, G. Zhong, J. Li, Y. Liu, J. Yuan, J. Chen, H. Zhan, Z. Wen, Hierarchical porous carbon nanofibers for compatible anode and cathode of potassium-ion hybrid capacitor, Energy & Environmental Science, 13 (2020) 2431–2440.

[120] S. Liu, Z. Cai, J. Zhou, A. Pan, S. Liang, Nitrogen-doped TiO_2 nanospheres for advanced sodium-ion battery and sodium-ion capacitor applications, Journal of Materials Chemistry A, 4 (2016) 18278-18283.

[121] Z. Le, F. Liu, P. Nie, X. Li, X. Liu, Z. Bian, G. Chen, H.B. Wu, Y. Lu, Pseudocapacitive sodium storage in mesoporous single-crystal-like TiO_2–graphene nanocomposite enables high-performance sodium-ion capacitors, ACS Nano, 11 (2017) 2952–2960.

[122] S. Liu, Z. Luo, G. Tian, M. Zhu, Z. Cai, A. Pan, S. Liang, TiO_2 nanorods grown on carbon fiber cloth as binder-free electrode for sodium-ion batteries and flexible sodium-ion capacitors, Journal of Power Sources, 363 (2017) 284–290.

[123] Y.E. Zhu, L. Yang, J. Sheng, Y. Chen, H. Gu, J. Wei, Z. Zhou, Fast sodium storage in TiO_2@CNT@C nanorods for high-performance Na-ion capacitors, Advanced Energy Materials, 7 (2017) 1701222.

[124] L.F. Que, F.D. Yu, Z.B. Wang, D.M. Gu, Pseudocapacitance of TiO_2−x/CNT anodes for high-performance quasi-solid-state Li-ion and Na-ion capacitors, Small, 14 (2018) 1704508.

[125] S. Luo, T. Yuan, L. Soule, J. Ruan, Y. Zhao, D. Sun, J. Yang, M. Liu, S. Zheng, Enhanced ionic/electronic transport in nano-TiO_2/sheared CNT composite electrode for Na^+ insertion-based hybrid ion-capacitors, Advanced Functional Materials, 30 (2020) 1908309.

[126] W. Feng, R.R. Maça, V. Etacheri, High-energy-density sodium-ion hybrid capacitors enabled by interface-engineered hierarchical TiO_2 nanosheet anodes, ACS Applied Materials & Interfaces, 12 (2020) 4443–4453.

[127] G. Wang, Y. Li, Y. Liu, S. Jiao, B. Peng, J. Li, L. Yu, G. Zhang, Nest-like TiO_2-nitrogen-doped-carbon hybrid nanostructures as superior host for potassium-ion hybrid capacitors, Chemical Engineering Journal, 417 (2021) 127977.

[128] H. Li, J. Chen, L. Zhang, K. Wang, X. Zhang, B. Yang, L. Liu, W. Liu, X. Yan, A metal–organic framework-derived pseudocapacitive titanium oxide/carbon core/shell heterostructure for high performance potassium ion hybrid capacitors, Journal of Materials Chemistry A, 8 (2020) 16302–16311.

[129] S. Dong, L. Shen, H. Li, G. Pang, H. Dou, X. Zhang, Flexible sodium-ion pseudocapacitors based on 3D $Na_2Ti_3O_7$ nanosheet arrays/carbon textiles anodes, Advanced Functional Materials, 26 (2016) 3703–3710.

[130] S.S. Bhat, B. Babu, M. Feygenson, J.C. Neuefeind, M. Shaijumon, Nanostructured $Na_2Ti_9O_{19}$ for hybrid sodium-ion capacitors with excellent rate capability, ACS Applied Materials & Interfaces, 10 (2018) 437–447.

[131] B. Babu, M. Shaijumon, High performance sodium-ion hybrid capacitor based on $Na_2Ti_2O_4(OH)_2$ nanostructures, Journal of Power Sources, 353 (2017) 85–94.

[132] S. Zhao, L. Dong, B. Sun, K. Yan, J. Zhang, S. Wan, F. He, P. Munroe, P.H. Notten, G. Wang, $K_2Ti_2O_5$@C Microspheres with enhanced K^+ intercalation pseudocapacitance ensuring fast potassium storage and long-term cycling stability, Small, 16 (2020) 1906131.

[133] S. Dong, Z. Li, Z. Xing, X. Wu, X. Ji, X. Zhang, Novel potassium-ion hybrid capacitor based on an anode of $K_2Ti_6O_{13}$ microscaffolds, ACS Applied Materials & Interfaces, 10 (2018) 15542–15547.

[134] Z. Zhang, M. Li, Y. Gao, Z. Wei, M. Zhang, C. Wang, Y. Zeng, B. Zou, G. Chen, F. Du, Fast potassium storage in hierarchical $Ca_{0.5}Ti_2(PO_4)_3$@C microspheres enabling high-performance potassium-ion capacitors, Advanced Functional Materials, 28 (2018) 1802684.

[135] S. Zhang, Y. Liu, Q. Han, S. He, N. Zhang, J. Yang, Development and characterization of aqueous sodium-ion hybrid supercapacitor based on $NaTi_2(PO_4)_3$//activated carbon, Journal of Alloys and Compounds, 729 (2017) 850–857.

[136] T. Wei, G. Yang, C. Wang, Iso-oriented $NaTi_2(PO_4)_3$ mesocrystals as anode material for high-energy and long-durability sodium-ion capacitor, ACS Applied Materials & Interfaces, 9 (2017) 31861–31870.

[137] Q. Yang, S. Cui, Y. Ge, Z. Tang, Z. Liu, H. Li, N. Li, H. Zhang, J. Liang, C. Zhi, Porous single-crystal $NaTi_2(PO_4)_3$ via liquid transformation of TiO_2 nanosheets for flexible aqueous Na-ion capacitor, Nano Energy, 50 (2018) 623–631.

[138] E. Lim, H. Kim, C. Jo, J. Chun, K. Ku, S. Kim, H.I. Lee, I.-S. Nam, S. Yoon, K. Kang, Advanced hybrid supercapacitor based on a mesoporous niobium pentoxide/carbon as high-performance anode, ACS Nano, 8 (2014) 8968–8978.

[139] Z. Tong, S. Liu, Y. Zhou, J. Zhao, Y. Wu, Y. Wang, Y. Li, Rapid redox kinetics in uniform sandwich-structured mesoporous Nb_2O_5/graphene/mesoporous Nb_2O_5 nanosheets for high-performance sodium-ion supercapacitors, Energy Storage Materials, 13 (2018) 223–232.

[140] Y. Li, H. Wang, L. Wang, Z. Mao, R. Wang, B. He, Y. Gong, X. Hu, Mesopore-induced ultrafast Na^+-storage in T-Nb_2O_5/carbon nanofiber films toward flexible high-power Na-ion capacitors, Small, 15 (2019) 1804539.

[141] X. Wang, Q. Li, L. Zhang, Z. Hu, L. Yu, T. Jiang, C. Lu, C. Yan, J. Sun, Z. Liu, Caging Nb_2O_5 nanowires in PECVD-derived graphene capsules toward bendable sodium-ion hybrid supercapacitors, Advanced Materials, 30 (2018) 1800963.

[142] E. Lim, C. Jo, M.S. Kim, M.H. Kim, J. Chun, H. Kim, J. Park, K.C. Roh, K. Kang, S. Yoon, High-performance sodium-ion hybrid supercapacitor based on Nb_2O_5@ carbon core–shell nanoparticles and reduced graphene oxide nanocomposites, Advanced Functional Materials, 26 (2016) 3711–3719.

[143] J. Dong, Y. Jiang, Q. Wei, S. Tan, Y. Xu, G. Zhang, X. Liao, W. Yang, Q. Li, Q. An, Strongly coupled pyridine-$V_2O_5 \cdot nH_2O$ nanowires with intercalation pseudocapacitance and stabilized layer for high energy sodium ion capacitors, Small, 15 (2019) 1900379.

[144] R. Kiruthiga, C. Nithya, R. Karvembu, Reduced graphene oxide embedded V_2O_5 nanorods and porous honey carbon as high performance electrodes for hybrid sodium-ion supercapacitors, Electrochimica Acta, 256 (2017) 221–231.

[145] Y. Wang, D. Kong, W. Shi, B. Liu, G.J. Sim, Q. Ge, H.Y. Yang, Ice templated free-standing hierarchically WS_2/CNT-rGO aerogel for high-performance rechargeable lithium and sodium ion batteries, Advanced Energy Materials, 6 (2016) 1601057.

[146] Y. Xiao, D. Su, X. Wang, S. Wu, L. Zhou, Y. Shi, S. Fang, H.M. Cheng, F. Li, CuS microspheres with tunable interlayer space and micropore as a high-rate and long-life anode for sodium-ion batteries, Advanced Energy Materials, 8 (2018) 1800930.

[147] H. Huang, J. Cui, G. Liu, R. Bi, L. Zhang, Carbon-coated $MoSe_2$/MXene hybrid nanosheets for superior potassium storage, ACS Nano, 13 (2019) 3448–3456.

[148] H. Dong, Y. Xu, C. Zhang, Y. Wu, M. Zhou, L. Liu, Y. Dong, Q. Fu, M. Wu, Y. Lei, MoS_2 nanosheets with expanded interlayer spacing for enhanced sodium storage, Inorganic Chemistry Frontiers, 5 (2018) 3099–3105.

[149] X. Ren, Q. Zhao, W.D. McCulloch, Y. Wu, MoS_2 as a long-life host material for potassium ion intercalation, Nano Research, 10 (2017) 1313–1321.

[150] X. Hu, Y. Liu, J. Chen, J. Jia, H. Zhan, Z. Wen, FeS quantum dots embedded in 3D ordered macroporous carbon nanocomposite for high-performance sodium-ion hybrid capacitors, Journal of Materials Chemistry A, 7 (2019) 1138–1148.

[151] J. Ge, B. Wang, J. Wang, Q. Zhang, B. Lu, Nature of $FeSe_2$/N-C anode for high performance potassium ion hybrid capacitor, Advanced Energy Materials, 10 (2020) 1903277.

[152] Y. Yi, Z. Sun, C. Li, Z. Tian, C. Lu, Y. Shao, J. Li, J. Sun, Z. Liu, Designing 3D biomorphic nitrogen-doped $MoSe_2$/graphene composites toward high-performance potassium-ion capacitors, Advanced Functional Materials, 30 (2020) 1903878.

[153] K. Li, X. Liu, Y. Qin, Z. Zhao, Y. Xu, Y. Yi, H. Guan, Y. Fu, P. Liu, D. Li, Sb_2S_3-Bi_2S_3 microrods with the combined action of carbon encapsulation and rGO confinement for improving high cycle stability in sodium/potassium storage, Chemical Engineering Journal, 414 (2021) 128787.

[154] D. Li, J. Zhou, X. Chen, H. Song, Graphene-loaded Bi_2Se_3: A conversion-alloying-type anode material for ultrafast gravimetric and volumetric Na storage, ACS Applied Materials & Interfaces, 10 (2018) 30379–30387.

[155] J. Cui, S. Yao, Z. Lu, J.Q. Huang, W.G. Chong, F. Ciucci, J.K. Kim, Revealing pseudocapacitive mechanisms of metal dichalcogenide SnS_2/graphene-CNT aerogels for high-energy Na hybrid capacitors, Advanced Energy Materials, 8 (2018) 1702488.

[156] J. Chen, B. Yang, H. Hou, H. Li, L. Liu, L. Zhang, X. Yan, Disordered, Large interlayer spacing, and oxygen-rich carbon nanosheets for potassium ion hybrid capacitor, Advanced Energy Materials, 9 (2019) 1803894.

[157] J. Niu, J. Guan, M. Dou, Z. Zhang, J. Kong, F. Wang, Sustainable synthesis of biomass-derived carbon electrodes with hybrid energy-storage behaviors for use in high-performance Na-Ion capacitors, ACS Applied Energy Materials, 3 (2020) 2478–2489.

[158] S. Wang, R. Wang, Y. Zhang, L. Zhang, Highly porous carbon with large electrochemical ion absorption capability for high-performance supercapacitors and ion capacitors, Nanotechnology, 28 (2017) 445406.

[159] J. Ajuria, E. Redondo, M. Arnaiz, R. Mysyk, T. Rojo, E. Goikolea, Lithium and sodium ion capacitors with high energy and power densities based on carbons from recycled olive pits, Journal of Power Sources, 359 (2017) 17–26.

[160] H. Li, J. Lang, S. Lei, J. Chen, K. Wang, L. Liu, T. Zhang, W. Liu, X. Yan, A high-performance sodium-ion hybrid capacitor constructed by metal–organic framework–derived anode and cathode materials, Advanced Functional Materials, 28 (2018) 1800757.

[161] Q. Zhao, D. Yang, A.K. Whittaker, X. Zhao, A hybrid sodium-ion capacitor with polyimide as anode and polyimide-derived carbon as cathode, Journal of Power Sources, 396 (2018) 12–18.

[162] B. He, A.-H. Lu, F. Cheng, X.-F. Yu, D. Yan, W.-C. Li, Fabrication of high-energy hybrid capacitors by using carbon-sulfur composite as promising cathodes, Journal of Power Sources, 396 (2018) 102–108.

[163] H. Zhang, M. Hu, Q. Lv, Z.H. Huang, F. Kang, R. Lv, Advanced materials for sodium-ion capacitors with superior energy–power properties: Progress and perspectives, Small, 16 (2020) 1902843.

[164] E.T. Mombeshora, P.G. Ndungu, A.L. Jarvis, V.O. Nyamori, Oxygen-modified multiwalled carbon nanotubes: physicochemical properties and capacitor functionality, International Journal of Energy Research, 41 (2017) 1182–1201.

[165] Y. Wang, Y. Song, Y. Xia, Electrochemical capacitors: mechanism, materials, systems, characterization and applications, Chemical Society Reviews, 45 (2016) 5925–5950.

[166] P. Zhang, X. Zhao, Z. Liu, F. Wang, Y. Huang, H. Li, Y. Li, J. Wang, Z. Su, G. Wei, Exposed high-energy facets in ultradispersed sub-10 nm SnO_2 nanocrystals anchored on graphene for pseudocapacitive sodium storage and high-performance quasi-solid-state sodium-ion capacitors, NPG Asia Materials, 10 (2018) 429–440.

[167] S. Dong, Y. Xu, L. Wu, H. Dou, X. Zhang, Surface-functionalized graphene-based quasi-solid-state Na-ion hybrid capacitors with excellent performance, Energy Storage Materials, 11 (2018) 8–15.

[168] M.D. Stoller, S. Park, Y. Zhu, J. An, R.S. Ruoff, Graphene-based ultracapacitors, Nano Letters, 8 (2008) 3498–3502.

[169] D. Han, J. Zhang, Z. Weng, D. Kong, Y. Tao, F. Ding, D. Ruan, Q.-H. Yang, Two-dimensional materials for lithium/sodium-ion capacitors, Materials Today Energy, 11 (2019) 30–45.

[170] J. Zhang, W. Lv, D. Zheng, Q. Liang, D.-W. Wang, F. Kang, Q.-H. Yang, The interplay of oxygen functional groups and folded texture in densified graphene electrodes for compact sodium-ion capacitors, Advanced Energy Materials, 8 (2018) 1702395.

[171] F. Yu, Z. Liu, R. Zhou, D. Tan, H. Wang, F. Wang, Pseudocapacitance contribution in boron-doped graphite sheets for anion storage enables high-performance sodium-ion capacitors, Materials Horizons, 5 (2018) 529–535.

[172] H. Zhang, R. Lv, Defect engineering of two-dimensional materials for efficient electrocatalysis, Journal of Materiomics, 4 (2018) 95–107.

[173] B. Anasori, M.R. Lukatskaya, Y. Gogotsi, 2D metal carbides and nitrides (MXenes) for energy storage, Nature Reviews Materials, 2 (2017) 1–17.

[174] Y. Dall'Agnese, P.-L. Taberna, Y. Gogotsi, P. Simon, Two-dimensional vanadium carbide (MXene) as positive electrode for sodium-ion capacitors, The Journal of Physical Chemistry Letters, 6 (2015) 2305–2309.

[175] M. Naguib, J. Halim, J. Lu, K.M. Cook, L. Hultman, Y. Gogotsi, M.W. Barsoum, New two-dimensional niobium and vanadium carbides as promising materials for Li-ion batteries, Journal of the American Chemical Society, 135 (2013) 15966–15969.

[176] F. Ming, H. Liang, W. Zhang, J. Ming, Y. Lei, A.-H. Emwas, H.N. Alshareef, Porous MXenes enable high performance potassium ion capacitors, Nano Energy, 62 (2019) 853–860.

[177] W. Wei, X. Cui, W. Chen, D.G. Ivey, Manganese oxide-based materials as electrochemical supercapacitor electrodes, Chemical Society Reviews, 40 (2011) 1697–1721.

[178] N. Karikalan, C. Karuppiah, S.M. Chen, M. Velmurugan, P. Gnanaprakasam, Three-dimensional fibrous network of $Na_{0.21}MnO_2$ for aqueous sodium-ion hybrid supercapacitors, Chemistry–A European Journal, 23 (2017) 2379–2386.

[179] W. Song, X. Ji, Z. Wu, Y. Zhu, Y. Yang, J. Chen, M. Jing, F. Li, C.E. Banks, First exploration of Na-ion migration pathways in the NASICON structure $Na_3V_2(PO_4)_3$, Journal of Materials Chemistry A, 2 (2014) 5358–5362.

[180] L. Yang, W. Wang, M. Hu, J. Shao, R. Lv, Ultrahigh rate binder-free $Na_3V_2(PO_4)_3$/carbon cathode for sodium-ion battery, Journal of Energy Chemistry, 27 (2018) 1439–1445.

[181] K. Dai, J. Mao, X. Song, V. Battaglia, G. Liu, $Na_{0.44}MnO_2$ with very fast sodium diffusion and stable cycling synthesized via polyvinylpyrrolidone-combustion method, Journal of Power Sources, 285 (2015) 161–168.

[182] Z. Chen, T. Yuan, X. Pu, H. Yang, X. Ai, Y. Xia, Y. Cao, Symmetric sodium-ion capacitor based on $Na_{0.44}MnO_2$ nanorods for low-cost and high-performance energy storage, ACS Applied Materials & Interfaces, 10 (2018) 11689–11698.

[183] X. Xie, M.-Q. Zhao, B. Anasori, K. Maleski, C.E. Ren, J. Li, B.W. Byles, E. Pomerantseva, G. Wang, Y. Gogotsi, Porous heterostructured MXene/carbon nanotube composite paper with high volumetric capacity for sodium-based energy storage devices, Nano Energy, 26 (2016) 513–523.

[184] D. Xu, D. Chao, H. Wang, Y. Gong, R. Wang, B. He, X. Hu, H.J. Fan, Flexible quasi-solid-state sodium-ion capacitors developed using 2D metal–organic-framework array as reactor, Advanced Energy Materials, 8 (2018) 1702769.

[185] G. Wang, L. Zhang, J. Zhang, A review of electrode materials for electrochemical supercapacitors, Chemical Society Reviews, 41 (2012) 797–828.

[186] K. Zhu, H. Zhang, K. Ye, W. Zhao, J. Yan, K. Cheng, G. Wang, B. Yang, D. Cao, Two-dimensional titanium carbide MXene as a capacitor-type electrode for rechargeable aqueous Li-ion and Na-ion capacitor batteries, ChemElectroChem, 4 (2017) 3018–3025.

[187] J. Lee, S. Kim, C. Kim, J. Yoon, Hybrid capacitive deionization to enhance the desalination performance of capacitive techniques, Energy & Environmental Science, 7 (2014) 3683–3689.

[188] S. Fleischmann, M. Widmaier, A. Schreiber, H. Shim, F.M. Stiemke, T.J. Schubert, V. Presser, High voltage asymmetric hybrid supercapacitors using lithium-and sodium-containing ionic liquids, Energy Storage Materials, 16 (2019) 391–399.

[189] T.C. Mendes, F. Zhou, A.J. Barlow, M. Forsyth, P.C. Howlett, D.R. MacFarlane, An ionic liquid based sodium metal-hybrid supercapacitor-battery, Sustainable Energy & Fuels, 2 (2018) 763–771.

[190] A. Ponrouch, D. Monti, A. Boschin, B. Steen, P. Johansson, M.R. Palacín, Non-aqueous electrolytes for sodium-ion batteries, Journal of Materials Chemistry A, 3 (2015) 22–42.

[191] Y. Liu, C. Gao, L. Dai, Q. Deng, L. Wang, J. Luo, S. Liu, N. Hu, The features and progress of electrolyte for potassium ion batteries, Small, 16 (2020) 2004096.

[192] M. Shakourian-Fard, G. Kamath, K. Smith, H. Xiong, S.K. Sankaranarayanan, Trends in Na-ion solvation with alkyl-carbonate electrolytes for sodium-ion batteries: insights from first-principles calculations, The Journal of Physical Chemistry C, 119 (2015) 22747–22759.

[193] J. Ding, H. Wang, Z. Li, K. Cui, D. Karpuzov, X. Tan, A. Kohandehghan, D. Mitlin, Peanut shell hybrid sodium ion capacitor with extreme energy–power rivals lithium ion capacitors, Energy & Environmental Science, 8 (2015) 941–955.

[194] Y. Xu, C. Zhang, M. Zhou, Q. Fu, C. Zhao, M. Wu, Y. Lei, Highly nitrogen doped carbon nanofibers with superior rate capability and cyclability for potassium ion batteries, Nature Communications, 9 (2018) 1720.

[195] U.N. Maiti, W.J. Lee, J.M. Lee, Y. Oh, J.Y. Kim, J.E. Kim, J. Shim, T.H. Han, S.O. Kim, 25th anniversary article: Chemically modified/doped carbon nanotubes & graphene for optimized nanostructures & nanodevices, Advanced Materials, 26 (2014) 40–66.

[196] T. Van Khai, H.G. Na, D.S. Kwak, Y.J. Kwon, H. Ham, K.B. Shim, H.W. Kim, Significant enhancement of blue emission and electrical conductivity of N-doped graphene, Journal of Materials Chemistry, 22 (2012) 17992.

[197] M. Acik, C. Mattevi, C. Gong, G. Lee, K. Cho, M. Chhowalla, Y.J. Chabal, The role of intercalated water in multilayered graphene oxide, ACS Nano, 4 (2010) 5861–5868.

[198] S.W. Lee, N. Yabuuchi, B.M. Gallant, S. Chen, B.S. Kim, P.T. Hammond, Y. Shao-Horn, High-power lithium batteries from functionalized carbon-nanotube electrodes, Nature Nanotechnology, 5 (2010) 531–537.

[199] S.W. Lee, B.-S. Kim, S. Chen, Y. Shao-Horn, P.T. Hammond, Layer-by-layer assembly of all carbon nanotube ultrathin films for electrochemical applications, Journal of the American Chemical Society, 131 (2009) 671–679.

[200] H. Kim, J.C. Kim, S.-H. Bo, T. Shi, D.-H. Kwon, G. Ceder, K-ion batteries based on a P2-type $K_{0.6}CoO_2$ cathode, Advanced Energy Materials, 7 (2017) 1700098.

[201] X. Wang, X. Xu, C. Niu, J. Meng, M. Huang, X. Liu, Z. Liu, L. Mai, Earth abundant Fe/Mn-based layered oxide interconnected nanowires for advanced K-ion full batteries, Nano Letters, 17 (2017) 544–550.

[202] W.B. Park, S.C. Han, C. Park, S.U. Hong, U. Han, S.P. Singh, Y.H. Jung, D. Ahn, K.-S. Sohn, M. Pyo, KVP_2O_7 as a robust high-energy cathode for potassium-ion catteries: Pinpointed by a full screening of the inorganic registry under specific search conditions, Advanced Energy Materials, 8 (2018) 1703099.

[203] M. Clites, J.L. Hart, M.L. Taheri, E. Pomerantseva, Chemically preintercalated bilayered $K_xV_2O_5{\cdot}nH_2O$ nanobelts as a high-performing cathode material for K-ion batteries, ACS Energy Letters, 3 (2018) 562–567.

[204] Y.-H. Zhu, X. Yang, D. Bao, X.-F. Bie, T. Sun, S. Wang, Y.-S. Jiang, X.-B. Zhang, J.-M. Yan, Q. Jiang, High-energy-density flexible potassium-ion battery based on patterned electrodes, Joule, 2 (2018) 736–746.

[205] T. Deng, X. Fan, J. Chen, L. Chen, C. Luo, X. Zhou, J. Yang, S. Zheng, C. Wang, Layered P2-type $K_{0.65}Fe_{0.5}Mn_{0.5}O_2$ microspheres as superior cathode for high-energy potassium-ion batteries, Advanced Functional Materials, 28 (2018) 1800219.

[206] C. Zhang, Y. Xu, M. Zhou, L. Liang, H. Dong, M. Wu, Y. Yang, Y. Lei, Potassium Prussian blue nanoparticles: A low-cost cathode material for potassium-ion batteries, Advanced Functional Materials, 27 (2017) 1604307.

[207] H. Kim, Y.-U. Park, K.-Y. Park, H.-D. Lim, J. Hong, K. Kang, Novel transition-metal-free cathode for high energy and power sodium rechargeable batteries, Nano Energy, 4 (2014) 97–104.

[208] V. Augustyn, J. Come, M.A. Lowe, J.W. Kim, P.L. Taberna, S.H. Tolbert, H.D. Abruna, P. Simon, B. Dunn, High-rate electrochemical energy storage through Li^+ intercalation pseudocapacitance, Nature Materials, 12 (2013) 518–522.

[209] S. Ardizzone, Fregonara, G., and Trasatti, S., "Inner" and "outer" active surface of RuO_2 electrodes, Electrochimica Acta, 35 (1989) 263–267.

[210] Y. Luo, L. Liu, K. Lei, J. Shi, G. Xu, F. Li, J. Chen, A nonaqueous potassium-ion hybrid capacitor enabled by two-dimensional diffusion pathways of dipotassium terephthalate, Chemical Science, 10 (2019) 2048–2052.

[211] Y. Wang, Z. Zhang, G. Wang, X. Yang, Y. Sui, F. Du, B. Zou, Ultrafine Co_2P nanorods wrapped by graphene enable a long cycle life performance for a hybrid potassium-ion capacitor, Nanoscale Horizons, 4 (2019) 1394–1401.

[212] H.V. Ramasamy, B. Senthilkumar, P. Barpanda, Y.-S. Lee, Superior potassium-ion hybrid capacitor based on novel P3-type layered $K_{0.45}Mn_{0.5}Co_{0.5}O_2$ as high capacity cathode, Chemical Engineering Journal, 368 (2019) 235–243.

[213] W. Hummers, R. Offeman, Graphene oxide, Journal of the American Chemical Society 80 (1958) 1339.

[214] Y. Zhu, S. Murali, M.D. Stoller, K. Ganesh, W. Cai, P.J. Ferreira, A. Pirkle, R.M. Wallace, K.A. Cychosz, M. Thommes, Carbon-based supercapacitors produced by activation of graphene, Science, 332 (2011) 1537–1541.

[215] Y. Sun, J. Tang, K. Zhang, J. Yuan, J. Li, D.M. Zhu, K. Ozawa, L.C. Qin, Comparison of reduction products from graphite oxide and graphene oxide for anode applications in lithium-ion batteries and sodium-ion batteries, Nanoscale, 9 (2017) 2585–2595.

[216] C. Zhang, Y. Xu, K. He, Y. Dong, H. Zhao, L. Medenbach, Y. Wu, A. Balducci, T. Hannappel, Y. Lei, Polyimide@ketjenblack composite: A porous organic cathode for fast rechargeable potassium-ion batteries, Small, 16 (2020) 2002953.

[217] V. Augustyn, P. Simon, B. Dunn, Pseudocapacitive oxide materials for high-rate electrochemical energy storage, Energy & Environmental Science, 7 (2014) 1597.

[218] W. Weppner, R. Huggins, Electrochemical investigation of the chemical diffusion, partial ionic conductivities, and other kinetic parameters in Li_3Sb and Li_3Bi, Journal of Solid State Chemistry, 22 (1977) 297–308.

[219] X. Xuan, J. Wang, H. Wang, Theoretical insights into $PF6^-$ and its alkali metal ion pairs: geometries and vibrational frequencies, Electrochimica Acta, 50 (2005) 4196–4201.

[220] J. Zhang, Z. Cao, L. Zhou, G.-T. Park, L. Cavallo, L. Wang, H.N. Alshareef, Y.-K. Sun, J. Ming, Model-based design of stable electrolytes for potassium ion batteries, ACS Energy Letters, 5 (2020) 3124–3131.

[221] L. Zhou, Z. Cao, W. Wahyudi, J. Zhang, J.-Y. Hwang, Y. Cheng, L. Wang, L. Cavallo, T. Anthopoulos, Y.-K. Sun, H.N. Alshareef, J. Ming, Electrolyte engineering enables high stability and capacity alloying anodes for sodium and potassium ion batteries, ACS Energy Letters, 5 (2020) 766–776.

[222] Y. Huang, L. Zhao, L. Li, M. Xie, F. Wu, R. Chen, Electrolytes and electrolyte/electrode interfaces in sodium-ion batteries: From scientific research to practical application, Advanced Materials, 31 (2019) 1808393.

[223] Z. Jian, C. Bommier, L. Luo, Z. Li, W. Wang, C. Wang, P.A. Greaney, X. Ji, Insights on the mechanism of Na-ion storage in soft carbon anode, Chemistry of Materials, 29 (2017) 2314–2320.

[224] Z.W. Seh, J. Sun, Y. Sun, Y. Cui, A highly reversible room-temperature sodium metal anode, ACS Central Science, 1 (2015) 449–455.

[225] X. Fan, F. Wang, X. Ji, R. Wang, T. Gao, S. Hou, J. Chen, T. Deng, X. Li, L. Chen, C. Luo, L. Wang, C. Wang, A universal organic cathode for ultrafast lithium and multivalent metal batteries, Angewandte Chemie International Edition, 57 (2018) 7146–7150.

[226] X. Yang, A.L. Rogach, Electrochemical techniques in battery research: a tutorial for nonelectrochemists, Advanced Energy Materials, 9 (2019) 1900747.

[227] H. Kim, J. Hong, Y.U. Park, J. Kim, I. Hwang, K. Kang, Sodium storage behavior in natural graphite using ether-based electrolyte systems, Advanced Functional Materials, 25 (2015) 534–541.

[228] Q. Wei, Q. Li, Y. Jiang, Y. Zhao, S. Tan, J. Dong, L. Mai, D.-L. Peng, High-Energy and High-Power Pseudocapacitor–battery hybrid sodium-ion capacitor with Na^+ intercalation pseudocapacitance anode, Nano-Micro Letters, 13 (2021) 1–13.

[229] K. Naoi, S. Ishimoto, Y. Isobe, S. Aoyagi, High-rate nano-crystalline $Li_4Ti_5O_{12}$ attached on carbon nano-fibers for hybrid supercapacitors, Journal of Power Sources, 195 (2010) 6250–6254.

Appendix I: techniques for characterization and analysis

In this dissertation, some typical physicochemical characterization techniques such as SEM, TEM, XRD, XPS, and Raman spectroscopy are applied to analyze the morphology, surface, and crystalline structure of the studied materials. In addition, some typical electrochemical measuring techniques including CV, GITT, EIS are applied to analyze the electrochemical properties of the studied materials. Herein, the theory and principles of these techniques are extensively discussed and explained.

AI.1 Scanning electron microscope (SEM)

The SEM instrument is a type of electron microscope that images a material by scanning the surface with a focused beam of electrons. Specifically, the electron beam from the sources strikes the atoms of the material, providing energy to the atomic electrons which then emits various signals (Figure 9-1), such as secondary electrons, backscattered electrons, Auger electrons, X-rays, and visible light (cathodoluminescence).[AI. B1] By collecting the signals and manipulating them with the computer, a required image can be obtained. According to the detected signals including secondary electrons, backscattered electrons, and X-rays, different information of the material can be observed. The secondary electrons are used for imaging the morphology and topography of the material. The backscattered electrons are used for indicating the contrasts in multiphase materials composition. The X-rays are used for the element analysis of the material.

The basic operation requirement for SEM is the high vacuum environment, avoiding the interaction of the focused beam with gas molecules and other particles in order to obtain a high-resolution image. The primary electron beam produced and emitted from the electron gun is accelerated by heating or applying high energy in the range of 1–50 keV. The resolution of the microscope depends on the diameter of the focused electron beam (diameter of 100 nm or less).

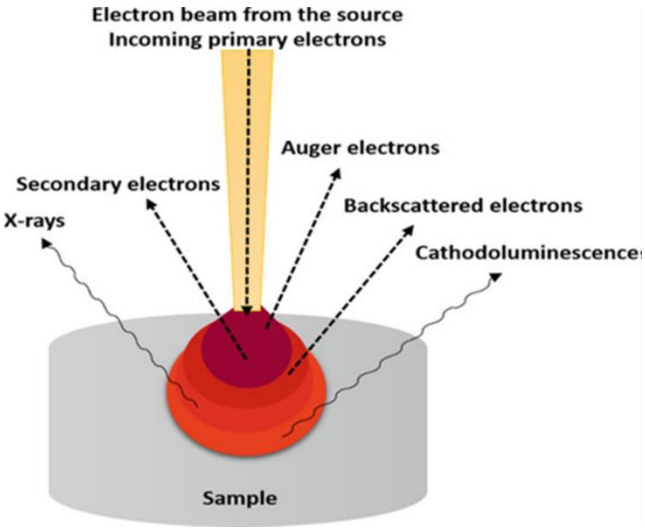

Figure 9-1 The interaction of electron beam with specimen and the signal emitted from the sample.[AI. B1]

AI.2 Transmission electron microscope (TEM)

The TEM instrument also images a material through the interaction of the material and focused electron beam. The major difference between TEM and SEM is that the SEM image is obtained by collecting the reflected electrons, whereas the TEM image is obtained by collecting the transmitted electrons (transmitted electrons experience the elastic and inelastic interaction), as shown in Figure 9-2.[AI. B1] The transmitted electron beam contains information about electron density, phase, and periodicity. The different electron transmitted electrons can be used for different techniques in TME. In consequence, the TEM characterization can offer information on the internal structure of the material in terms of crystal structure, morphology, the multiphase materials composition in bulk.

It is also essential to operate the TEM in a high vacuum environment. The electron beam is focused into a very fine beam using an electromagnetic lens system. The electron beam can be accelerated by a high voltage range of 60–300 keV. In addition, the magnification of TEM is more than 50 million times, while SEM is limited to 1-2 million times. TEM even enables the observation of the distribution of atoms. The resolution of TEM is as small as 01–0.2 nm.

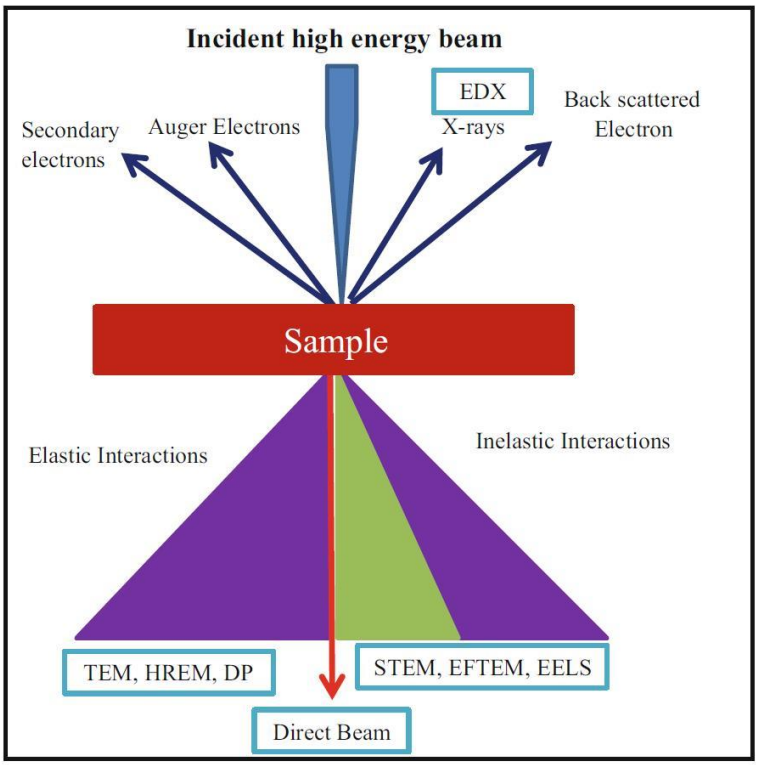

Figure 9-2 Schemic of different electron interaction with mater and corresponding teachniques in TEM using specific interaction.[AI. B1]

AI.3 Raman spectroscopy

Raman spectroscopy is an analysis method based on the Raman scattering effect, which analyzes the scattering spectra with a frequency different from the incident light to obtain information on molecular vibration and rotation. Therefore, Raman spectroscopy is generally applied to molecular structure research. As shown in Figure 9-3, the incident monochromatic laser beam will interact with the material molecules, the scattered photons are observed in the perpendicular direction to the incident light. These photons can be categorized into two parts. When the scattered photons have the same frequency as the incident light, we call them Rayleigh scattering. When the scattered photons have a lower or higher frequency than the incident light, we call it Raman scattering. In principle, the Raman scattering has the frequency $\upsilon_0 \pm \upsilon_R$, where υ_R is the frequency corresponding to molecular vibration. The scattered photons with the frequency of $\upsilon_0+\upsilon_R$ are called anti-Stokes Raman scattering ($\lambda_{scatter} < \lambda_{laser}$), and the scattered photons with the frequency of $\upsilon_0-\upsilon_R$ are called Stokes Raman scattering ($\lambda_{scatter} > \lambda_{laser}$). Therefore, Raman spectroscopy can measure the molecular vibration frequency (υ_R) as a shift from the incident frequency (υ_0).[AI. B2]

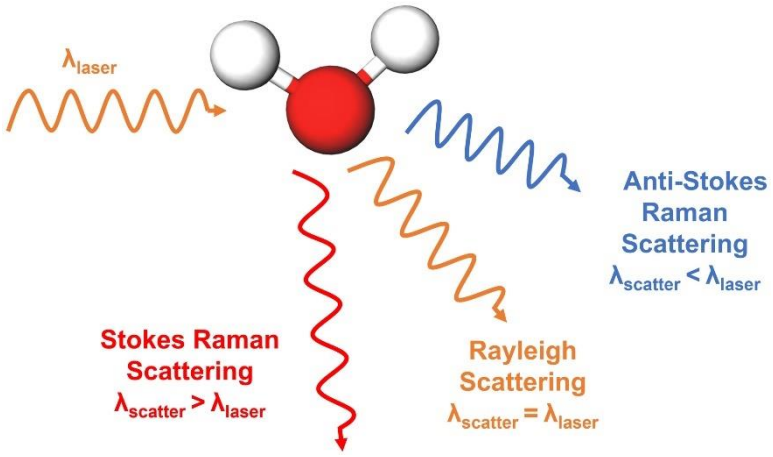

Figure 9-3 Types of scattering process that occur when light interacts with a molecule.

AI.4 X-ray diffraction (XRD)

XRD is a non-destructive characterization that is generally used for identifying the phase composition and crystalline structure of a material. In principle, all crystalline materials have an ordered components (atoms, ions, or molecules) arrangement. It is a necessary condition to comply with the requirement for XRD utilization. It is because that diffraction can only occur if X-rays are scattered by a long-range ordered array of particles. As shown in Figure 9-4, the XRD is based on constructive interference of monochromatic X-rays. The incident X-rays are produced by a cathode ray tube, filtered to generate monochromatic radiation. When the incident X-rays interact with the material, constructive interference happens only if the condition obeys Bragg's law:

$$n\lambda = 2d \times \sin\theta \qquad Eq.A1$$

The magnitude of this path length only depends on the distance between the crystal planes and the incident angle of the X-ray beam.[AI. B3]

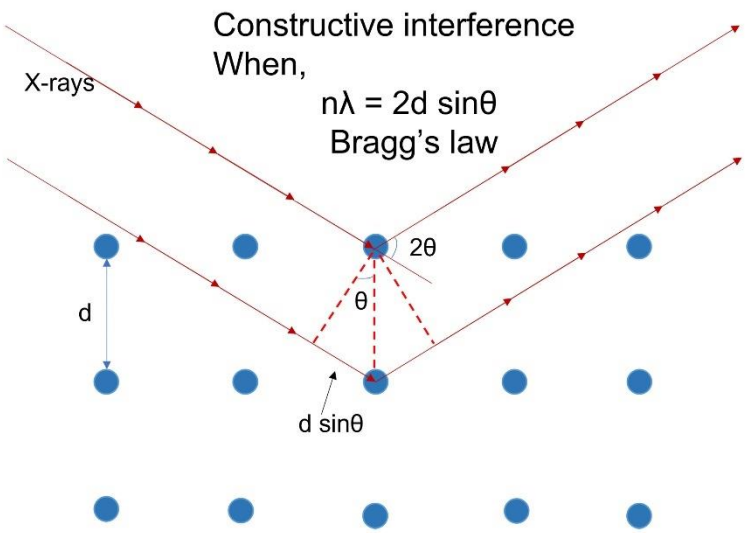

Figure 9-4 Schematic representation of the Bragg equation.

AI.5 X-ray photoelectron spectroscopy (XPS)

XPS is a quantitative analysis technique that is used for identifying the elements, elements' chemical state, electronic structure, and density of electronic states in a material or on the surface of a material. As shown in Figure 9-5, the X-ray beam irradiates a material with the energy of hν, the XPS spectra are obtained by measuring the kinetic energy (E_k) and the number of escaped electrons from the top of a material (1–10 nm). The binding energy (E_B) of the detected element can be determined according to the photoelectric effect equation:

$$E_B = h\nu - E_k - \Phi_{sp} \qquad Eq.A2$$

where Φ_{sp} is the work function for the specific surface of the material. In addition, the intensity of peaks in XPS spectra can provide information about the content of elements or chemical bonds presented in the material. XPS instrument also requires an ultra-high vacuum to avoid the energy loss of a particular X-ray wavelength.[AI. B4]

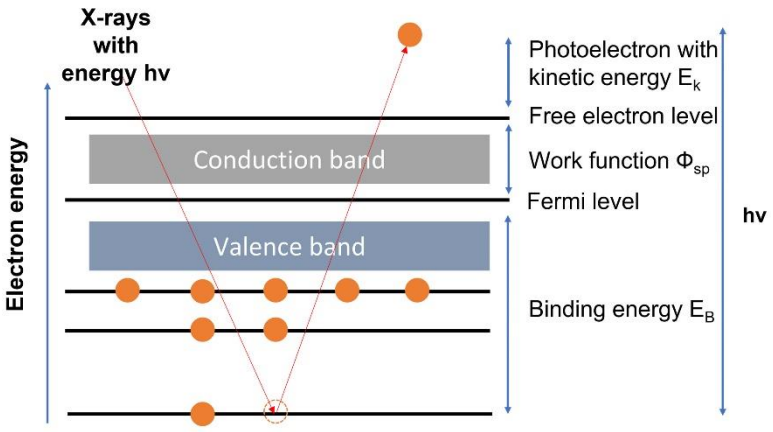

Figure 9-5 Schematic representation of the Principle of XPS.

AI.6 Cell configuration

The laboratory research for battery assessment generally employs coin cells configuration. In this dissertation, we use type 2032 coin cells to assemble the batteries. As shown in Figure Figure 9-6, the coin cells are assembled by following steps:

a. Placing the cathode materials on the cell can.

b. Wetting the separator with electrolyte and placing it on the cathode materials.

c. Placing the anode materials on the separator.

d. Placing the spacer and spring on the anode material successively, then sealing the cell with the cap.

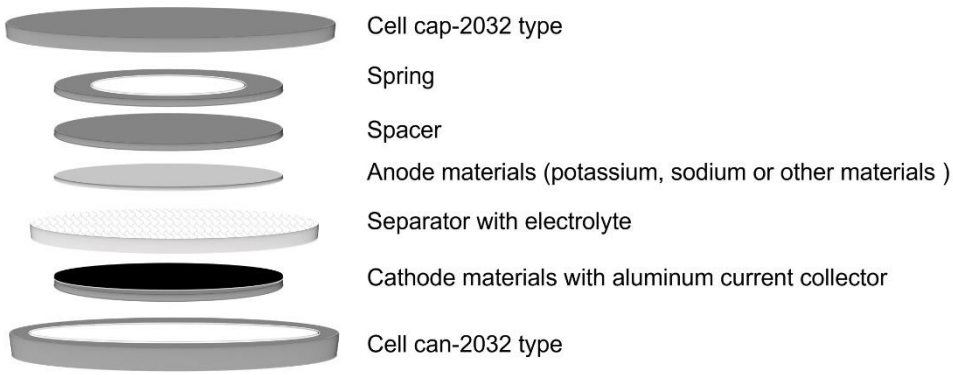

Figure 9-6 Construction of a coin cell.

AI.7 Cyclic voltammetry (CV)

CV measurement is one of the primary techniques in electrochemical characterization. It is generally used for qualitatively and quantitatively analyzing electrode redox reactions. To conduct the CV measurement, we need to determine the voltage window (V_1–V_2) and scan

rate (v). The typical current response (i) can be generated as the electron transfer between the active material and electrode.[AI. B5]

For the qualitative analysis, Figure 9-7 shows four typical shapes of CV curves that are accordant with the different charge storage mechanisms.[AI. B6] The EDLC and surface redox reaction can be identified if the CV curve is a box-like shape. The pseudocapacitor-type intercalation reaction exhibits a broad peak in a certain voltage window, whereas the battery-type redox reaction exhibits sharp cathodic and anodic peaks. Reaction kinetics always play an important role in evaluating the ion-storage facilitation of electrode materials. In practice, lots of ion-storage devices are designed to be pseudocapacitive while maintaining battery-type ion storage behavior.

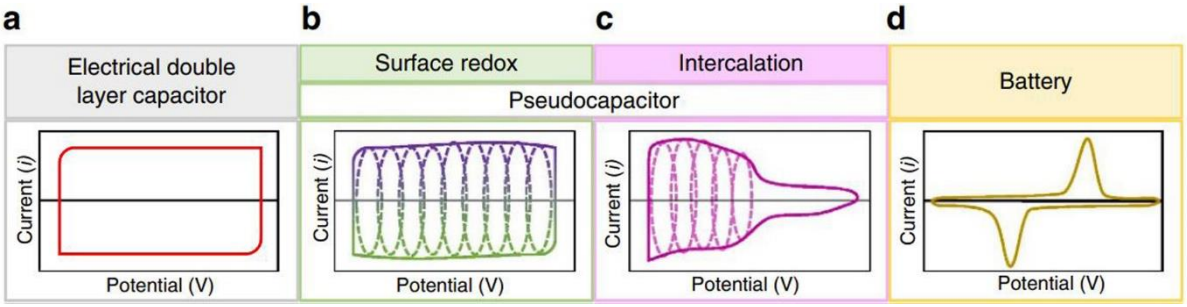

Figure 9-7 Summary of representative CV curves describing the different charge storage mechanisms.[AI. B6]

To separate the contribution of different ion storage characteristics, the CV measurements at different scan rates need to be carried out. The peak current (i_p) and scan rate (v) obey a relation as:

$$i_p = av^b \qquad Eq.A3$$

$$\log(i_p) = \log(a) + b \times \log(v) \qquad Eq.A4$$

After the transformation of the formula, the linear relationship between log (i_p) and log (v) is confirmed. The b-value can be obtained by calculating the slope of the linear plot. The b-value of 5 refers to the dominance of diffusion-controlled reaction, while the b-value of 1 refers to the capacitive charge storage behavior.[AI. B7–8]

Further quantitatively analysis can determine the specific diffusion and capacitive contributions using the relationship between current response (i) with the combination of

capacitive contribution (k_1v) and diffusion controlled contribution ($k_2v^{1/2}$), according to the equations:

$$i = k_1 v + k_2 v^{1/2} \qquad Eq.A5$$

$$\frac{i}{v^{1/2}} = k_1 v^{1/2} + k_2 \qquad Eq.A6$$

After the transformation of the formula, a linear relationship between $\frac{i}{v^{1/2}}$ and $v^{1/2}$ is confirmed. By determining the k_1 and k_2, the response currents of capacitive contribution (k_1v) and diffusion-controlled contribution ($k_2v^{1/2}$) are obtained. Thereby, the percentage of diffusion-controlled capacity and capacitive capacity can be estimated.

AI.8 Galvanostatic (GA) charge/discharge

GA **c**harge/discharge measurement is carried out by using a fixed current density within a voltage window. The charge storage (Q) of certain electrode material is calculated by the integral of the applied current density (i) and consuming charge or discharge time (t), defined in the following equation:

$$Q = \int_0^t i(t) d_t \qquad Eq.A7$$

While, the charge storage is normally defined by the specific capacity (c), measured in (mAh g^{-1}), as described equation below:

$$c = \frac{Q}{m} \qquad Eq.A8$$

where m is the active mass of the electrode material. By calculating the theoretical specific capacity or measuring the specific capacity, the ion-storage capability of a material can be evaluated. Besides, the electrode-electrolyte reaction, electrode decomposition or pulverization can cause irreversible capacity loss, differentiating the charge and discharge capacities. The coulombic efficiency (CE) is defined to assess this circumstance, as described below:

$$CE = \frac{c_{discharge}}{c_{charge}} \qquad Eq.A9$$

where $c_{discharge}$ and c_{charge} are the discharge specific capacity and charge specific capacity, respectively.

In addition, the galvanostatic intermittent titration technique (GITT) is generally applied to retrieve both thermodynamics and kinetics parameters. It is carried out by separating GA charge/discharge processes into many small and equivalent segments, where the cell is relaxed from kinetic equilibrium state to thermodynamic equilibrium state for each charge and discharge segment. The GITT procedure consists of a series of fixed current pulses, each followed by a fixed relaxation time, in which the cell has no current input.[AI. B5] Based on the GITT theory, the ion diffusion coefficient (d_k) can be calculated, according to the equation:

$$D_K = \frac{4}{\pi\tau}\left(\frac{m_B V_M}{M_B S}\right)^2\left(\frac{\Delta E_S}{\Delta E_\tau}\right)^2 \quad \left(t \ll \frac{L_2}{D}\right) \qquad Eq.A10$$

where m_B, V_M, and M_B are the mass, molecular volume, and molar mass of the active materials, respectively; τ is the pulse time (s); S is the area of the electrode; $\triangle E_S$ and $\triangle E_\tau$ are defined in Figure 9-8.

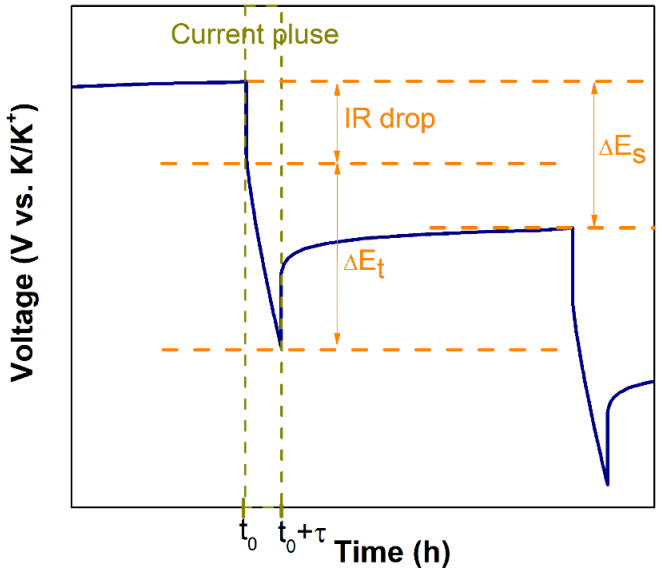

Figure 9-8 Schematic of calculation of diffusion coefficient using the GITT technique.

AI.9 Electrochemical impedance spectroscopy (EIS)

EIS measurement is used for obtaining accurate information about the electron transport properties in an energy storage device. It is generally carried out by applying an AC potential to an electrochemical cell with a range of frequencies, subsequently measuring the current through the cell. Figure 9-9 shows a typical Nyquist plot and its corresponding equivalent

electrical circuit, where R_{int} is the internal resistance, C_{dl} is the double layer capacitance, R_{ct} is the charge transfer resistance at the interface, and Z_w is the Warburg impedance corresponding to the charge transfer resistance in the bulk phase. The combination of all these elements is known as a Randles circuit. Since the ion diffusion is not an instantaneous process, their concentration can be considered as a constant value when the applied frequency is high enough, thereby Z_w almost contributes no impedance to the overall part.[AI. B5] In this regard, the real and imaginary parts of impedance can be expressed as equations:

$$Z' = R_{int} + \frac{R_{ct}}{1 + \omega^2 C_{dl}^2 R_{ct}^2} \qquad Eq.A11$$

$$Z'' = -\frac{\omega C_{dl} R_{ct}^2}{1 + \omega^2 C_{dl}^2 R_{ct}^2} \qquad Eq.A12$$

where the Z' is the real partc and Z'' is the imaginary part, the ω is the angular frequency.

When EIS data deviate from a standard Randles model, it may be difficult to fit convincing equivalent circuits. Nevertheless, even without performing numerical fitting, EIS data are still useful, such as:

a) The span of semicircle or arc in the high-frequency region is a rough estimation of R_{ct}.

b) The number of semicircles or arcs is usually the number of capacitors in the equivalent circuit.

c) The slope in the low-frequency region is a qualitative indicator of capacitive or battery-like behaviors, as well as roughly estimating the diffusion coefficient.

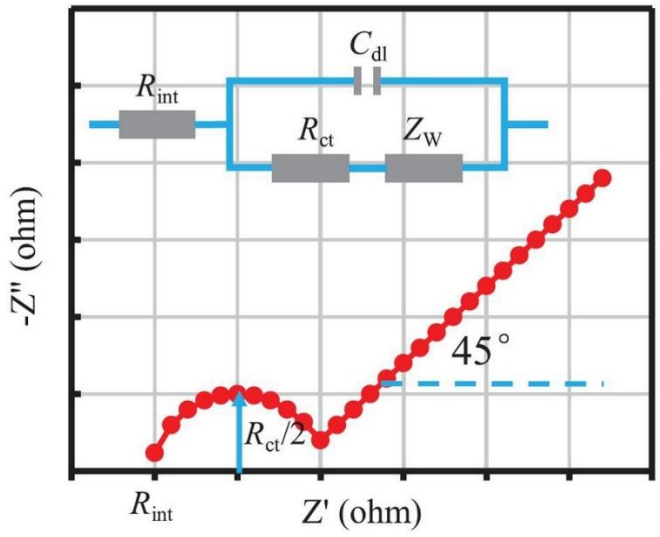

Figure 9-9 Nyquist plot and the corresponding equivalent electrical circuit.[AI. B5]

AI.10 Bibliography for Appendix I

[AI. B1] S.K. Sharma, D.S. Verma, L.U. Khan, S. Kumar, S.B. Khan, Handbook of Materials Characterization, Springer 2018.

[AI. B2] E. Smith, G. Dent, The theory of Raman spectroscopy, Modern Raman Spectroscopy-A Practical Approach, (2005) 71-92.

[AI. B3] C.D. Igwebike-Ossi, X-ray techniques, failure analysis and prevention. InTechOpen, (2017) 153-172.

[AI. B4] J.F. Watts, X-ray photoelectron spectroscopy, Surface Science Techniques, 45 (1994) 5.

[AI. B5] X. Yang, A.L. Rogach, Electrochemical techniques in battery research: a tutorial for nonelectrochemists, Advanced Energy Materials, 9 (2019) 1900747.

[AI. B6] M.R. Lukatskaya, B. Dunn, Y. Gogotsi, Multidimensional materials and device architectures for future hybrid energy storage, Nature Communications, 7 (2016) 1-13.

[AI. B7] H. Lindström, S. Södergren, A. Solbrand, H. Rensmo, J. Hjelm, A. Hagfeldt, S.-E. Lindquist, Li^+ ion insertion in TiO_2 (anatase). 2. Voltammetry on nanoporous films, The Journal of Physical Chemistry B, 101 (1997) 7717-7722.

[AI. B8] V. Augustyn, P. Simon, B. Dunn, Pseudocapacitive oxide materials for high-rate electrochemical energy storage, Energy & Environmental Science, 7 (2014) 1597-1614.

Appendix II: extended works

During the period of my Ph.D. study, besides the research works presented in the dissertation, I have not only focused on the oxygen-doped carbon materials and hybrid ion capacitors, but also have been extended to the electrode materials for potassium-ion batteries, such as nitrogen-doped carbon anode, Bi anode, Bi_2Se_3 anode, and organic polyimide cathode. I also wrote and published a review article. The abstracts and table of content figures of the representative papers are illustrated in this chapter to highlight my scientific achievements beyond the scope of this dissertation.

1) Highly nitrogen doped carbon nanofibers with superior rate capability and cyclability for potassium ion batteries (shared first authorship, contributed equally)

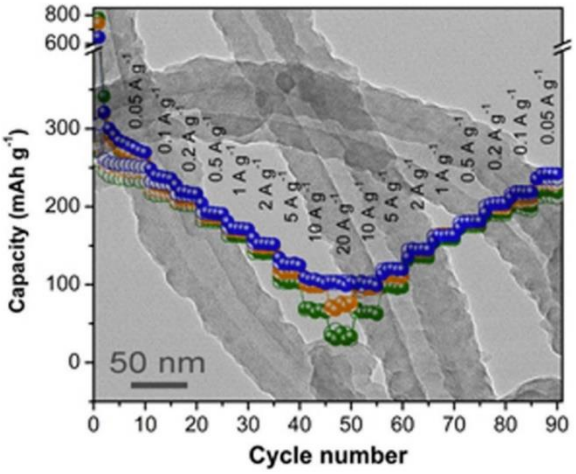

Potassium-ion batteries are a promising alternative to lithium-ion batteries. However, it is challenging to achieve fast charging/discharging and long cycle life with the current electrode materials because of the sluggish potassiation kinetics. Here we report a soft carbon anode, namely highly nitrogen-doped carbon nanofibers, with superior rate capability and cyclability. The anode delivers reversible capacities of 248 mAh g^{-1} at 25 mA g^{-1} and 101 mAh g^{-1} at 20 A g^{-1}, and retains 146 mAh g^{-1} at 2 A g^{-1} after 4000 cycles. Surface-dominated K-storage is verified by quantitative kinetics analysis and theoretical investigation. A full cell coupling the anode and Prussian blue cathode delivers a reversible capacity of 195 mAh g^{-1} at 0.2 A g^{-1}. Considering the cost-effectiveness and material sustainability, our work may shed some light on searching for K-storage materials with high performance.

2) Polyimide@Ketjenblack composite: a porous organic cathode for fast rechargeable potassium-ion batteries (first authorship)

Potassium-ion batteries (PIBs) configurated by organic electrodes have been identified as a promising alternative to lithium-ion batteries. Here, a porous organic Polyimide@Ketjenblack

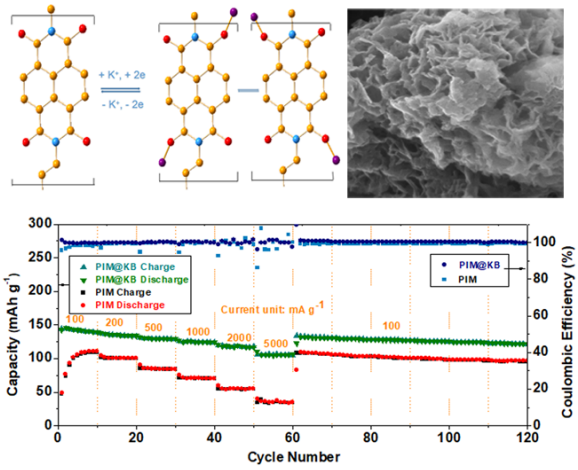

is demonstrated in PIBs as a cathode, which exhibits excellent performance with a large reversible capacity (143 mAh g^{-1} at 100 mA g^{-1}), high rate capability (125 and 105 mAh g^{-1} at 1000 and 5000 mA g^{-1}), and long cycling stability (76% capacity retention at 2000 mA g^{-1} over 1000 cycles). The domination of fast capacitive-like reaction kinetics is verified, which benefits from the porous structure synthesized using in situ polymerization. Moreover, a renewable and low-cost full cell is demonstrated with superior rate behavior (106 mAh g^{-1} at 3200 mA g^{-1}). This work proposes a strategy to design polymer electrodes for high-performance organic PIBs.

3) Recent research progress of anode materials for potassium-ion Batteries (first authorship)

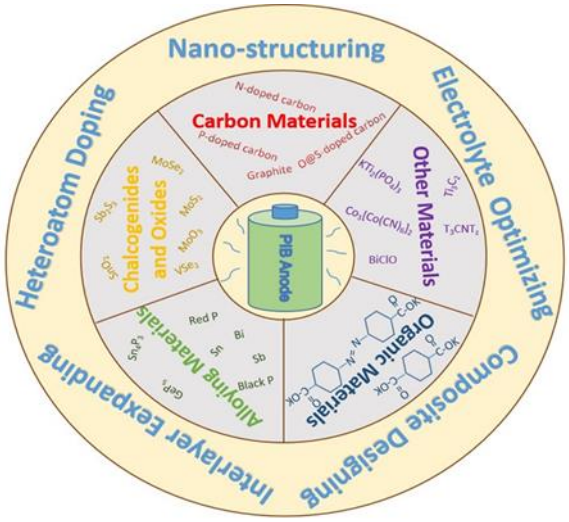

The next-generation smart grid for the storage and delivery of renewable energy urgently needs to develop a low-cost and rechargeable energy storage technology beyond lithium-ion batteries (LIBs). Owing to the abundance of potassium (K) resources and the similar electrochemical performance to that of LIBs, potassium-ion batteries (PIBs) have been attracted considerable interest in recent years, and significant progress has been achieved concerning the discovery of high-performance electrode materials for PIBs. This review especially summarizes the latest research progress regarding anode materials for PIBs, including carbon materials, organic materials, alloys, metal-based compounds, and other new types of compounds. The reversible K-ion storage principle and the electrochemical performance (i.e., capacity, potential, rate capability, and cyclability) of these developed anode materials are summarized. Furthermore, the challenges and the corresponding effective

strategies to enhance the battery performance of the anode materials are highlighted. Finally, prospects of the future development of high-performance anode materials for PIBs are discussed.

4) Bismuth nanoparticles confined in carbonaceous nanospheres as anodes for high-performance potassium-ion batteries (shared first authorship, contributed equally)

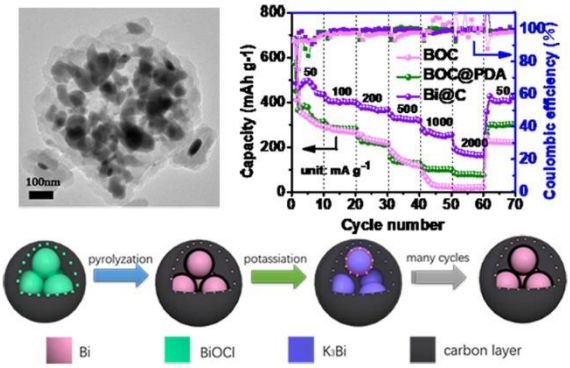

Bismuth (Bi) has been considered as a promising alloying-type anode for potassium-ion batteries (PIBs), owing to its high theoretical capacity and suitable working voltage plateaus. However, Bi suffers from dramatic volume fluctuation and significant pulverization during the discharge/charge processes, resulting in fast capacity decay. Herein, we synthesize Bi nanoparticles confined in carbonaceous nanospheres (denoted as Bi@C) for PIBs by first utilizing BiOCl nanoflakes as a hard template and a Bi precursor. The construction of the loose structure buffers the mechanical stresses resulting from the volume expansion of Bi during the alloying reaction and avoids the fracture of the electrode structure, thus improving the cycling performance. Moreover, the carbonaceous layers increase the electronic conductivity and disperse the Bi nanoparticles, enhancing the charge transportation and ionic diffusion, which further promotes the rate capability of Bi@C. It exhibits a superior capacity (389 mAh g^{-1} at 100 mA g^{-1} after 100 cycles), excellent cycling stability (206 mAh g^{-1} at 500 mA g^{-1} over 1000 cycles), and an improved rate capability (182 mAh g^{-1} at 2.0 A g^{-1}). This work provides a new structuring strategy in alloying materials for boosting reversible and stable potassium-ion storage.

5) Bismuth selenide nanosheets confined in thin carbon layers as anode material for advanced potassium-ion batteries (shared first authorship, contributed equally)

Metal selenides as promising anode materials for potassium ion batteries (PIBs) have attracted high research attention. However, it is still a challenge to promote its practical application due to the unsatisfactory cyclability resulting from large volume variation and sluggish kinetics. Herein, we tackle this issue by focusing on a promising but non-demonstrated anode, bismuth

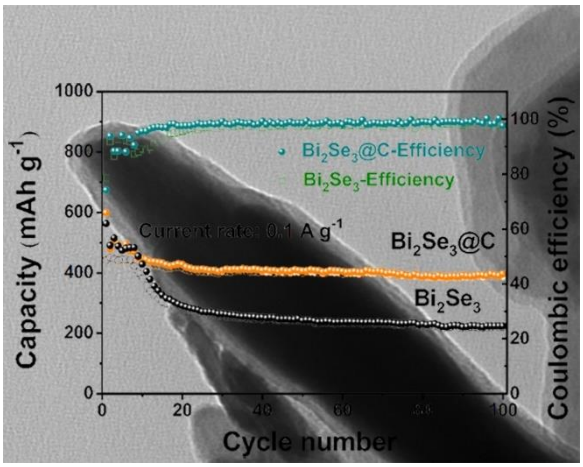

selenide for PIBs which possesses a high theoretical capacity and good electronic conductivity. Benefitting from carbon layers coating, Bi_2Se_3@C owns the capability to inhibit self-aggregation and buffer the volume expansion, leading to outstanding potassium-ion storage capability. It exhibits a very high reversible capacity of 526 mAh g^{-1} at 50 mA g^{-1}, as well as superior cyclability and rate capability with maintaining a high capacity of 214 mAh g^{-1} at 1.0 A g^{-1} after 1000 cycles. Furthermore, the fast and reversible ion storage mechanism was verified, which undergoes first conversion and subsequent alloying redox reactions. This work enriches the understanding and development of stable conversion/alloying-based anode for high-performance potassium-ion batteries.

6) Enhanced potassium storage capability of two-dimensional transition-metal chalcogenides enabled by a collective strategy (co-authorship, in cooperation with Yuhan Wu)

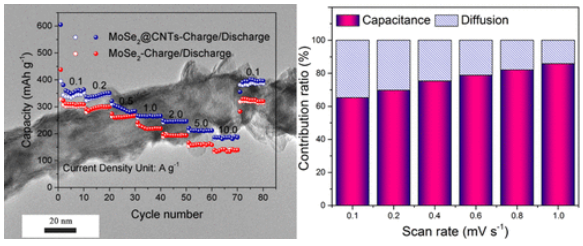

Potassium-ion batteries (PIBs) have been considered as a promising alternative to lithium-ion batteries due to their merits of high safety and low cost. Two-dimensional transition-metal chalcogenides (2D TMCs) with high theoretical specific capacities and unique layered structures have been proven to be amenable materials for PIB anodes. However, some intrinsic properties including severe stacking and unsatisfactory conductivity restrict their electrochemical performance, especially rate capability. Herein, we prepared a heterostructure of high-crystallized ultrathin $MoSe_2$ nanosheet-coated multiwall carbon nanotubes and investigated its electrochemical properties with a view of demonstrating the enhancement of a collective strategy for K storage of 2D TMCs. In such a heterostructure, the constructive contribution of CNTs not only suppresses the restacking of $MoSe_2$ nanosheets but also accelerates electron transport. Meanwhile, the $MoSe_2$ nanosheets loaded on CNTs exhibit an ultrathin feature, which can expose abundant

active sites for the electrochemical reaction and shorten K^+ diffusion length. Therefore, the synergistic effect between ultrathin $MoSe_2$ and CNTs endows the resulting nanocomposite with superior structural and electrochemical properties. Additionally, the high crystallinity of the $MoSe_2$ nanosheets further leads to the improvement of electrochemical performance. The composite electrode delivers high-rate capacities of 209.7 and 186.1 mAh g^{-1} at high current densities of 5.0 and 10.0 A g^{-1}, respectively.

7) Recent advances in ferromagnetic metal sulfides and selenides as anodes for sodium- and potassium-ion batteries (co-authorship, in cooperation with Yuhan Wu)

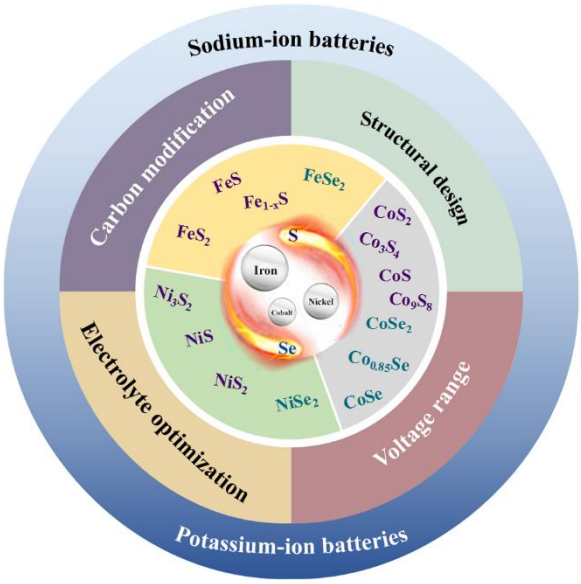

In next-generation rechargeable batteries, sodium-ion batteries (SIBs) and potassium-ion batteries (PIBs) have been considered as attractive alternatives to lithium-ion batteries due to their cost competitiveness. Anodes with complicated electrochemical mechanisms determine the performance and safety of battery systems to a large degree. Among a wide range of anode materials for SIBs and PIBs, ferromagnetic metal (Fe, Co, and Ni) sulfides and selenides have captured prominent attention by virtue of their high theoretical capacities, suitable potentials, and relatively low price. Although some breakthrough results have been achieved, a few intrinsic issues stemming from the materials themselves need to be further explored and studied, especially in the field of PIBs, an emerging research interest. Herein, in this review, we highlight the pioneering investigation of typical ferromagnetic metal sulfides and selenides for application as anodes in SIBs and PIBs and overview their recent research progress. Meanwhile, the preparation methods, structural characteristics, charge storage mechanisms, and electrochemical properties are outlined. Finally, the present challenges and research perspectives are discussed.

8) Unexpected intercalation-dominated potassium storage in WS_2 as a potassium-ion battery anode (co-authorship, in cooperation with Yuhan Wu)

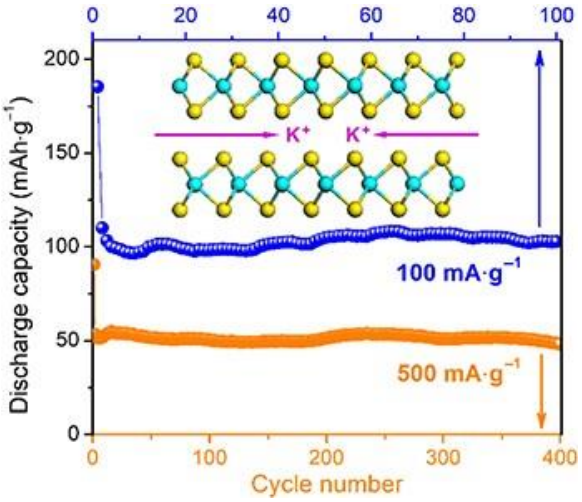

Unexpected intercalation-dominated process is observed during K^+ insertion in WS_2 in a voltage range of 0.01–3.0 V. This is different from the previously reported two-dimensional (2D) transition metal dichalcogenides that undergo a conversion reaction in a low voltage range when used as anodes in potassium-ion batteries. Charge/discharge processes in the K and Na cells are studied in parallel to demonstrate the different ion storage mechanisms. The Na^+ storage proceeds through intercalation and conversion reactions while the K^+ storage is governed by an intercalation reaction. Owing to the reversible K^+ intercalation in the van der Waals gaps, the WS_2 anode exhibits a low decay rate of 0.07% per cycle, delivering a capacity of 103 mAh g^{-1} after 100 cycles at 100 mA g^{-1}. It maintains 57% capacity at 800 mA g^{-1} and shows stable cyclability up to 400 cycles at 500 mA g^{-1}. Kinetics study proves the facilitation of K^+ transport is derived from the intercalation-dominated mechanism. Furthermore, the mechanism is verified by the density functional theory (DFT) calculations, showing that the progressive expansion of the interlayer space can account for the observed results.

9) Ammonium vanadium bronze as a potassium-ion battery cathode with high rate capability and cyclability (co-authorship, in cooperation with Dr. Yang Xu)

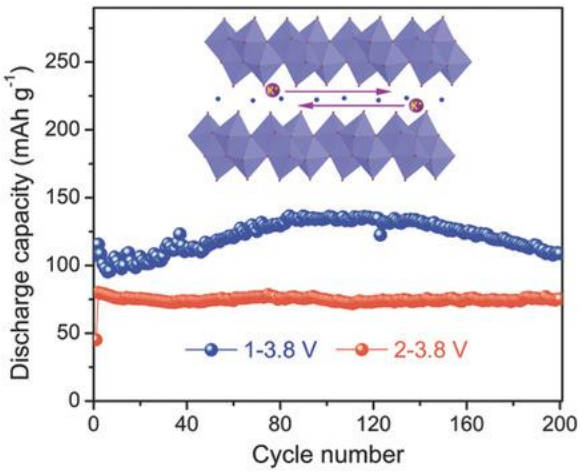

K-ion batteries (KIBs) are a promising alternative to lithium-ion batteries. Despite the rapid development of KIB anodes, cathodes have not developed to the same extent due to the sluggish kinetics of K-ion intercalation. Here, ammonium vanadium bronze $NH_4V_4O_{10}$ (NVO) is proposed as a potential KIB cathode material. The as-synthesized NVO features a large interlayer spacing of 9.8

Å and self-assembled flower-like architecture. The cathode delivers a high capacity of 136 mAh g^{-1} (50 mA g^{-1}) and a decay rate of 0.02% per cycle over 200 cycles in the range of 1–3.8 V. It retains 94% capacity (80 mAh g^{-1}) after 200 cycles in the range of 2–3.8 V. Moreover, it exhibits fast rate capability by delivering 51 mAh g^{-1} at a rate as high as 3 A g^{-1} (2–3.8 V), being 90% of the capacity at 0.1 A g^{-1}. Electrochemical mechanism studies suggest that K-ion storage in NVO is a topotactic process, where transition between V^{4+} and V^{5+} occurs. They also show that prevention of deammoniation at a higher voltage toward 4.2 V is critical for the structural stability of NVO. This work may stimulate future exploitation of vanadium oxides in KIBs and more insights into the mechanisms of K-ion storage.

10) Bismuth oxychloride nanoflake assemblies as a new anode for potassium ion batteries (co-authorship, in cooperation with Wei Li)

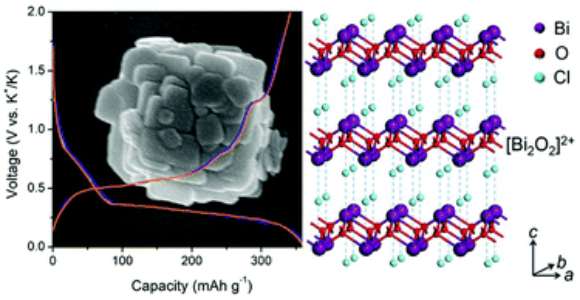

This work reports the first demonstration of bismuth oxyhalides as anode materials in potassium-ion batteries. BiOCl nanoflake assemblies deliver high capacities of 367 mAh g^{-1} at 50 mA g^{-1} and 175 mAh g^{-1} at 1 A g^{-1}. The formation of K–Bi alloys at an early stage of potassiation is observed.

11) Enhancing potassium-ion battery performance by defect and interlayer engineering (co-authorship, in cooperation with Dr. Yang Xu)

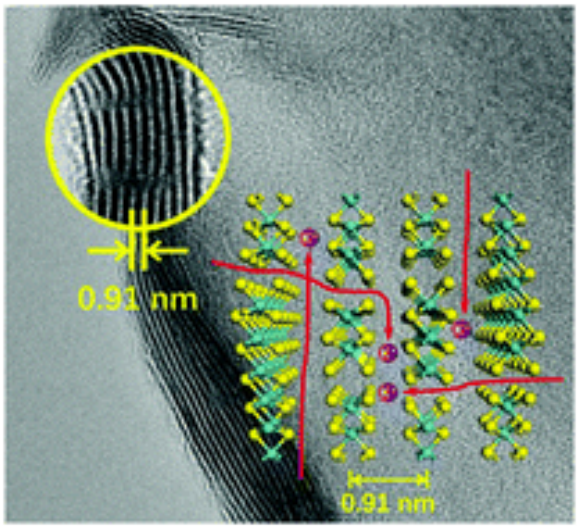

Defect and interlayer engineering is applied to exploit the large van der Waals gaps of transition metal dichalcogenides for potassium-ion batteries (KIBs). As a demonstrator, MoS_2 nanoflowers with expanded interlayer spacing and defects in the basal planes are used as KIB anodes in the voltage range of 0.5–2.5 V, where an intercalation reaction rather than a conversion reaction takes place to store K-ions in the van der Waals gaps. The nanoflowers

show enhanced K-storage performance compared to the defect-free counterpart that has a pristine interlayer spacing. Kinetic analysis verifies that the K-ion diffusion coefficient and surface charge storage are both enhanced in the applied voltage range of the intercalation reaction. The collective effects of expanded interlayer spacing and additionally exposed edges induced by the in-plane defects enable facile K-ion intercalation, rapid K-ion transport and promoted surface K-ion adsorption simultaneously.

12) MoS_2 nanosheets with expanded interlayer spacing for enhanced sodium storage (co-authorship, in cooperation with Huishuang Dong)

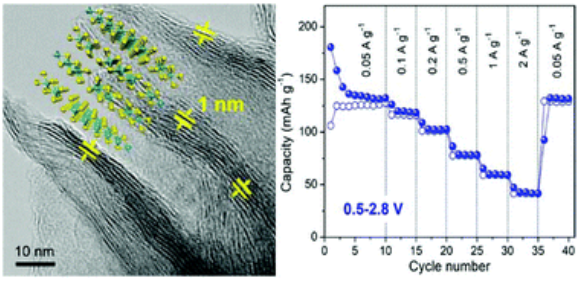

Sodium-ion battery technology is a promising alternative to lithium-ion batteries for low-cost and large-scale energy storage applications. The larger size of the Na-ion relative to the Li-ion imposes kinetic limitations and often results in sluggish Na-ion diffusion. It is a great necessity to explore prominent structural features of materials to overcome the limitations and improve the diffusion. Layered MoS_2 has an ideal two-dimensional diffusion pathway because of the weak van der Waals interaction between the layers. However, the limited gallery height of 0.3 nm is insufficient to achieve fast Na-ion diffusion. A facile hydrothermal route at medium-ranged temperatures is reported in this work to obtain interlayer expanded MoS_2 nanosheets. The interlayer spacing is greatly expanded to 1 nm and facilitates Na-ion insertion and extraction in the van der Waals gaps. The nanosheet morphology shortens the Na-ion diffusion distance from the lateral side. The interlayer expanded MoS_2 nanosheets are used as sodium-ion battery anodes in the voltage window of 0.5–2.8 V, where intercalation reaction contributes to Na storage and the layered structure can be preserved. The nanosheets exhibit a high cycling stability by retaining 92% of the initial charge capacity after 100 cycles and a great rate capability of 43 mAh g^{-1} at 2 A g^{-1}. Kinetics study reveals a significant alleviation of diffusional limitation, verifying the improved Na-ion diffusion and enhanced Na storage. The presented work explores the utilization of the van der Waals gaps to store ions and sheds light on designing two-dimensional materials in other energy systems.

Appendix III: scientific contributions

In total, I have published and jointly published 13 papers in SCI-indexed international scientific journals during the period of my Ph.D. study, including 6 papers with the first authorship and 7 papers with the co-authorship. Many of the SCI-indexed papers are published in first-class scientific journals in physics, chemistry, and materials science, such as Nature Communication, Nano Energy, Energy & Environmental Materials, Small, Small Methods, Journal of Materials Chemistry A, ACS Applied Materials & Interfaces, Inorganic Chemistry Frontiers, Nanoscale Horizon, Nano Research, Chemical Communications. So far, the published papers have been cited more than 734 times, and my h-index is 10 according to Google Scholar.

Besides, I also made 10 contributions to conferences, including 6 talks and 4 posters.

AIII.1 Publication contributions in SCI-indexed scientific journals

1) J. Yao, **C. Zhang**, G. Yang, M. Sha, Y. Dong, Q. Fu, Y. Wu, H. Zhao, M. Wu, Y. Lei, Bismuth nanoparticles confined in carbonaceous nanospheres as anodes for high-performance potassium-ion batteries, ACS Applied Materials & Interfaces, (2021). (IF: 9.229, **Shared first authorship**)
2) X. Zhao, **C. Zhang**, G. Yang, Y. Wu, Q. Fu, H. Zhao, Y. Lei, Bismuth selenide nanosheets confined in thin carbon layers as anode material for advanced potassium-ion batteries, Inorganic Chemistry Frontiers, (2021). (IF: 6.17, **Shared first authorship**)
3) Y. Wu, Q. Zhang, Y. Xu, R. Xu, L. Li, Y. Li, **C. Zhang**, H. Zhao, S. Wang, U. Kaiser, Enhanced potassium storage capability of two-dimensional transition-metal chalcogenides enabled by a collective strategy, ACS Applied Materials & Interfaces, 13 (2021), 18838-18848. (IF: 9.229)
4) Y. Wu, **C. Zhang**, H. Zhao, Y. Lei, Recent advances in ferromagnetic metal sulfides and selenides as anodes for sodium-and potassium-ion batteries, Journal of Materials Chemistry A, 9 (2021), 9506-9534. (IF: 12.732)
5) **C. Zhang**, Y. Xu, K. He, Y. Dong, H. Zhao, L. Medenbach, Y. Wu, A. Balducci, T. Hannappel, Y. Lei, Polyimide@Ketjenblack composite: a porous organic cathode for fast rechargeable potassium-ion batteries, Small, 16 (2020), 2002953. (IF: 13.281)
6) **C. Zhang**, H. Zhao, Y. Lei, Recent research progress of anode materials for potassium-ion batteries, Energy & Environmental Materials, 3 (2020), 105-120. (IF: 15.122)

7) **C. Zhang**, Y. Xu, G. Du, Y. Wu, Y. Li, H. Zhao, U. Kaiser, Y. Lei, Oxygen-functionalized soft carbon nanofibers as high-performance cathode of K-ion hybrid capacitor, Nano Energy, 72 (2020), 104661. (IF: 17.881)
8) Y. Wu, Y. Xu, Y. Li, P. Lyu, J. Wen, **C. Zhang**, M. Zhou, Y. Fang, H. Zhao, U. Kaiser, Unexpected intercalation-dominated potassium storage in WS_2 as a potassium-ion battery anode, Nano Research, 12 (2019), 2997-3002. (IF: 8.183)
9) Y. Xu, H. Dong, M. Zhou, **C. Zhang**, Y. Wu, W. Li, Y. Dong, Y. Lei, Ammonium vanadium bronze as a potassium - ion battery cathode with high rate capability and cyclability, Small Methods, 3 (2019), 1800349. (IF: 14.188)
10) W. Li, Y. Xu, Y. Dong, Y. Wu, **C. Zhang**, M. Zhou, Q. Fu, M. Wu, Y. Lei, Bismuth oxychloride nanoflake assemblies as a new anode for potassium ion batteries, Chemical Communications, 55 (2019), 6507-6510. (IF: 6.222)
11) Y. Xu, F. Bahmani, M. Zhou, Y. Li, **C. Zhang**, F. Liang, S.H. Kazemi, U. Kaiser, G. Meng, Y. Lei, Enhancing potassium-ion battery performance by defect and interlayer engineering, Nanoscale Horizons, 4 (2019) 202-207. (IF: 9.94)
12) Y. Xu, **C. Zhang**, M. Zhou, Q. Fu, C. Zhao, M. Wu, Y. Lei, Highly nitrogen doped carbon nanofibers with superior rate capability and cyclability for potassium ion batteries, Nature Communications, 9 (2018) 1720. (IF: 14.919, **Shared first authorship**)
13) H. Dong, Y. Xu, **C. Zhang**, Y. Wu, M. Zhou, L. Liu, Y. Dong, Q. Fu, M. Wu, Y. Lei, MoS_2 nanosheets with expanded interlayer spacing for enhanced sodium storage, Inorganic Chemistry Frontiers, 5 (2018) 3099-3105. (IF: 6.17)

AIII.2 Conference contributions

1) **C. Zhang**, Y. Xu, L. Liu, Y. Lei, Highly nitrogen doped carbon nanofibers with superior rate capability and cyclability for potassium ion batteries, The 83rd Annual Conference of the DPG, Mar. 31–Apr. 5, 2019, Regensburg, Germany. (Talk)
2) **C. Zhang**, Y. Xu, L. Liu, Y. Lei, A low cost potassium Prussian blue cathode for potassium ion batteries, The 83rd Annual Conference of the DPG, Mar. 31–Apr. 5, 2019, Regensburg, Germany. (Poster)
3) Y. Wu, Y. Xu, **C. Zhang**, Y. Lei, Tungsten sulfide: An intercalation-type anode material for potassium-ion battery, The 83rd Annual Conference of the DPG, Mar. 31–Apr. 5, 2019, Regensburg, Germany. (Talk)

4) Y. Wu, Y. Xu, F. Bahmani, **C. Zhang**, Y. Lei, Enhancing potassium-ion battery performance by defect and interlayer engineering, The 83rd Annual Conference of the DPG, Mar. 31–Apr. 5, 2019, Regensburg, Germany. (Poster)
5) L. Liu, H. Zhao, Y. Xu, **C. Zhang**, Y. Fang, Y. Lei, Rational surface engineering toward optimizing hydrogen evolution activity of nanoporous electrodes, The 83rd Annual Conference of the DPG, Mar. 31–Apr. 5, 2019, Regensburg, Germany. (Talk)
6) L. Liu, H. Zhao, **C. Zhang**, Y. Xu, D. Yang, Y. Lei, Mechanism of $SeOx^{2-}$ immobilization by δ-Bi_2O_3 microsphere with surface oxygen vacancies, The 83rd Annual Conference of the DPG, Mar. 31–Apr. 5, 2019, Regensburg, Germany. (Poster)
7) **C. Zhang**, Y. Xu, M. Zhou, L. Liu, Y. Lei, Low-cost $K_{0.220}Fe[Fe(CN)_6]_{0.805}$ as cathode material for potassium-ion batteries, The 82nd Annual Conference of the DPG, Mar. 11–Mar. 16, 2018, Berlin, Germany. (Talk)
8) Y. Wu, Y. Xu, **C. Zhang**, Z. Liu, Y. Lei, Preparation and catalytic properties of chitosan supporting sliver-based composite, The 82nd Annual Conference of the DPG, Mar. 11–Mar. 16, 2018, Berlin, Germany. (Talk)
9) L. Liu, H. Zhao, Y. Xu, S. Xu, **C. Zhang**, Z. Zeng, Y. Lei, Evaluate the role of nanostructure current collector in supercapacitor electrode when the electroactive material is in the form of thick layer, The 82nd Annual Conference of the DPG, Mar. 11–Mar. 16, 2018, Berlin, Germany. (Talk)
10) L. Liu, H. Zhao, R. Xu, S. Xu, **C. Zhang**, Y. Lei, Transparent CdS@TiO_2 nanotextile photoanode with boosted photoelectrocatalytic efficiency and stability, The 82nd Annual Conference of the DPG, Mar. 11–Mar. 16, 2018, Berlin, Germany. (Poster)

AIII.3 Award

10/2020: The publication in Nature Communication (www.nature.com/articles/s41467-018-04190-z) is awarded publication prize 2020 in TU Ilmenau (Publikationspreis der TU Ilmenau 2020). This paper has attracted great attention in relevant research fields. So far, it has been cited for more than 522 times since its publication in 2018.

Declaration

I hereby declare that this Ph.D. dissertation entitled ‘Effective Strategies to Enhance Electrochemical Performance of Carbon Materials for Non-Aqueous Potassium- and Sodium-Ion Capacitors’ was carried out by me for the degree of Doctor of Philosophy under the supervision of Prof. Dr. Yong Lei. All data and information in this dissertation that have been directly or indirectly consulted or used from other sources are clearly stated. This dissertation has not been submitted, in part or in whole, for any other degree or examination in any other university. I have acknowledged all main sources of help, and I have made clear exactly what was done by others and what I have contributed when the work was done jointly with others. Some of the results may have been published in scientific journals or elsewhere. I am aware that the falsity of this dissertation will be regarded as an attempt of deception and will cause the derogation of the doctoral procedure.